HIGHLY NONLINEAR SOLITARY WAVES FOR RAIL BUCKLING PREVENTION

by

Luyao Cai

B.S. in Engineering Mechanics, Harbin Institute of Technology, 2011

Submitted to the Graduate Faculty of

Swanson School of Engineering in partial fulfillment

of the requirements for the degree of

Master of Science

University of Pittsburgh

2013

UNIVERSITY OF PITTSBURGH

SWANSON SCHOOL OF ENGINEERING

This thesis was presented

by

Luyao Cai

It was defended on

July 25, 2013

and approved by

Morteza Torkamani, PhD, Associate Professor, Department of Civil and Environmental Engineering

Qiang Yu, PhD, Assistant Professor, Department of Civil and Environmental Engineering

Thesis Advisor: Piervincenzo Rizzo, PhD, Associate Professor, Department of Civil and Environmental Engineering

HIGHLY NONLINEAR SOLITARY WAVES FOR RAIL BUCKLING PREVENTION

Luyao Cai, M.S.

University of Pittsburgh, 2013

One of the major structural problems in the railroads made of continuous welded rails is buckling in hot weather and breakage or pulling apart in cold weather. Buckling is usually caused by the high compressive stress due to thermal load or weak track conditions, and sometimes vehicle loads. The prevention of track buckling is related to the determination of the temperature, called rail neutral temperature, at which the net longitudinal force in the rail is zero.

In the project presented in this thesis we investigated the capability of a novel sensing system to indirectly measure applied stress in rails and predict incipient buckling. This system consists of a simple and cost-effective transducer, recently developed at the University of Pittsburgh, which enables the generation and detection of highly nonlinear solitary waves (HNSWs), which are compact non-dispersive mechanical waves that can form and travel in highly nonlinear systems such as granular, layered, or porous materials, where they are conventionally generated by the mechanical impact of a striker.

To prove the feasibility of this novel system to predict buckling temperature or measure applied stress, we investigated numerically and experimentally the interaction between solitary waves propagating along a chain of granular particles and slender beams of different shapes, lengths, and boundary conditions. We found that the geometric and mechanical properties of the beam or thermal stress applied to the beam alter certain features of the solitary waves.

Overall, the work presented in this thesis was articulated in four main tasks: 1) literature review; 2) create a semi-analytical model; 3) design and test new transducers; and 4) conduct a series of experiments including a field test at the University of California, San Diego.

This HNSWs approach does not require many electronic accessories and shows a good sensitivity to the properties of the material that is at the interface with the chain of particles. Moreover, it only observes the propagation of solitary waves within the transducer without the waves in the rail.

TABLE OF CONTENTS

LIST OF TABLES

LIST OF FIGURES

PREFACE

First, I would like to thank Professor P. Rizzo for providing me the opportunity to perform this research. I couldn't finish this dissertation without his guidance and continuous support through the process of my research.

This report presents the results of the research activities conducted under Contract DTFR53-12-C-00014 between the University of Pittsburgh and the U.S. Federal Railroad Administration. The main objective of the contract was to conduct a feasibility study on the use of highly nonlinear solitary waves for the prediction of buckling in rails due to excessive thermal stress.

For this project we used test equipment at the University of Pittsburgh's Laboratory for Nondestructive Evaluation and Structural Health Monitoring studies and the Watkins-Haggart Structural Engineering Laboratory (WHSEL). A field test was conducted at the Powell Laboratories at the University of California, San Diego (UCSD).

Some of the work presented in this report was conducted with the contribution of Dr. Xianglei Ni former student and postdoctoral scholar at the Laboratory for Nondestructive Evaluation and Structural Health Monitoring studies. The authors are grateful to Prof. Jinkyu Yang at the University of South Carolina and Prof. Chiara Daraio at ETH Zurich (Switzerland) for their contribution to the work presented in Ch. 6.

The authors would like to acknowledge Leith Al-Nazer, program manager, and Gary Carr and Cameron Stuart, technical advisors, all at the U.S. Federal Railroad Administration for their

valuable suggestions. The authors are grateful to Prof. Francesco Lanza di Scalea, Xuan Zhu, and Dr. Robert Phillips at UCSD for all the logistic support provided during the execution of the field test at San Diego.

The contribution of Mr. Charles Hager, full-time staff member at the University of Pittsburgh's Department of Civil and Environmental Engineering, in the preparation of the transducers used in this project is greatly appreciated. Dr. Ni's knowledge in the HNSWs experiments helps me a lot.

Most of all, I owe my deepest gratitude to my great parents and my lovely girlfriend for their love and support.

DISCLAIMER

The use of the results or reliance on the material presented is the responsibility of the reader. The contents of this document are not meant to represent standards and are not intended for use as a reference in specifications, contracts, regulations, statutes, or any other legal document. The opinions and interpretations expressed are those of the authors and other duly referenced sources. The views and findings reported herein are solely those of the writers and not necessarily those of the U.S. Federal Railroad Administration. This report does not constitute a standard, a specification, or regulations.

1.0 INTRODUCTION

One of the major structural problems in the railroads made of continuous welded rails (CWR) is buckling in hot weather and breakage or pulling apart in cold weather. Buckling is usually caused by the simultaneous occurrence of one or more of the following: high compressive stress due to thermal load, weak track conditions, and vehicle loads. It is estimated for instance that a 10 °C variation in temperature causes CWR force variation around 18 tons (Vortok 2007a). A typical rail buckling is shown in Figure 1.1.

Figure 1.1 Thermal Buckling in a Continuous Welded Rail (Robertson 2012)

In the decade 2003-2012, in the United States track buckling was responsible for 297 derailments, which caused $121M in reportable damage, and accounted for 10% of all damage relative to the track bed. In 2012, track buckling caused 27 derailments, $24.2M in reportable

damage which represented 25.9% of the all reportable damage for that year (Federal Railway Administration 2013).

The prevention of track buckling is related to the determination of the temperature, called rail neutral temperature (RNT), at which the net longitudinal force in the rail is zero. The simplest relationship between the RNT T_N and the longitudinal stress σ at a given temperature T_R is given by:

$$\sigma = E\alpha\left(T_R - T_N\right) \tag{1.1}$$

where E is the Young's modulus of the rail and α is the thermal expansion coefficient of steel. By knowing the buckling stress of the structure, the proper assessment of T_N allows for the prediction of the temperature T at which the rail will buckle.

The typical response of the track structure to temperature increase (temperature above the RNT) can be described in terms of the neutral temperature, buckling temperature, and safe temperature as shown in Figure 1.2, which shows the response of a track with an initial imperfection (Lim et al. 2003). Three branches, namely AB, BC and CD, are visible. Branches AB and CD represent stable equilibrium configurations of the track structure, whereas BC represents an unstable equilibrium configuration. At point B, the increase in temperature above T_N causes the track structure becomes unstable and the track will snap into the next stable configuration on branch CD. The point C corresponds to the safe temperature increase (T_{min}), which represents the temperature below which there is only one stable equilibrium configuration, hence, it is ''safe'' to expose the track to any temperature increase less than point C, without risk of buckling, provided there are no dynamic effects like passing trains.

Railroad agencies and companies are compelled to capitalize in Nondestructive Evaluation (NDE) methods to determine the value of T_N.

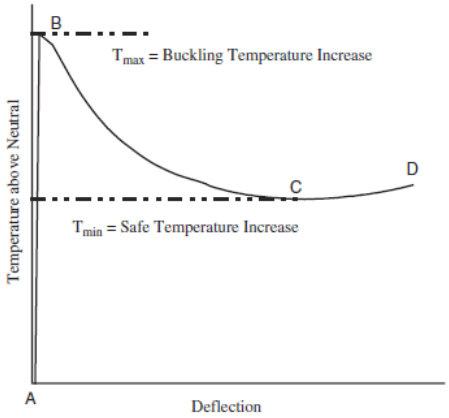

Figure 1.2 Typical track response curve (Lim et al. 2003)

1.1 PROPOSED METHODOLOGY

In this project, we investigated the capability of a novel sensing system to indirectly measure applied stress in rails. This Nondestructive Evaluation (NDE) system consists of a simple and cost-effective transducer, recently developed at the University of Pittsburgh (Ni et al. 2011a, b). The transducer enables the generation and detection of highly nonlinear solitary waves (HNSWs), which are compact non-dispersive mechanical waves that can form and travel in highly nonlinear systems such as granular, layered, or porous materials (Nesterenko 1983, Daraio and Nesterenko 2005).

A typical HNSW transducer is shown in Figure 1.3(a) and it consists of a chain of steel particles[1] filled inside a tube and surmounted by an electromagnet. The chain of particles inside the tube is the granular medium that sustains the propagation of the HNSWs. The electromagnet serves to control the stroke of a striker. The impact of the striker with the chain generates a

[1] The transducer shown in Figure 1.3 can accommodate spherical particles 4.76 mm in diameter

solitary wave pulse that propagates along the granular medium. The wave can be detected either by sensor beads such as the one schematized in Figure 1.3(c) placed inside the chain, or by a force sensor located at the end of the chain.

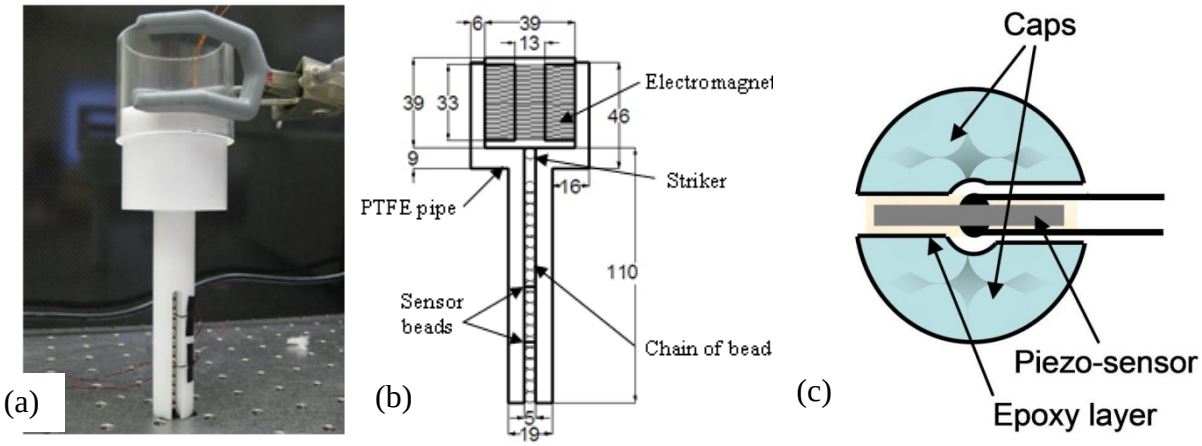

Figure 1.3 (a) Photo of the actuator for the remote non-contact generation of HNSWs. (Ni et al. 2011a) A mechanical holder was used during the experiments presented here. (b) Actuator's design. Dimensions are expressed in mm. (c) structure of a sensor bead (Daraio et al. 2005).

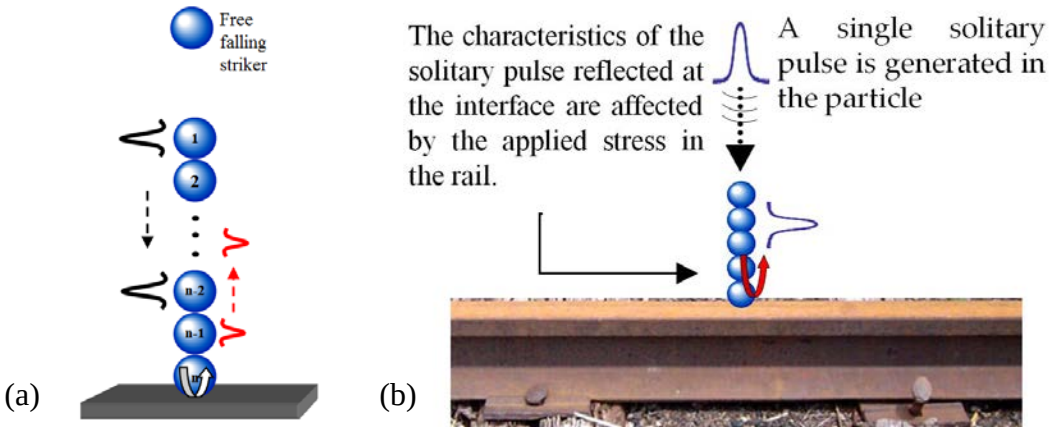

Figure 1.4 (a) Scheme of structural assessment by means of HNSWs. A free falling striker creates a solitary wave along a chain made of spherical particles (the chain is the highly nonlinear medium). The characteristics of the solitary pulse reflected at the interface (the red pulse) are affected by the stress in the rail. (b) Concept as it applies to rails.

The overall principle of the HNSWs method proposed in this project is illustrated in Figure 1.4. The chain is in contact with the rail to be monitored. The impact of a striker on the

chain generates a single solitary pulse that propagates through the chain and is partially reflected at the interface. We hypothesize that certain features of the reflected solitary wave are indirectly correlated to the thermal stress acting on the rail.

Figure 1.5 shows the typical shape of a solitary wave pulse as detected by two sensor beads. In this study we considered the time of flight (TOF), i.e. the transit time at a sensor bead between the incident and the reflected wave, and the amplitude ratio of the reflected solitary wave, i.e. the ratio of the reflected wave to the incident solitary wave as possible features to be correlated to the rail stress. In order to measure the amplitude and time of arrival of the solitary waves, two or more sensor beads like the one schematized in Figure 1.3 (c), were inserted in the chain.

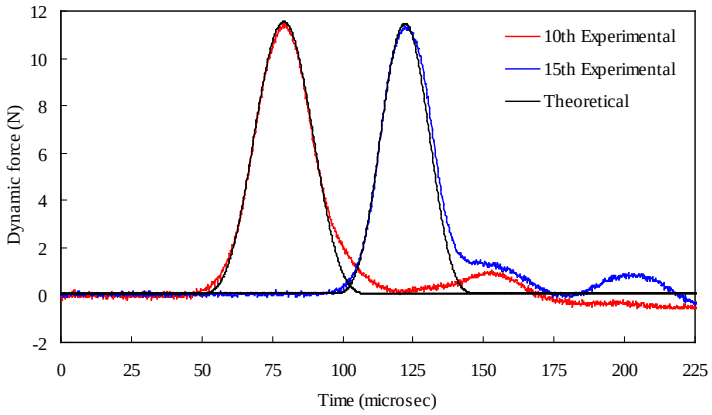

Figure 1.5 Typical profile of a solitary wave pulse detected by two sensor beads (Ni et al. 2011a)

The quality of the proposed innovation is related to the use of an approach that does not require many electronic accessories, and the use of HNSWs which have shown sensitivity to the properties of the material that is at the interface with the chain of particles (Ni et al. 2011a,b,c, 2012a,b,c 2013). Moreover, the proposed methodology does not consider the propagation of the waves along the rail running direction or across the rail thickness, but observes the propagation

of the solitary waves within the transducer, i.e. within the granular medium. In fact, we hypothesize that the characteristics of the solitary waves are altered at the chain-rail interface. The potential payoff of this project is a new NDE paradigm that is less invasive, more cost-effective, as well as more sensitive to the variation of thermal stress in rails.

The research was conducted at the University of Pittsburgh (Pitt)'s Laboratory for NDE and Structural Health Monitoring (SHM) studies directed by Prof. Rizzo and at the University of Pittsburgh's Watkins-Haggart Structural Engineering Laboratory (WHSEL). A large scale test was conducted at the University of California, San Diego (UCSD) at a research facility directed by Prof. Francesco Lanza di Scalea.

1.2 SCOPE OF WORK

The scope of the work conducted under the aegis of the U.S. Federal Railroad Administration (FRA), was to conduct a feasibility study on the use of HNSWs for the prediction / prevention of incoming rail buckling. The primary hypothesis was that the characteristics of the HNSWs propagating in a nonlinear medium placed in contact to the rail are affected by the flexural stiffness of the rail. In turn the flexural stiffness is affected by the thermal stress acting on the rail due to the presence of a thermal gradient. The main goal of the research was determining in a non-contact way the occurrence of large compressive stress rather than the determination of the rail neutral temperature.

The work was articulated in four main tasks: 1) conduct a literature review; 2) design and test new transducers; 3) create a semi-analytical model; and 4) conduct a series of experiments. The first task involved a review of the main analytical formulations relative to the structural

buckling of columns and rail and a review of the main NDE methods applied in the rail industry. In the second task we designed and tested a few different transducer shapes with the objective to create the optimal transducer for the application in rails. We then created a simplified model to predict the coupling between the nonlinear system and the linear medium (beam or rail) subjected to axial load. Finally we conducted several experiments where HNSW transducers were used to monitor thermal stress in beams and rails and they were conducted at the Laboratory for NDE and SHM studies, the Watkins-Haggart Structural Engineering Laboratory, and at UCSD.

1.3 REPORT OUTLINE

The outline of the report is as follows.

Chapter 2 presents a brief overview of buckling theories of columns and rails from the structural engineering standpoint. Different types of analytical formulations and finite element models are introduced.

Chapter 3 describes a literature review of NDE/SHM methods to prevent/predict buckling in rails.

Chapter 4 illustrates the theoretical background associated with the propagation of HNSWs and a simplified methodology to model numerically the interaction of solitary waves with linear medium. The study of this chapter has been submitted for possible publication in Cai et al. 2013b.

Chapter 5 reports the results relative to the propagation of HNSW in a curved granular chain. The effects of different radius and different angles of the curved channel on propagation of HNSW are studied. The outcome of this study has been published in Cai et al. 2013a.

Chapter 6 describes a comparative study on three different transducers for the measurement of nonlinear solitary waves. The outcome of this study has been published in Ni et al 2013.

Chapter 7 presents the experiments done at the University of Pittsburgh.

Chapter 8 discusses the field test performed at the Powell laboratories at UC San Diego.

Chapter 9 presents the conclusion of this project and the recommendations for future works.

2.0 BUCKLING OF COLUMNS AND RAILS

In 1744, Leonhard Euler proposed an equation to calculate the buckling load of an ideal column subjected to an axial force. A column is said to be ideal if it is perfectly straight before loading, is homogeneous, and the load is applied through the centroid of the cross section. The Euler formulation also assumes that the material remains linear elastic and the buckling occurs in a single plane. If the load P is lower than the elastic proportional limit and below the critical value of buckling, the bar remains straight and undergoes only axial compression. This equilibrium is stable, which means that if a lateral force is applied and a small lateral deflection is produced, the column returns to its equilibrium position once the lateral force is removed. The critical load (or Euler load) is then defined as the maximum value which is capable to keep this stable equilibrium (Timoshenko and Gere 1963).

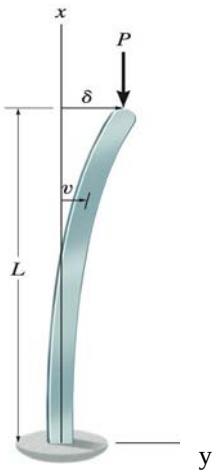

Figure 2.1 Effect of axial load on a free-fixed column subjected to axial load (Hibbeler 2011, Figure 13-11a)

As the Euler's formulation theory may not be sufficiently accurate for some engineering systems, Engesser (1889, 1891) modified the Euler's theory by including the effects of shear deformations. However, Engesser's solution lacks of accuracy when the slenderness ratio[2] is very small, i.e. when the column is very short. Thus, Haringx (1942) developed an alternate buckling formula which predicts an infinite buckling load as the slenderness approached zero. Several authors discussed the advantages of both Engesser's and Haringx's approaches (Timoshenko and Gere 1963, Bazant 1971, 2003, Zielger 1982, Reissner 1972, Reissner 1982, Bazant and Cedolin 1991, Gjelsvik 1991). In the following sections we discuss each model briefly.

2.1 EULER'S MODEL

Let consider an ideal column, fixed at the base and free at the other end, where it is subjected to an axial force ***P*** (Figure 2.1). The differential equation for the deflection curve is (Hibbeler, 2011):

$$\frac{d^2y}{dx^2} = \frac{P}{EI}(\delta - y) \tag{2.1}$$

where, x represents the longitudinal coordinate, y is the lateral displacement, E is the Young's modulus of the material, I is the moment of inertia, and δ represents the displacement at the point of application of the force P. The critical buckling load P_E is:

[2] The slenderness ratio here is defined as the ratio of the effective length of a column to the least radius of gyration of its cross section

$$P_E = \frac{\pi^2 EI}{4L^2} = \frac{\pi^2 EI}{(kL)^2} \tag{2.1}$$

where the coefficient *k*, called the *effective-length factor*, depends on the type of ends' support. For pinned ends *k*=1, for fixed and free ends *k*=2, for fixed ends *k*=0.7.

2.2 ENGESSER'S MODEL

Engesser (Engesser, 1891) included the shear force $Q = P\left(dy/dx\right)$ generated by the transverse deformation *dy/dx*. The change in slope of the deflection curve produced by the shearing force is nQ/AG, where A is the cross-sectional area of the column, G is the shear modulus, and n is a coefficient depending on the shape of the cross section. For a rectangular cross section, $n = 1.2$, and for a circular cross section, *n=1.11*. For an I beam bent about the minor axis of the cross section (that is, bent in the plane of the flanges) the factor is $n \sim 1.2\ A/A_f$ where A_f is the area of the two flanges. If a W-beam bends in the plane of the web (about the major axis) the factor $n \sim 1.2\ A/A_w$, where A_w is the area of the web. The curvature $\left(dy^2/dx^2\right)$ associated with the presence of the shear force Q is given by:

$$\frac{n}{AG}\frac{dQ}{dx} = \frac{nP}{AG}\frac{d^2y}{dx^2} \tag{2.2}$$

When it is included into the Euler model (Equation 2.1), we obtain:

$$\frac{d^2y}{dx^2} = \frac{P}{EI}\left(\delta - y\right) + \frac{nP}{AG}\frac{d^2y}{dx^2} \tag{2.3}$$

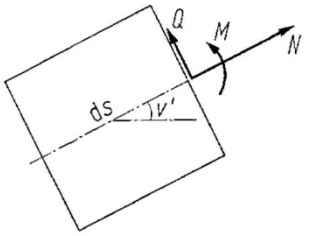

Figure 2.2 Stresses in an un-deformed (cross-section perpendicular to the axis) element with transverse deformation in Engesser's approach (Zielger, 1982)

from which the Engesser's critical buckling load P_{cr}:

$$P_{cr} = \frac{P_E}{1+\left(nP_E/GA\right)} \tag{2.4}$$

is derived (Engesser 1889, Engesser 1891). In Equation 2.5, P_E represents the Euler buckling load.

2.3 HARINGX'S MODEL

Haringx (1942) modified Engesser's equation (2.3) taking into account the presence of the shear force Q. The difference with the Engesser's model is that the stresses of a deformed element, such as the one depicted in Figure 2.3, were considered. The model assumes that the angle $d\theta$ represents the change in slope due to the bending moment $M = P\left(\delta - y\right)$.

Due to shear strains, the slope of the deflected curve is

$$\frac{dy}{dx} = \theta + \frac{nQ}{AG} = \theta\left(1+\frac{nP}{AG}\right) \tag{2.5}$$

The differential equation in the element with a deformed cross section is

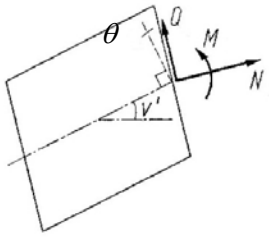

Figure 2.3 Stresses in a deformed element (cross-section not perpendicular to the axis) in Haringx's model (Zielger, 1982)

$$\frac{d^2y}{dx^2} = \frac{P(\delta - y)}{EI}\left(1 + \frac{nP}{AG}\right) \tag{2.6}$$

Solving this differential equation, we get the Haringx's critical buckling load:

$$P_{cr} = \frac{GA}{2n}\left(\sqrt{1 + \frac{4nP_E}{GA}} - 1\right) \tag{2.7}$$

The difference between the Engesser's and Haringx's solutions is negligible for slender columns. However, for cases in which the effect of shear is large, as in short columns, the Haringx's result is more accurate. Bazant (1971), and Bazant and Cedolin (1991) proved that Engesser's model is equivalent with Haringx's after shear modulus *G* is replaced by *(G-N/A)* where *N* is the axial force.

2.4 MODIFIED ENGESSER'S MODEL

Zielger (1982) modified the model proposed by Engesser by including the axial deformation associated with the presence of the compressive force. He proved that the effect of axial shortening is of the same order of magnitude as the influence of shear. For a column in

compression status the presence of the negative strain ε increases the flexural rigidity $\alpha=EI$ and shear rigidity $\beta=kGA$ by:

$$\alpha' = \frac{\alpha}{1+\varepsilon}, \quad \beta' = \frac{\beta}{1+\varepsilon} \tag{2.8}.$$

This yields to the following critical load P_{cr}:

$$P_{cr} = \frac{EA}{2}\left[1 \pm \sqrt{1 - \frac{4}{EA}\left(\frac{P_E}{1+\left(nP_E/GA\right)}\right)}\right] \tag{2.9}$$

where n is the coefficient defined in the Engesser's model (see Section 2.2). Since $P_E/EA<<1$ and $P_E/GA<<1$, Equation (2.10) can be simplified as:

$$P_{cr} \approx \frac{1+P_E/EA}{1+nP_E/GA} \cdot P_E \tag{2.10}$$

which shows that the decrease in length increases the critical load, whereas the shear stress decreased the critical load.

2.5 MODIFIED HARINGX'S MODEL

Attard (2003a, 2003b) proposed a model where axial and shear deformation were taken into account under the assumption that the cross-sectional shape remain identical after deformation. By using a formulation based on the strain energy, the following critical load was derived:

$$P_{cr} = \frac{EA}{2\left(1-\frac{E}{G}\right)}\left[1 \pm \sqrt{1 - \frac{4P_E}{EA}\left(1-\frac{E}{G}\right)}\right] \tag{2.11}$$

This solution is similar to Haringx's solution in Equation 2.8.

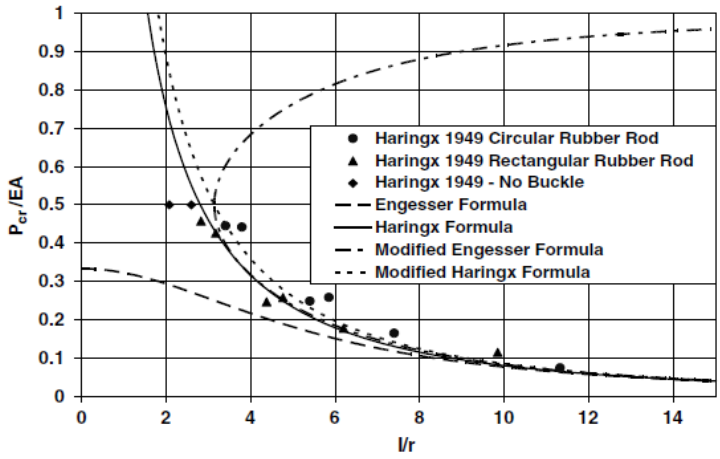

Figure 2.4 Comparison of column buckling test results for rubber rods in Haringx (1949) with predictions of Haringx and Engesser formulas (Attard, 2008).

In a later study Attard (2008) conducted an experimental investigation and compared the results to the predictions provided by different buckling theories. Figure 2.4 shows the critical load P_{cr} normalized with respect to the axial rigidity EA as a function of the slenderness ratio l/r. The lower limit $l/r=2$ represents the value at which the yielding load is lower than the buckling load.

Figure 2.4 demonstrates that the Engesser's model diverges from the experimental results when the column is short, e.g. $l/r<4$. This occurs that in short columns the shear deformation is large and should not be ignored. The figure also shows that the discrepancy between Engesser's model and Haringx's becomes evident large when axial force is large (P/EA>0.5).

2.6 THERMAL BUCKLING IN RAILS

In general, a CWR is elastically constrained by ballast and pad-fastener and its buckling behavior is usually affected by the vertical, lateral and torsional vibration (Lim et al. 2003). The models to

describe track buckling are generally based on simplified beams or are based on rail–tie models. The beam-based models consider either the vertical or the horizontal plane modes, i.e. they hypothesize that buckling occurs in one mode only: in the vertical plane or in the lateral plane. In the 1960s, Bijl applied the beam model to explore the stability of the CWR track using energy methods (Bijl 1964). Kerr and El-Aini (Kerr 1972, Kerr and El-Aini 1978, El-Aini 1978) studied the buckling of rails according to the vertical plane. In these studies the railroad track is simplified as a single beam either supported by elastic springs or by a rigid base. A more sophisticated model was regarding the structural response of rails subjected to operational loads (Kerr and Zarembski 1981).

Kerr (1976) also proposed a model of post-buckling to derive the safe temperature. In this analysis, the rail-tie structure was replaced by an equivalent "track-beam" system consisting of two separate rails as shown in Figure 2.5.

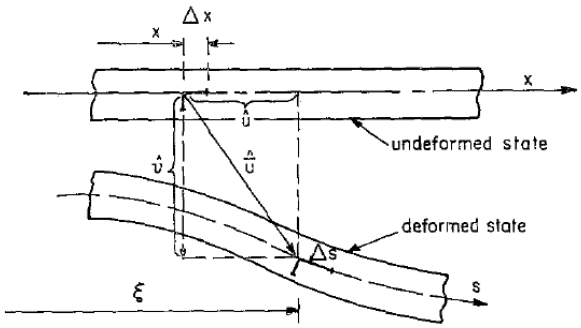

Figure 2.5 Kerr's "track-beam" model (Kerr 1976)

The principle of virtual displacement was used to derive the safe temperature. The following assumptions were made: (1) the lateral and axial resistance coefficients (ρ_0, r_0) was considered constant; (2) prior and during buckling the response of the rail-tie structure is elastic; (3) the vertical deflection can be neglected. The safe temperature was determined from the

possible post-buckling profiles schematized in Figure 2.6, which represent the four possible post buckling shapes (*I, II, III, IV*) observed in actual rails. In these post-buckling profiles, a rail track consists of five regions: the lateral buckled zone of length *2l*, two adjoining regions of length *a* with no lateral deformation, and outside infinite regions which are subjected only to axial load. Kerr (1976) analyzed all these four cases and found the minimum value of the temperature which corresponds to the safe temperature.

By using the virtual work principle, Kerr (1976) derived a formula that relates the temperature T_0, which is the temperature change measured from the installation temperature, to the rail deformation:

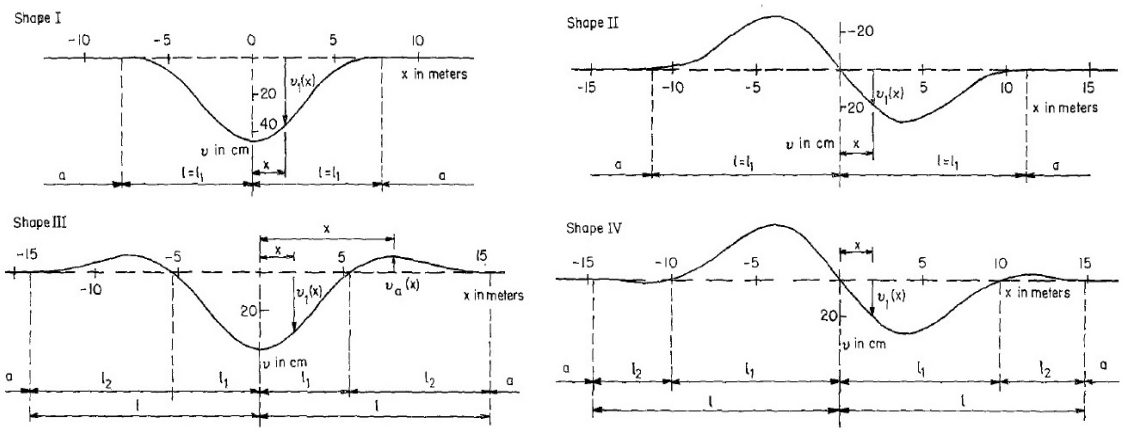

Figure 2.6 Buckling modes observed in field tests----shape *I, II, III, IV* (Kerr 1976)

$$EA\alpha T_0 = \tilde{N}_t + lr_0\left\{-1 \pm \sqrt{1+\frac{EA}{l^2 r_0}\int_0^l v_1'^2 dx}\right\} \tag{2.13}$$

In Equation (2.13) the function $v_1(x)$ is given by:

$$v_1(x) = \frac{\rho_0 l^4}{2EI(\lambda l)^2}\left[1-\frac{x^2}{l^2}-\frac{2(\cos\lambda x-\cos\lambda l)}{\lambda l \sin\lambda l}\right] \tag{2.14}$$

where $tan\,\lambda l = \lambda l$, $\lambda l = 4.493$, $\tilde{N}_t$ is the compression force (negative axial force) in the buckling region which is a constant and ρ_0, r_0 means lateral and axial resistance separately. Equations (2.13) and (2.14) enable to find the compression force $\tilde{N}_t$ and to determine the corresponding value of $\lambda = \sqrt{\tilde{N}_t / (EI)}$ and the length of buckling region $l = 4.493/\lambda$. The lateral displacement $v_{\max}$ can also be derived from formula $v_1(x)$. Results of the relationship between temperature increase T_0 and the maximum lateral displacement $v_{\max}$ are shown in Figure 2.7. Corresponding solutions for post-buckling shapes *II, III, IV* are also derived and plotted in the same graph.

In the study conducted by Kerr (1976), a specific rail section was considered. And it was found that the safe temperature is $T_{\min} = T_L = 43.7\ ^oC$. Note that for any temperature increase above T_L there correspond three states of equilibrium (Figure 2.7): the stable state (before point A), the unstable state on branch $\overline{AL}$ and the state on branch $\overline{LB}$. For this beam model, different shapes of buckling I, II, III, IV showed a similar result that the safe temperature increase is $T_L \approx 42\ ^oC$.

Few years later, Kerr (1980) suggested that the use of a bilinear response curve for axial resistance gives much more accurate safe temperature values than the use of a constant axial resistance. The model for axial resistance is shown in Figure 2.8. A fitted curve (the dotted line in Figure 2.8) was used to simulate the nonlinear axial resistance. It was concluded that the use of nonlinear resistance curve lowers the obtained safe temperature T_L values. He also evaluated the effect of lateral resistance on track buckling analysis, in which he found that the assumption of linear lateral resistance is not valid, whereas the assumption of constant lateral resistance is admissible.

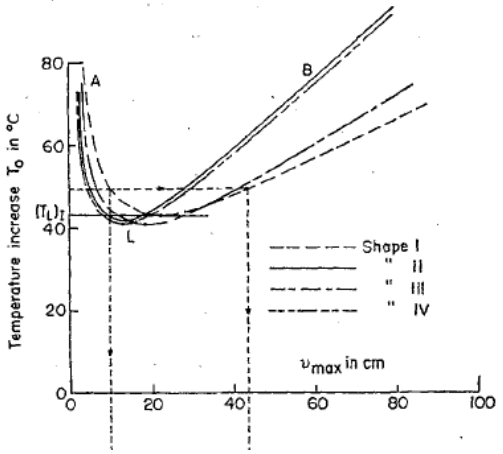

Figure 2.7 Temperature increase T_0 in post-buckling equilibrium state for shapes *I, II, III, IV* (Kerr 1976)

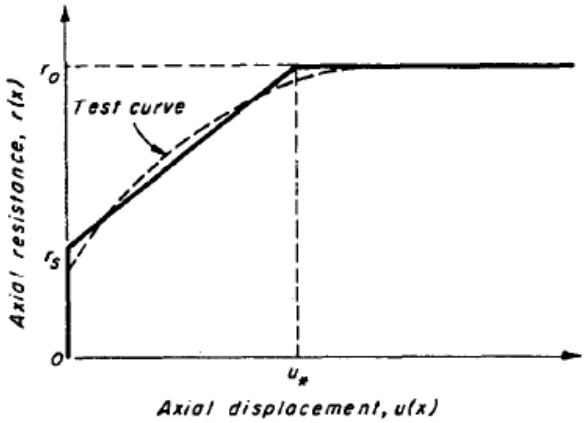

Figure 2.8 Axial resistance-displacement response (Kerr 1980)

Samavedam (Samavedam 1979) developed a model that included track imperfections, nonlinearities in the ballast resistances and missing ties and presented a Fourier series technique for the complete solution of the lateral track buckling problem. Kish (1982) developed a theory for tracks of finite length. Samavedam (Samavedam et al. 1983) conducted a series of parametric studies based on the two analyses mentioned above. The study showed that both lateral foundation resistance and the size of the initial imperfections have a profound effect on the buckling phenomenon. The study also concluded that buckling test on short tracks can misrepresent reality and lead to overestimates of buckling strength. It should be mentioned that,

different with the model considering nonlinear foundation resistances reviewed before, the parametric study used constant values and assumed the nonlinearity in the latter state can be neglected.

According to Ramesh (1985), Kerr's model presented the following shortcomings: 1) assumption of plane-section hypothesis, 2) the resistance of tie-to-rail rotation being considered negligible; 3) the flexibility of cross-ties not being taken into account; 4) assumption of constant axial and lateral foundation resistances.

Esveld and Hengstum (Esveld and Hengstum 1988) explored track stability in tight curves using a finite element method associated with a beam model. EI-Ghazaly and Sherbourne (EI-Ghazaly and Sherbourne 1991) applied a three dimensional open section single beam model to analyze track stability using the FE method. The buckling modes indicated interaction between lateral and torsional buckling. However, for simplicity, ballast resistance and fastener stiffness were constant and they only investigated the bifurcation buckling loads in a single rail subjected to a mechanical load.

Grissom and Kerr (Grissom and Kerr 2006) utilized the nonlinear formulation for lateral buckling of a tangent track presented by Kerr in conjunction with the new track equations with rotationally stiff fasteners presented by Kerr and Zarembski (Kerr and Zarembski 1981) and Kerr and Accorsi (Kerr and Accorsi 1985). The obtained differential equations for a simple frame-type structure subjected to a lateral loading $\hat{q}$ are

$$\begin{aligned} &2EI\hat{v}^{iv} + \left(\hat{N} - k\right)\hat{v}'' + \left(2k/h\right)\tilde{u}' = \hat{q} \\ &EA\tilde{u}'' - \left(2k/h^2\right)\tilde{u} + \left(k/h\right)\hat{v}' = 0 \\ &EA\hat{u}'' = 0 \end{aligned} \tag{2.12}$$

They concluded that the rotational stiffness of the fasteners and the tie stiffness in the lateral plane have a profound effects on the safe temperature increase $T_{\min}$.

Therefore, in an actual track, these parameters should be maintained as high as possible to reduce the possibility of lateral buckling. The relationship between the temperature increase ΔT and the lateral displacement v_{max} under different rotational fastener stiffness and lateral tie stiffness are plotted in Figure 2.9 (a) and 2.9 (b), respectively.

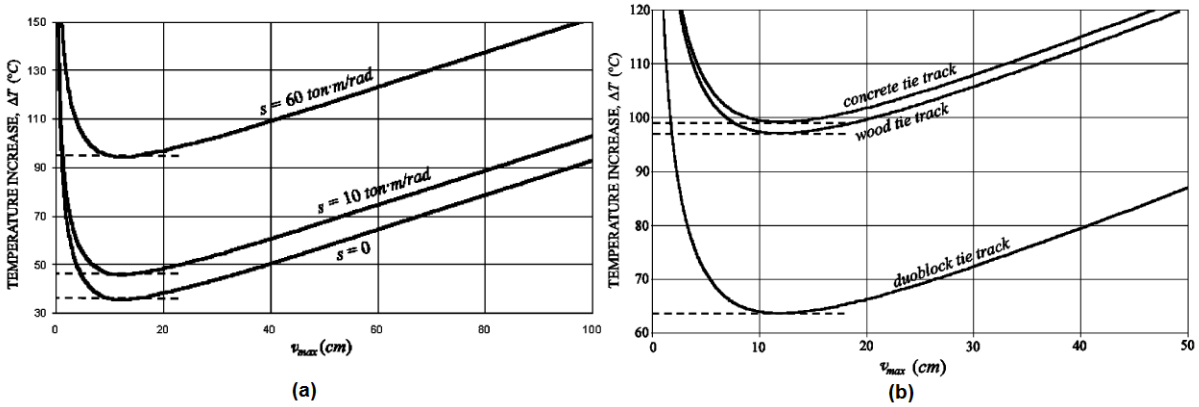

Figure 2.9 Temperature increaseΔT ($^{\circ}C$) vs. lateral displacement v_{max} (cm) under different (a) fastener rotational stiffness (b) tie lateral stiffness (Grissom and Kerr 2006)

In additional to the shortcomings pointed out earlier, another drawback of the analytical studies reviewed so far is in regard to the final buckled shape of the track. The four possible post-buckling shapes (I, II, III, IV) illustrated in Figure 2.7 have been widely observed in field tests. None of the analyses reviewed above has the capability to predict the final buckled shape, if a certain configuration of pre-buckled track is given. All these studies were based on the premise that the track could buckle into each shape, and then compared the minimum safe temperature at each condition.

From 1982 to 1987, Kish and co-authors published a series of articles about track buckling using the beam model (Kish and Samavedam 1983, 1987, Kish et al. 1982,). However,

their model did not consider the effects of nonuniformly distributed ballast resistance along the track, missing ties and fasteners, the variation of the track gauge, and differing neutral temperatures between two rails, etc. In 1988, Esveld and Hengstum explored track stability in tight curves using an FEM associated with a beam model (Esveld and Hengstum 1988). In 1991, El-Ghazaly et al. applied a 3-D open section single beam model to the analysis of track stability using the FEM (EI-Ghazaly et al. 1991). The buckling modes indicated interaction between lateral and torsional buckling. However, for simplicity, ballast resistance and fastener stiffness were constant and the authors only investigated the bifurcation buckling loads in a single rail subjected to a mechanical load. At 1985, Ramesh developed a two-dimensional rail–tie model, one tie plus two rails in the length of a tie spacing, for lateral track buckling analysis (Ramesh 1985).

The models that consider rail-tie systems or three-dimensional models essentially consist of two parallel rails that rest on a series of cross-ties as shown in Figure 2.10. Since those constraints are not continuously distributed and the force-displacement relations between constraints and rails are nonlinear, several simplified models of CWRs were proposed to simulate buckling behavior.

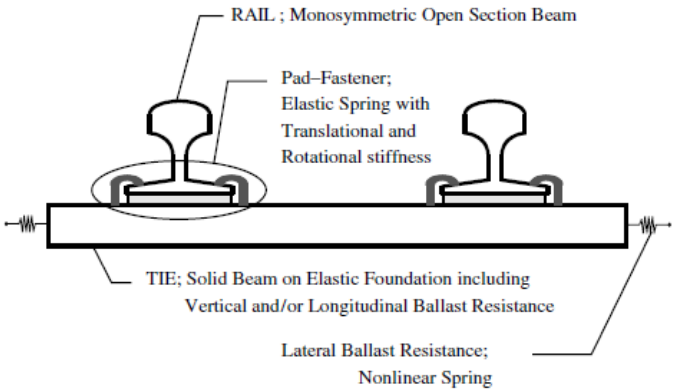

Figure 2.10 Cross section of two parallel rail tracks (Lim et al. 2003)

2.7 FINITE ELEMENT MODEL

The first finite element models on the track as a discrete structure for purposes of stability analysis were proposed by So and Martin (1977a, b), So and Young (1978) and Algan (1977). So and Young's model considered the effects of nonlinear ballast resistances, nonlinear fastener rotational resistance, initial imperfections, missing ties and lateral axial applied forces. The buckling load was found to be greatly affected by changes in lateral ballast resistance, initial imperfections and missing ties. However, since the finite element model consists of a single beam, the plane section hypothesis was kept as a premise.

The model proposed by Algan (1977) differed from So and Young's model in that it modeled two rails joined by flexible ties. Lateral and axial ballast resistances are modeled by nonlinear spring elements. Algan's study found that tie-stiffness has a significant effect on the buckling temperature of the track. The major disadvantage of this model is that it assumes the rail-tie fasteners to be rigid, and does not account for initial imperfections.

2.7.1 Ramesh's 2D FEM model

Ramesh (1985) developed a model that considering initial imperfections, foundation resistances, rail-tie fastener resistances to determine the safe temperature of a rail. The track was discretized into short sections as shown in Figure 2.11(a) and each element had six degrees of freedom (u_i, $\underline{w}_i$, Φ_i). Spring models were used to simulate the lateral (R_i) and longitudinal (T_i) resistance from the ballast and the rail fastener resistance (T_i) from cross-tie structures in Figure 2.11(b).

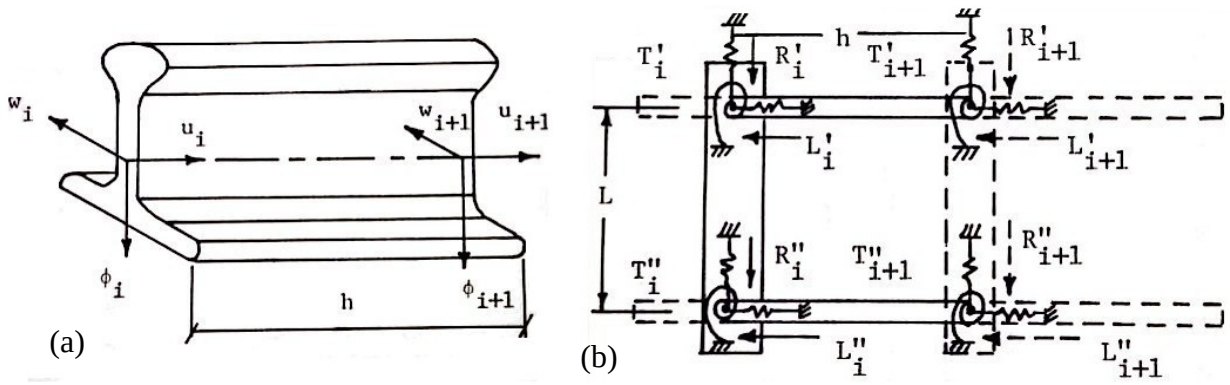

Figure 2.11 (a) Discretization of rail tracks (b) components of track-structure element (Ramesh 1985)

Two different cases were simulated, one without rail-tie fastener resistance (fastener torsion resistance), and the second with a linear spring model of rail-tie fastener resistance. The numerical results were compared to the experimental work and theoretical results from beam model by Kish and Samavedam (Kish and Samavedam 1982). The comparison is shown in Figure 2.12.

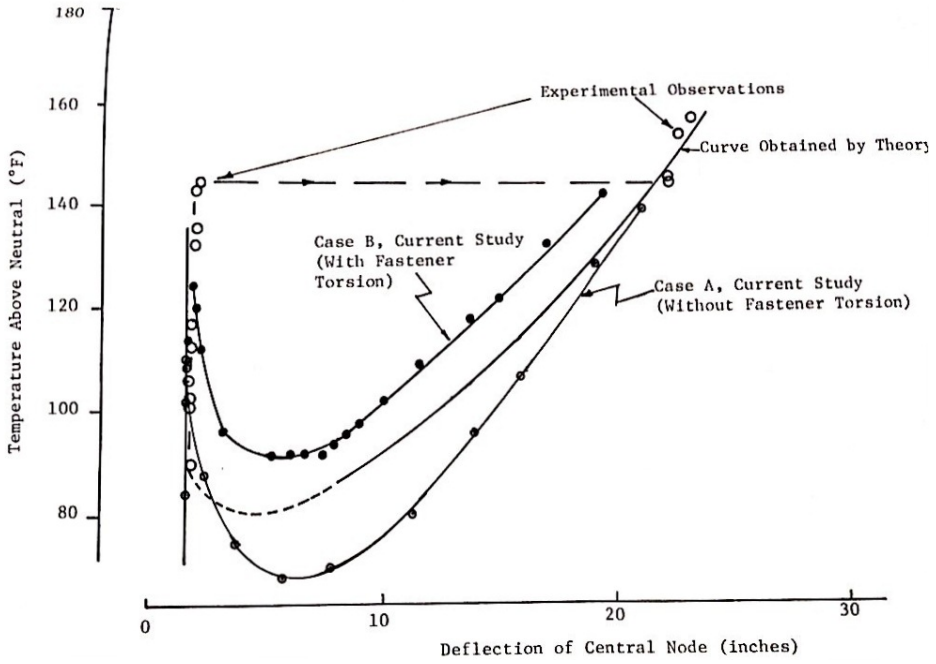

Figure 2.12 Comparison between Ramesh's 2-D model results in two different cases (Case A, without fastener torsion; Case B, with fastener torsion) and experimental observation and theoretical results from beam model by Kish and Samavedam (Ramesh 1985)

As seen in Figure 2.12, the safe temperature increase, i.e. the minimum value of the temperature above neutral in case A is smaller than that in case B. It shows that the existence of fastener torsion does make a difference in the calculation of safe temperature increase and should not be neglected. In other aspect, Kish's theoretical safe temperature increase value from beam's model is located between case A and case B of 2-D modeling. The difference remains unclear and may be because of the different rail parameters used in these two studies. (Ramesh 1985)

The advantage of 2-D FEM model over beam models is that:

(1) In beam model, hypothesis of plane section are made while in 2-D FEM this assumption does not need to be made.

(2) The application of FEM method in 2-D FEM model make it possible to take into account the discretized and also nonlinear ballast resistance and linear rail-tie resistance.

(3) 2-D FEM model predicts not only the buckling and safe temperature limits, but also the shape of the final buckled track, which has not been achieved in previous beam model.

The 2-D FEM model introduced by Ramesh (Ramesh 1985) did not consider the vertical rail-tie-ballast interaction which may affect the buckling analysis.

2.7.2 Nam-Hyoung Lim's 3D FEM model

The 2-D FEM model have their shortcomings for the CWR track buckling analysis, as they restrict to either the vertical or the horizontal plane. A 3-D FEM model was proposed by Lim et al. (2003), in which the vertical rail-tie-ballast interaction is considered. Figure 2.13 shows sections of two parallel rail tracks with ties are depicted. In this structure, rails are elastically

fixed to ties using pad-fastener. And those ties are also elastically fixed and embedded into ballast.

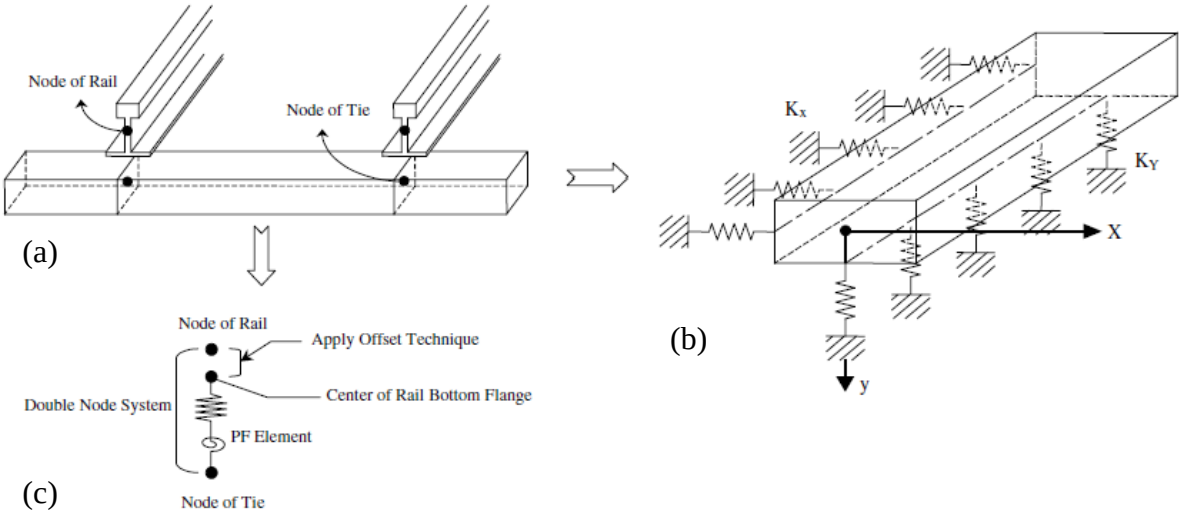

Figure 2.13 (a) Cross section of 3-D track model (b) Side view of 3-D track model (c) Geometric modeling technique for 3-D track model (Lim et al. 2003)

The interaction between rail tracks and ties was modeled into a double nodes system in which two nodes keep a constant distance. And the node of tie supports this double node system with six springs including three for force-displacement and three for moment-rotation. In order to facilitate the geometric modeling in 3-D, each modal element is lumped at the center of rail element and does not coincide with others. The node of rail and the center of rail bottom flange are separated through an offset technique. At last, ties are fixed with springs in horizontal and vertical directions as the right part of Figure 2.13.

Nam-Hyoung Lim and his colleagues (Lim et al. 2003) considered a linear temperature variation in cross-section of a rail track in Figure 2.14, the generalized thermal strain is:

$$\varepsilon_T = \alpha \cdot T_c + \alpha \cdot T_y \tag{2.16}$$

where T_c means the average temperature along the vertical direction, T_y means the linear variation of temperature in vertical direction and α means the thermal expansion coefficient. This temperature model considers the effects of heat from sunshine.

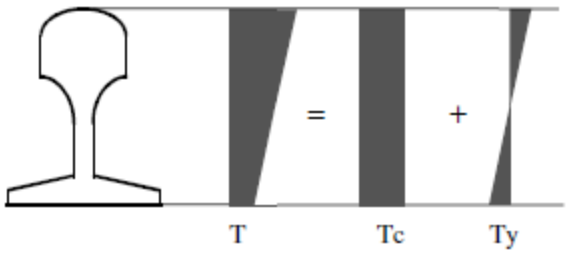

Figure 2.14 Variation of temperature field in the cross-section of rail (Lim et al. 2003)

The tie element was modeled as a solid beam on an elastic foundation under the following assumptions: (1) the cross-section retains their original shape; (2) Euler-Bernouli hypothesis (shear stress neglected); (3) Winkler foundation hypothesis (elastic spring hypothesis in vertical and longitudinal resistance); (4) linear elastic element.

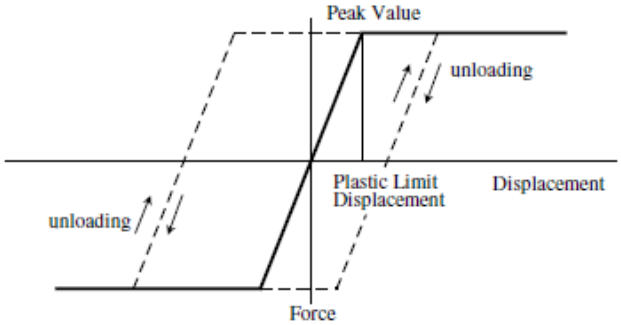

Figure 2.15 lateral force vs. lateral displacement of ties (Lim et al. 2003)

In the 3-D model (Lim et al. 2003), the ballast which is under those ties provides a support laterally, longitudinal and vertically. Existing test data indicate that the relationship between lateral force and lateral displacement of ballast is linear for small movement but nonlinear for large displacement. The relation between the lateral force and lateral displacement of ties is shown in Figure 2.15.

Three models were reviewed by Lim (Lim et al. 2003) to validate the 3-D CWR track model developed in this study. In model-A, both rail ends are hinged which means the displacements on both ends are restrained. In model-B (model-B2 has a larger rotational stiffness and lateral plastic limit displacement than model-B1), the longitudinal degree of freedom at both rail ends was elastically constrained with end spring stiffness. The solutions of temperature above neutral vs. different degree of freedom including lateral, vertical and torsional angle displacement are plotted separately in Figure 2.16. The vertical displacement and torsional angle is small compared to lateral displacement. It is also worthwhile noting that stronger boundary stiffness (model A>B1>B2) leads to a smaller buckling temperature.

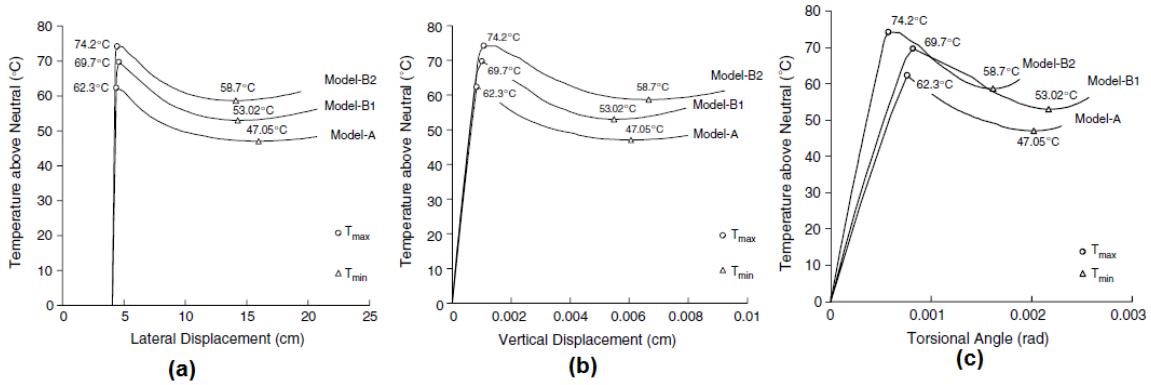

Figure 2.16 Temperature above Neutral vs. (a) Lateral Displacement (cm) (b) Vertical Displacement (cm) (c) Torsional Angle (rad) (Lim et al. 2003)

To validate this 3-D FEM model, comparison with other models is necessary. In Figure 2.17, different results about the compressive force vs. lateral displacement at the track center from 3-D FEM model (B1, B2) and beam model (Kish et al. 1982) are shown.

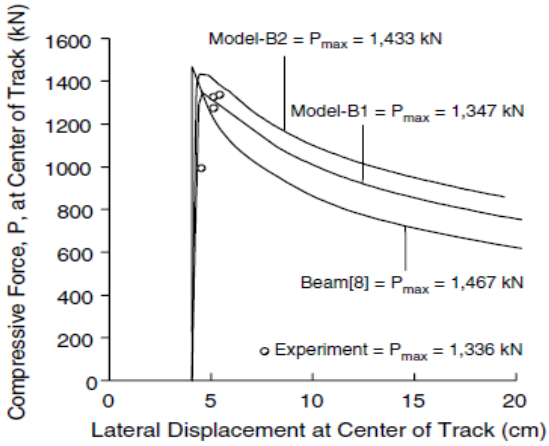

Figure 2.17 Compressive force-lateral displacement at center of rail track (Lim et al. 2003)

In Figure 2.17, the beam model gives a higher peak value of compressive force than that obtained from model-B1 and field test. The difference of forces in different models results from the effects of resistance from tie and PF in buckled zone. The beam model overestimated the CWR track stability because more degrees of freedom were restraint in beam model.

The 3-D FEM model (Lim et al. 2003) is also compared with the results derived by Ramesh's 2-D FEM model (Ramesh 1985). Track parameters and boundary conditions used in model-A are identical to those in Ramesh's study. The calculated T_{max} (buckling temperature increase) and T_{min} (safe temperature increase) was $78.3\,^{o}C$ and $49.4\,^{o}C$, respectively, in Ramesh's study. The calculated T_{max} and T_{min} from model-A is $62.3\,^{o}C$ and $47.0\,^{o}C$, respectively. This difference results from the lack of vertical deformation and torsion of the CWR and ties in the 2-D rail-tie model. That means some extra constraints have been implanted to make those degree

of freedom disappear and these constraints cause the 2-D model by Ramesh (1985) to render a higher buckling and safe temperature increase ($T_{\max}$, $T_{\min}$).

Lim (Lim et al. 2008) continued their work and did research on parametric studies on rail track buckling using the same 3-D FEM model developed in (Lim et al. 2003). Some of the important findings based on the parametric study are listed here.

(1) As the lateral tie resisting force increases, the buckling temperature $T_{\max}$ and safe temperature $T_{\min}$ increase as nonlinear. However, the buckling temperature is almost unrelated with the longitudinal tie resisting force.

(2) The buckling and safe temperature decrease as the elastic limit displacement (seen in Figure 2.15, “plastic limit displacement”) in lateral direction increases.

(3) The lateral ballast resistance and the track irregularity (alignment defect, gauge irregularity) have the maximum influence on buckling temperature while the lateral ballast resistance and the longitudinal resistance affect the safe temperature increase most.

Arbabi and Khalighi (Arbabi and Khalighi 2010) developed a discrete model, dividing a rail into several components. In their studies, a parametric study was done and the effects of lateral resistance of ballast on buckling load and buckling length is shown in Figure 2.18. It is shown that larger lateral resistance leads to a bigger buckling load, and a smaller buckling length. They also pointed out that the simple sinusoidal buckling shape assumed in many previous models is not valid unless the track properties are homogeneous along its length. For a structure such as a railroad track, with its significant length, it is not quite possible to have homogeneous properties along its full length. Local inhomogeneity can cause buckling at a lower load and with a different mode shape than sinusoidal.

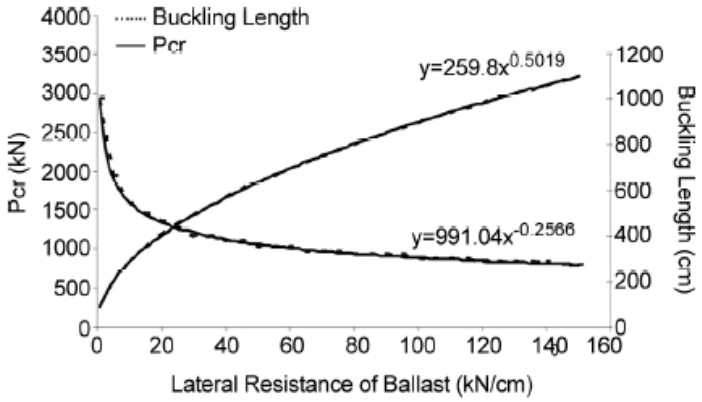

Figure 2.18 Variation of the critical load with the lateral resistance of ballast, and the associated buckling length

2.8 CONCLUSION

By comparing the three main models (Lim et al. 2003, Ramesh 1985, Kish et al. 1982) presented here we may conclude that the CWR track buckling is a three-dimensional problem, and the Ramesh's 2-D rail-tie model and Kish's beam model overestimated the CWR track stability. Also, 2-D rail-tie model may not be sufficiently adequate to represent the actual track response. Finite element methods seem to be the most accurate way to analyze the thermal buckling.

3.0 NONDESTRUCTIVE EVALUATION METHOD FOR RAIL LOAD ASSESSMENT: A REVIEW

In the last few decades several nondestructive methods were proposed and developed to determine the RNT of rail tracks or axial stress. In this chapter we review the concepts relative to the: lift method, frequency response functions method, vibration wavelength method, electromechanical impedance (EMI), magnetic Barkhausen noise, and the methods associated with the propagation of ultrasonic waves.

3.1 LIFT METHOD

The lift method is a technology patented by Vortok International Corp. and commercialized under the name of VERSE® (Vortok 2007b). It is based on the beam-column bending theory in which the axial load affects the vertical force required to lift a rail (Kish and Samavedam 1987). The principles are illustrated in Figure 3.1 where a rail is schematized as a simply supported beam. When the beam is compressed by a force *P*, the displacement δ generated by a static force *Q* increases, whereas δ decreases as tensile force increases. For an Euler-Bernoulli beam, the lateral displacement δ is given by

$$\delta = \frac{Ql^3}{48EI}\frac{3\left(\tan u - u\right)}{u^3} = \frac{Ql^3}{48EI}\chi\left(u\right) \tag{3.1}$$

where $\chi(u) = \frac{3(\tan u - u)}{u^3}$ and $u = \frac{l}{2}\sqrt{\frac{P}{EI}} = \frac{\pi}{2}\sqrt{\frac{P}{P_E}}$ where P_E is the Euler load. Conventionally $\chi(u)$ is approximated to:

$$\chi(u) \approx \frac{1}{1 - P/P_E} \tag{3.2}$$

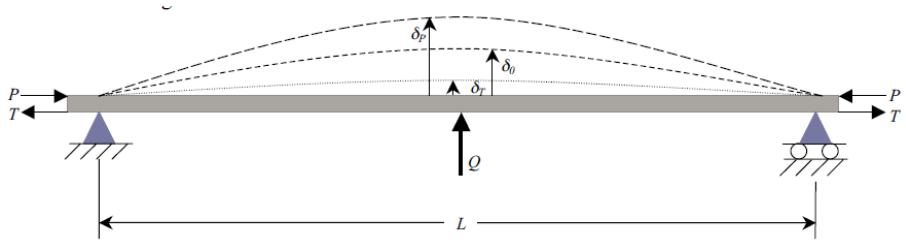

Figure 3.1 schematic diagram of lateral stiffness (Koob 2005)

In the VERSE® technology, the following formula of displacement δ is considered to estimate the longitudinal stress in the track (Kish and Samavedam 1987):

$$\delta \approx \left(\frac{\lambda Q L^3}{EI}\right)\left(\frac{1}{1 - P/P_E}\right) \tag{3.3}$$

where λ is a constant that depends on end constraints, Q is the uplift force, L is the unfastened rail length, EI is the flexural stiffness of the rail, and P_E is the Euler buckling load for the beam column over a length of L. From the Equation (3.3), the RNT is computed as:

$$RNT = T_R - \frac{P}{\alpha A} = T_R - \frac{P_E}{\alpha A}\left(1 - \frac{1}{\delta}\frac{\lambda Q L^3}{EI}\right) \tag{3.4}$$

where T_R is the rail temperature. In the lift method some 30 meters of rail is detached from the fasteners and a support spacer (Figure 3.2a) is placed 10 meters away from the mid-span. Then, the equipment visible in Figure 3.2b is used to lift steadily the rail. The vertical force needed to

lift the center by a fixed amount or the vertical displacement generated by a lift force of 10 KN is measured. The data are used to directly calculate the RNT (Vortok 2007a).

VERSE® has been tested in several countries (Vortok 2007a) and it is claimed that it can measure the RNT with an accuracy of 0.2 °C and a standard deviation of 1.3 °C. The method can be adapted to different kinds of rails and get instant result of RNT by Equation (3.4). As the method can be applied to tracks in tension, the ambient temperature must be lower than the true RNT. Usually, the complete execution of the inspection of one segment may take 20 to 30 minutes.

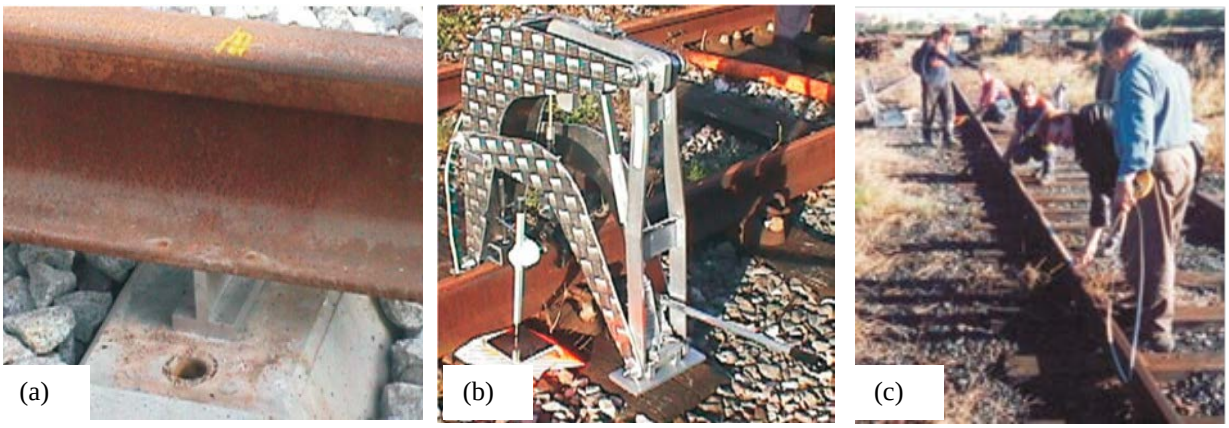

Figure 3.2 VERSE Technology (lift method) (a) unclip the rail for 30 meters (b) equipment of lifting rails (c) unclip the rail for 30 meters (Vortok, 2007a)

3.2 VIBRATION WAVELENGTH METHOD

Damljanovic and Weaver (2005) proposed a non-destructive vibration technique for the measurement of stress based on the measurement of the wavelength of bending waves. From the dispersion relation in the Euler-Bernoulli beam theory, for a beam of Young's modulus E, density ρ, area of cross-section A and moment of inertia I, the axial load P is

$$P = \rho A\left(c_b^2 r_g^2 k^2 - \frac{\omega^2}{k^2} \right) \tag{3.5}$$

where $c_b = \sqrt{E/\rho}$ is the bar wavespeed, $r_g = \sqrt{I/A}$ is the radius of gyration and k is the lateral bending wavenumber. Taking variations of Equation (3.5) and recognizing $\omega^2 \approx c_b^2 r_g^2 k^4$, we derive:

$$P = P - 0 = 4EAr_g^2 k^2 \left(\frac{\delta k}{k} \right) \tag{3.6}$$

where $\delta k/k$ is the relative distortion of k and δk is $k^{measured}|_P$ - $k^{FEM}|_{P=0}$. The value of k^{FEM} is the wavenumber predicted by finite element code. The relative distortion of lateral bending wavenumber k is defined:

$$\delta = \frac{\delta k}{k} = \frac{k^{measured} - k^{FEM}}{k^{FEM}} \tag{3.7}$$

The analytical predictions were experimentally validated by using a laser vibrometer positioned on a scanning platform parallel to the tested 136 AREMA rail to measure the wavenumber. A hydraulic actuator was used to apply axial loading on rail. The test setup is shown in Figure 3.3 (a) whereas Figure 3.3 (b) is the results of lateral displacement measured along the rail on the side of the rail head (P_1) and on the rail web (P_2).

The experimental result relative to $\delta(=\delta k/k)$ as a function of the axial load P is shown in Figure 3.4. The nonzero intercept ε may be attributed to some general parameters not properly accounted for. The slope $s=1/(4EAr_g^2k^2)$ is the coefficient of equation (3.6). With the knowledge of experimental wavenumbers, simulated wavenumbers and slope s, we can derive the axial loading P by using:

$$P = s\delta + \varepsilon \tag{3.8}$$

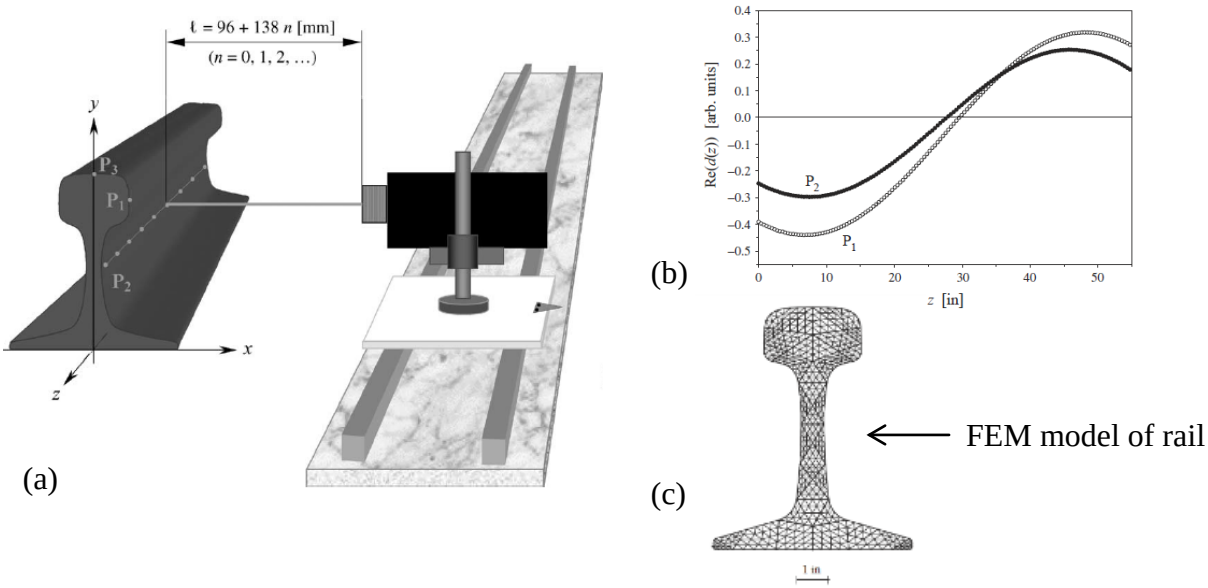

Figure 3.3 (a) Scan platform and vibrometer positioning with respect to rail; (b) Comparison of lateral displacements in the P1 and P2 scans (P1 is on the side of the rail head, P2 is on the rail web); (c) FEM model of rail section

Kjell and Johnson (2009) investigated the same methodology in more detail in a full scale laboratory experiment with a 11 *m* long rail track with clamps, sleepers. In their experiment, better measuring system was designed. The temperature drifting in temperature sensors, amplifiers and bad positioning of measurement points were minimized. And also a finer FEM was used.

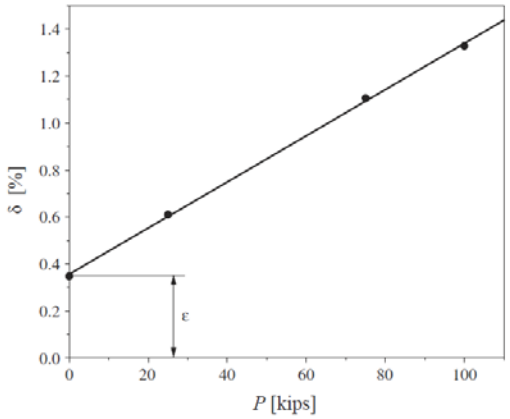

Figure 3.4 Applied load vs. relative distortion of lateral bending wavenumber *k*. The best-fit line, $\delta = \delta k/k = sP + \varepsilon$, has the slope of s=0.00983%/*kips* and the intercept ε=0.356% (Damljanovic and Weaver 2005)

3.3 ELECTROMECHANICAL IMPEDANCE METHOD

Impedance-based SHM, often indicated as the electromechanical impedance (EMI) method is an active sensing approach that exploits the relationship between the electrical impedance of a PZT and the mechanical impedance of the host structure to which the PZT is bonded or embedded. The electrical admittance, which is the inverse of the electrical impedance, is a function of the stiffness, mass and damping of the host structure, the length, width, thickness, orientation, and mass of the PZT, as well as the adhesive utilized to bond the PZT to the structure. Therefore any changes in the admittance are indicative of the presence of structural damages, provided the physical characteristics of the adhesive and the PZT remain constant. When compared to the vibration-based methods, the impedance-based methods use higher frequency ranges from the ten to the hundreds of kHz. Recently, it was demonstrated that the EMI method is also sensitive to the presence of stress on the host structure. Giurgiutiu (1999) firstly modeled the 1-D PZT-beam interaction considering both axial and flexural vibrations without static axial load. Close agreement with the experimental counterparts was reached. Lim and Soh (2012) used EMI to infer the change of the resonant frequency in a beam subjected to varying axial loading.

Phillips and Zhu (2012) applied the EMI method to a 136 AREMA rail. The electromechanical admittance of the PZT coupled to a host structure is:

$$Y(\omega) = i\omega C\left(1 - k_{31}^2 \frac{k_{str(\omega)}}{k_{PZT}(\omega) + k_{str}(\omega)}\right) \tag{3.9}$$

where C is the zero-load capacitance of the PZT transducer, $k_{31} = d_{13}/sqr\left(\bar{s}_{11}\bar{\varepsilon}_{33}\right)$ is the EMI cross-coupling coefficient of the PZT, $k_{PZT}(\omega)$ and $k_{str}(\omega)$ are respectively the dynamic stiffness of the PZT and host structure. Few statistical features were considered, including the root-mean-square deviation (RMSD), the piezoelectric efficiency factor (PEF), and the slope change of the

conductance and susceptance signature. The RMSD represents the variation of the signal across the entire susceptance and conductance signature and it is defined as:

$$RMSD(\%) = \sqrt{\frac{\sum_{i=1}^{N}(y_i - x_i)^2}{\sum_{i=1}^{N} x_i^2}} \times 100 \tag{3.10}$$

where y_i is the baseline admittance value, x_i is the current admittance, the real part for conductance and the imaginary for susceptance, measurement taken at each excitation frequency. Similar with RMSD parameter, the PEF calculated the variation of the signal, and it is given as:

$$PEF(\%) = \frac{\frac{C_1 + \ldots + C_n}{n}\sqrt{R_1^2 + \ldots + R_n^2}}{R_1 C_1 + \ldots + R_n C_n} \times 100 \tag{3.11}$$

where C_1, C_n are the means of the frequency ranges considered, R_1, R_n are the RMSD values of the frequency ranges. The last parameter is the slope change of the conductance and susceptance signatures which is evaluated by a simple first order linear regression.

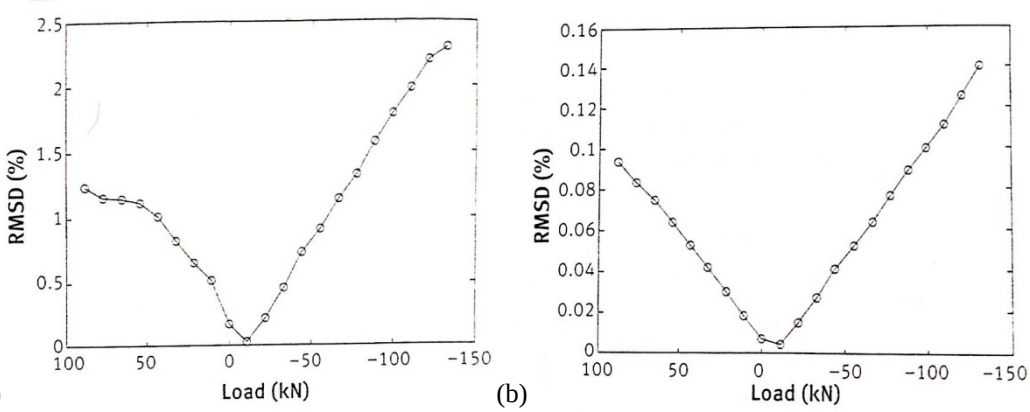

Figure 3.5 Root mean square deviation (RMSD) for (a) conductance; (b) susceptance (Phillips and Zhu 2012)

The experimental results relative to the RMSD, shown in Figure 3.6, demonstrate that the conductance and susceptance present a minimum very close to the zero stress load. The PEF factor as a function of load is instead presented in Figure 3.6.

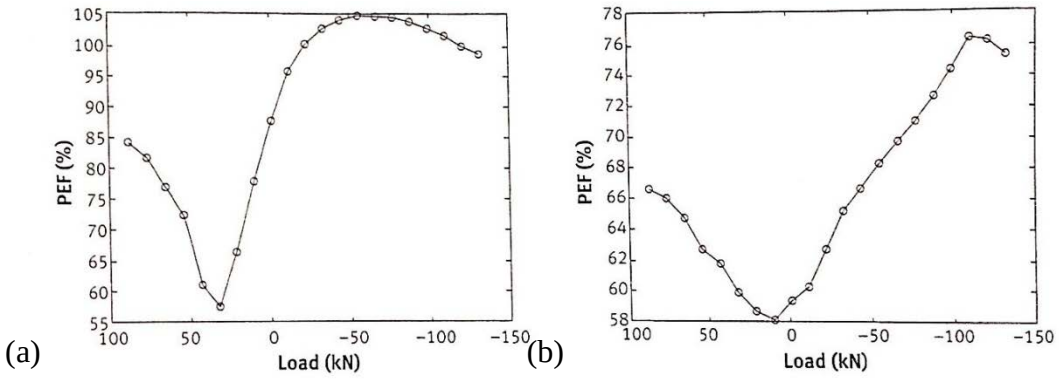

Figure 3.6 Piezoelectric efficiency factor (PEF) for: (a) conductance; (b) susceptance (Phillips and Zhu 2012)

Finally, Figure 3.7 shows the slope of the conductance and susceptance signatures as a function of load. All the features show a trend with changing axial load.

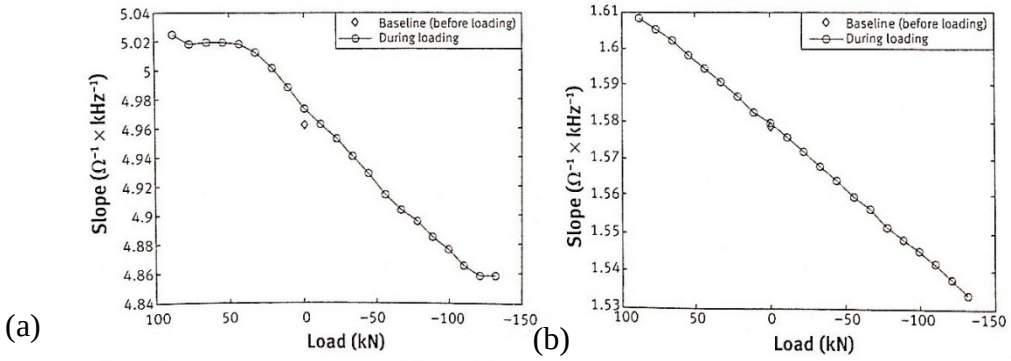

Figure 3.7 (a) Linear regression of susceptance; (b) slope change of susceptance (Phillips and Zhu 2012)

3.4 MAGNETIC BARKHAUSEN NOISE METHOD

This method is based on the Barkhausen effect which is the name given to the noise in the magnetic output of a ferromagnet when the magnetizing force applied to it is changed. The flux passing a ferromagnetic object during a typical magnetization and demagnetization process is shown in Figure 3.8 (a). Because of the irreversible properties of this magnetization process, the

flux/permeability of the ferromagnetic materials depends not only on its current environment but also on its past environment. This difference of flux/permeability in magnetization and demagnetization process is called magnetization hysteresis.

When a rail is subjected to a longitudinal load stress, its magnetic permeability changes. Tension leads to an increase of the permeability and vice versa. The magnetic Barkhausen noise (MBN) is exploited to provide a quantitative evaluation for the permeability, and therefore an indirect assessment of stress.

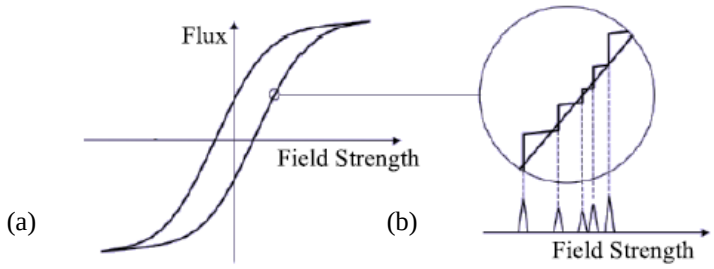

Figure 3.8 Magnetic Hysteresis Loop of Barkhausen Jumps (Wegner 2005)

Wegner (Wegner 2007) proposed a method based on the detection of the amplitude of the MBN as it depends on the rail's stress. The longitudinal stress and the neutral temperature are determined by measurement of characteristic magnetic values. The method needs calibration, which can be attained in the laboratory using calibration rails. The calibration serves to generate a diagram between a certain magnetic parameter β and the axial stress. An example of this diagram is shown in Figure 3.9.

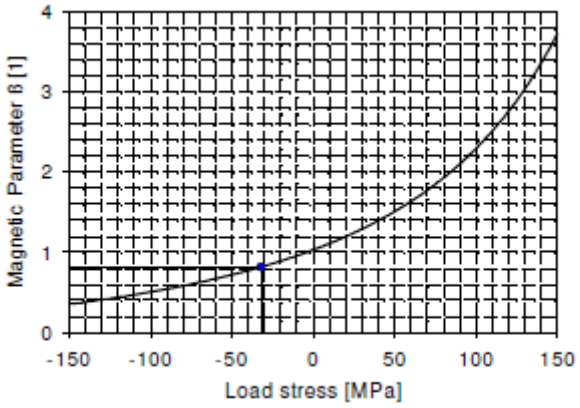

Figure 3.9 Longitudinal load stress determined by means of the rail specific calibration curve (Wegner 2007)

The method is commercialized by MAPS Technology as portable equipment. The measurements may be adversely affected by the residual stresses and unevenness, scale, rust, paint coating on the rail's surface (Wegner 2007).

3.5 ULTRASONIC BIREFRINGENCE METHOD

The ultrasonic birefringence method is based on the generation and detection of linearly polarized ultrasonic shear waves propagating along two directions that are perpendicular one to another. The difference in the time-of-flight of these two beams is dependent upon the applied stress and the residual stress on the material. As such, the major applications of the acoustic birefringence effect are the characterization of stress states in the bulk of components. The birefringence of a linearly polarized shear wave, polarized parallel to each of the two principal axes, respectively, yield quantitative results (Schneider 1995). A schematic of the setup for railroad application is presented in Figure 3.10.

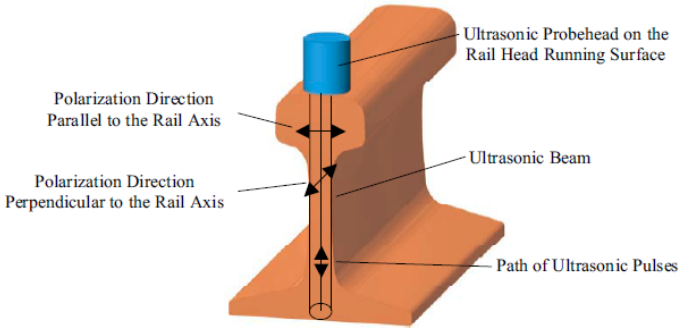

Figure 3.10 Acoustic Birefringence Method in Rail (Koob 2005)

If the anisotropy B_0 due to texture and the thermal-stress-induced anisotropy B_S are known, then the stress σ can be found as:

$$\sigma = \frac{B_0 - B_s}{\beta_B} \tag{3.12}$$

where β_B is an acoustoelastic constant defined as:

$$\beta_B = \frac{1}{2}\left(\frac{t_L - t_P}{t_L + t_P}\right) \tag{3.13}$$

where t_L and t_P are the time of flight of the wave along in the longitudinal and perpendicular direction of propagation of the waves (Szelazek 1998).

Since the acoustic birefringent method is a through-thickness method, the positive and negative parts of bending stress through the thickness cancel each other. Another advantage is that the method can be adopted by using non-contact ultrasonic transducers such as the electromagnetic-acoustic transducers (EMATs).

Hirao and his colleagues (Hirao et al 1994) used EMATs and the ultrasonic birefringence method to assess axial stress in rails. It was determined that the method enable the measurement of stress with a maximum deviation of 3 *MPa*. It should be pointed out that the use of EMATs

may require high voltages and it may be sensitive to the liftoff distance, i.e. the air gap between the EMAT and the test object.

3.6 POLARIZATION OF RAYLEIGH WAVES METHOD

Hurlebaus (2011) proposed a method to measure stress in rails using the polarization of ultrasonic Rayleigh waves. The relationship between the polarization of Rayleigh waves and the state of stress was developed numerically and preliminary experiments were conducted using lase Doppler vibrometer (LDV). The study demonstrated that Rayleigh wave polarization is more sensitive and more robust than the Rayleigh wave speed. Figure 3.11 shows the change of Rayleigh wave polarization with applied stress.

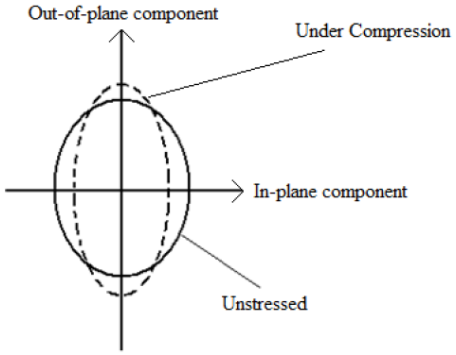

Figure 3.11 Change of Rayleigh wave polarization under applied stress (Hurlebaus 2011)

The experimental setup is shown in Figure 3.12. A wedge was used to generate Rayleigh waves in the test specimen and a LDV was used to measure the wave speed and the axial and out-of-plane displacements. One of the results is shown in Figure 3.13 and it shows the dependence of the normalized polarization of the Rayleigh wave on the normalized load.

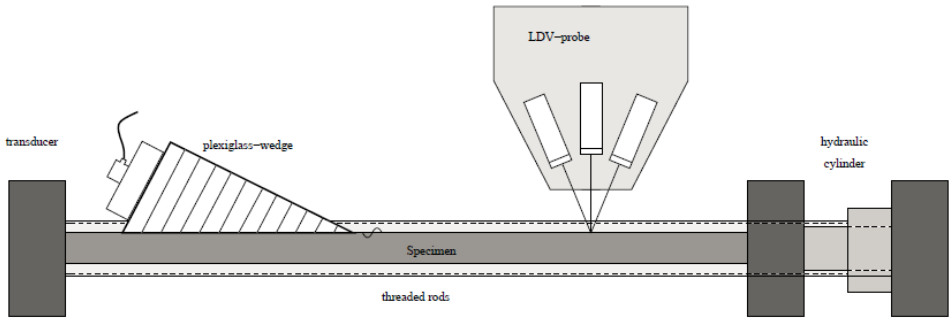

Figure 3.12 Experimental setup in polarization of Rayleigh wave measurement (Hurlebaus 2011)

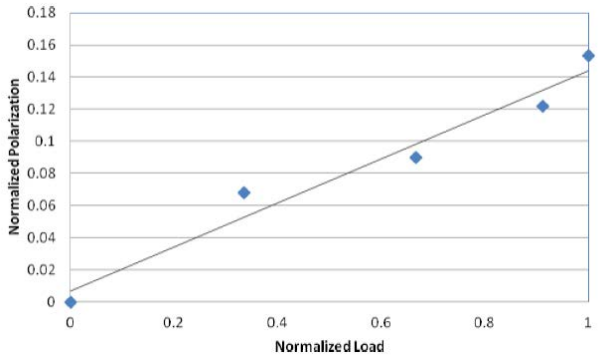

Figure 3.13 Normalized polarization vs. Normalized load (dots) with its trend line (solid line) (Hurlebaus 2011)

3.7 NONLINEAR ULTRASONIC METHOD

Bartoli et al. (2010) and Nucera et al. (2012) proposed the use of nonlinear ultrasonic guided waves to determine the RNT. The methodology was demonstrated numerically by means of the Semi-analytical Finite Element (SAFE) method (Figure 3.14) and experimentally (Figure 3.15). The SAFE method was developed to model the propagation of high-frequency waves in waveguides of arbitrary geometry and it is very effective when analytical solutions are not available or three-dimensional finite element analysis becomes too intensive.

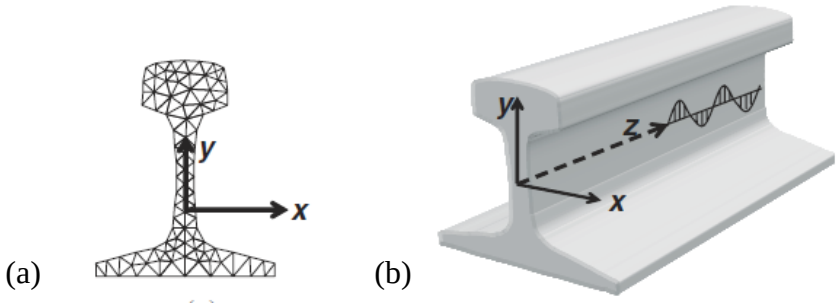

Figure 3.14 SAFE model for wave propagation in rails: (a) mesh plot of the rail cross section by 2-D Finite Element Analysis; (b) assumption of harmonic motion along propagation direction (Bartoli, 2010)

Experimentally, the method is based on the extraction of one or more features associated with the nonlinear component of the propagating guided wave and display the dependency of these features to the rail temperature. Figure 3.15(a) show a typical wave recorded experimentally whereas Figure 3.15(b) shows a nonlinear guided-wave parameter as a function of the longitudinal thermal strain. Figure 3.15(b) shows that the nonlinear guided wave parameter has a minimum at the zero strain, i.e. the method is effective at determining the RNT. The tests conducted in large scale test-bed indicate a 2 ^{o}F accuracy of the RNT measurement.

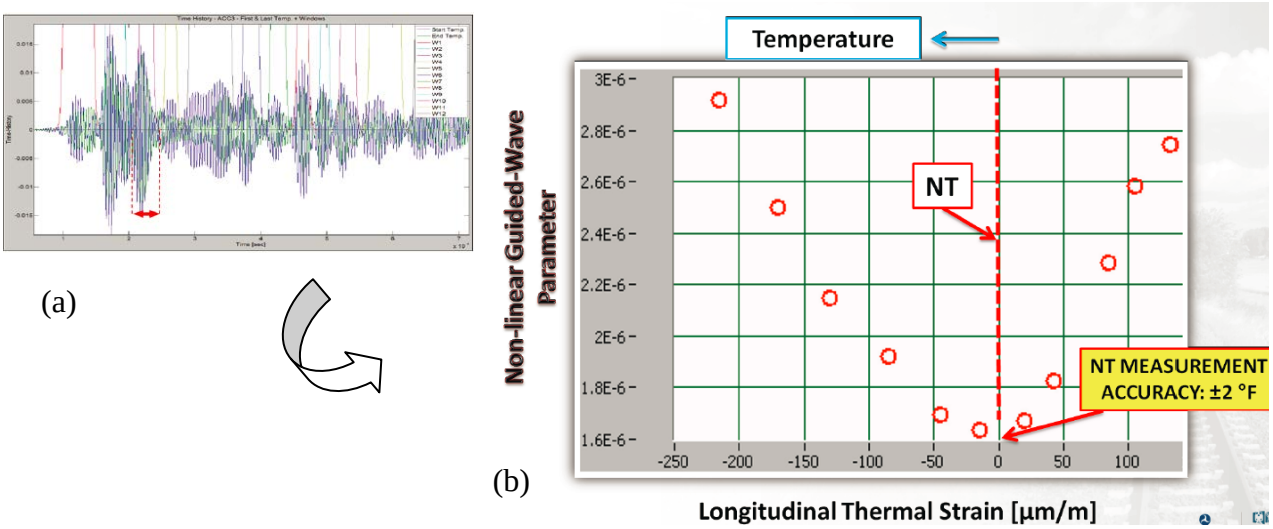

Figure 3.15 (a) waveforms cut to extract wave features; (b) Nonlinear guided wave parameters vs. Longitudinal thermal strain (Lanza di Scalea 2012)

4.0 HIGHLY NONLINEAR SOLITARY WAVE

In the last fifteen years, numerical and experimental studies on the propagation of nonlinear solitary waves in one-dimensional chains of spherical elastic beads have demonstrated that these waves can be used in several engineering applications, including but not limited to vibration absorbers (Fraternali, et al. 2009), impurity detectors (Sen et al. 1998, Hong and Xu, 2002), acoustic diodes (Nesterenko et al. 2005, Boechler et al. 2011) and nondestructive testing (Ni et al. 2012a, Ni and Rizzo, 2012b; Yang et al. 2012a). In chains of particles, the nonlinearity arises from a Hertzian-type contact between adjacent spheres subjected to compressive force. When the compression is small compared to the dynamic force associated with the propagation of the wave, HNSWs arise (Nesterenko, 1983, Lazaridi and Nesterenko, 1985, Nesterenko et al. 1995, Coste et al. 1997, Coste and Gilles, 1999, Daraio et al. 2005, 2006a, b, Job et al. 2005, 2007, Nesterenko et al, 2005, Yang et al. 2011, Carretero-González et al. 2009, Ni et al. 2011a, b). One peculiar characteristic of HNSWs is that their spatial wavelength is fixed (equal to approximately five particle diameters) and is independent of their amplitude. Moreover, the amplitude, speed and number of pulses can be tuned by engineering the granular system; for example, by changing the diameter of the bead or adding static pre-compression.

In the study presented in this chapter we coupled a chain of particles to a prismatic beam to evaluate the effect of the beam's geometry and material as well as the effect of thermal stress, on the characteristics of the solitary waves propagating along the chain. The objective of the

study is to investigate the hypothesis that HNSWs can predict the occurrence of thermal buckling in slender beams. Job and Melo (2005) studied the solitary reflection from walls having different mechanical properties. Yang et al. (2011) investigated the interaction of a 1-D granular system aligned with small cylinders of varying length and materials. The interaction between HNSW and thin plates was instead examined by Yang et al. (2012b) to evaluate the effect of the plate's boundary conditions.

We investigated different beam configurations numerically and experimentally. A discrete particle model was used to derive the shape and amplitude of the force function at the chain-beam interface. A continuous beam theory was used to estimate the structural response of the beam subjected to the solitary pulse forcing function. The structural response served to predict the characteristics of the solitary waves generated by the impact of the vibrating beam to the chain.

This chapter is organized as follows. The background and the numerical model associated with the propagation of HNSWs are presented in Sections 4.1 and 4.2, respectively. The response of the beam subjected to the impact of a solitary wave is described in section 4.3. Section 4.4 reports the numerical results associated with the sensitivity of the solitary wave to the beam's properties. Finally, Section 4.5 ends the paper with some conclusive remarks, the implications of our work, and the possible path for future research.

4.1 BACKGROUND ON HNSW

When two spheres are in contact and compressed by a static force F, as shown in Figure 4.1, their interaction is governed by the Hertz law (Landau and Lifshitz 1986):

$$F = \frac{1}{D}\left(\frac{R_1 R_2}{R_1 + R_2}\right)^{1/2} \delta^{3/2} \tag{4.1}$$

where R_1 and R_2 are the radius of the particles, δ is the distance of approach of their centers, and D is a coefficient given by:

$$D = \frac{3}{4}\left(\frac{1-\nu_1^2}{E_1} + \frac{1-\nu_2^2}{E_2}\right) \tag{4.2}$$

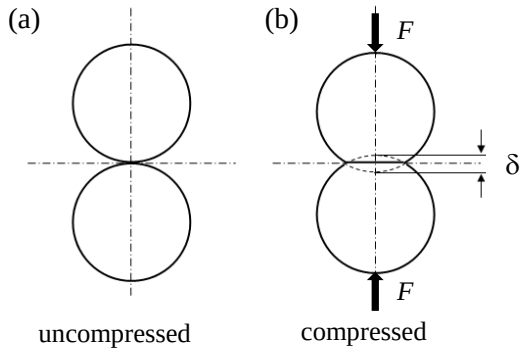

Figure 4.1 Schematics of two spheres that are (a) in contact, and (b) in contact and subjected to compression. The parameter δ is the approach of the two spheres' centers. (Figure adapted from Ni 2011c).

where E and ν are the Young's modulus and the Poisson's ratio of the material, respectively. Equation (4.1) can be generalized as:

$$F = A\,\delta^{3/2} \tag{4.3}$$

where

$$A = \begin{cases} A_c = \dfrac{E\sqrt{2R}}{3(1-\nu^2)} \\ A_w = \dfrac{4\sqrt{R}}{3}\left(\dfrac{1-\nu^2}{E} + \dfrac{1-\nu_w^2}{E_w}\right)^{-1} \end{cases} \tag{4.4}$$

In Equation (4.4) the stiffness constant A_c refers to the contact between two identical spheres, whereas A_w refers to the contact between a sphere and a semi-infinite wall. In this case,

E_w and ν_w represent the Young's modulus and the Poisson's ratio of the wall material. Figure 4.2 shows the schematics of the portion of a 1-D chain made of identical beads having radius R, mass m, subjected to a static pre-compression force F_0, and initial approach δ_0. When this system is subjected to the dynamic force F_m generated by the propagation of a solitary pulse, the second Newton's law relative to the *i-th* particle can be written as (Nesterenko 1983):

$$\ddot{u}_i = \eta_c(\delta_0 - u_i + u_{i-1})^{3/2} - \eta_c(\delta_0 - u_{i+1} + u_i)^{3/2} \quad , \quad 2 \le i \le N-1 \tag{4.5}$$

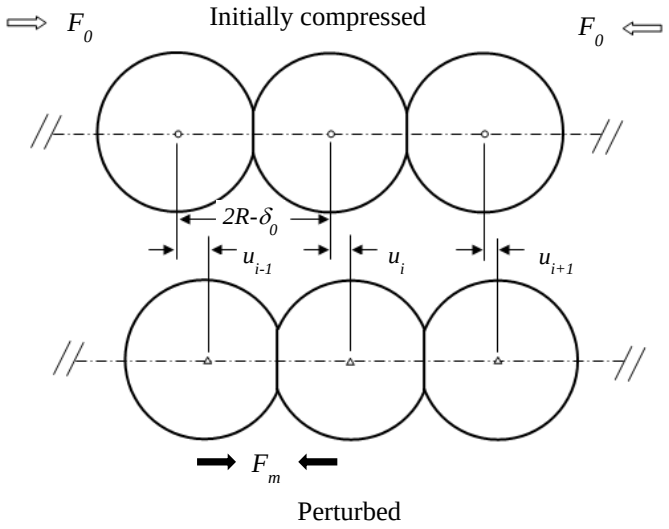

Figure 4.2 Top: chain of spherical particles subjected to static pre-compression F_0. Bottom: chain of spherical particles subjected to static pre-compression F_0 and removed from the equilibrium position due to the propagation of a solitary wave. The small circles represent the initial positions of beads' center whereas the triangles are the position of the beads' center after perturbation. F_m denotes the dynamic contact force associated with the propagation of a solitary wave. (Figure adapted from Ni 2011).

where u_i denotes the displacement of the i^{th} particle from its equilibrium position, and η_c is one of the stiffness constants defined in Equation (4.4) normalized with respect to the mass m, namely $\eta_c = A_c/m$. For the particles located at the two ends of the chain, i.e. when $i=1$ and $i=N$, Equation (4.5) becomes:

$$\ddot{u}_1 = -\eta_c\left(-u_2 + u_1\right)^{3/2} \tag{4.6a}$$

$$\ddot{u}_N = \eta_c(\delta_0 - u_N + u_{N-1})^{3/2} - \eta_w\left(\delta_{w0} - u_w + u_N\right)^{3/2} \tag{4.6b}$$

where δ_{w0} represents the initial approach between the last bead and the wall, and u_w is the displacement of the contact point on the wall, and η_w is the normalized stiffness constant $\eta_w = A_w/m$.

When the chain is "weakly" compressed, the particles displacement associated with the propagation of the wave is larger than the corresponding closest approach, i.e.

$$\frac{|u_{i+1} - u_i|}{\delta_0} \geq 1 \tag{4.7}$$

The time increment of the generic particles displacement can be expressed in terms of the Taylor series expansion as shown in Chatterjee (1999):

$$u(t+a) = u(t) + a\frac{du(t)}{dt} + \frac{a^2}{2!}\frac{d^2u(t)}{dt^2} + \frac{a^3}{3!}\frac{d^3u(t)}{dt^3} + \ldots \tag{4.8}$$

By substituting Equation (4.8) into Equation (4.5), the wave equation becomes:

$$\ddot{u} = c^2\left\{\frac{3}{2}(-u_x)^{1/2}u_{xx} + \frac{a^2}{8}(-u_x)^{1/2}u_{xxxx} - \frac{a^2}{8}\frac{u_{xx}u_{xxxx}}{(-u_x)^{1/2}} - \frac{a^2}{64}\frac{(u_{xx})^3}{(-u_x)^{3/2}}\right\} \tag{4.9}$$

where the subscript x indicats spatial derivatives and

$$c^2 = \frac{2E}{\pi\rho(1-\nu^2)}\ , \quad a = 2R \tag{4.10}$$

In Equation (4.9), u_x represents the strain, considered positive when the particle is compressed, and ρ is the density of the particle material (Nesterenko, 1983). The speed V_s of a solitary wave is (Nesterenko, 2001):

$$\begin{aligned} V_s &= \frac{c}{\xi_m - \xi_0}\left[\frac{2}{5}(3\xi_0^{5/2} + 2\xi_m^{5/2} - 5\xi_0^{3/2}\xi_m)\right]^{1/2} \\ &= \frac{c_0}{\xi_r - 1}\left[\frac{4}{15}(3 + 2\xi_r^{5/2} - 5\xi_r)\right]^{1/2} \\ &= 0.9314\left[\frac{4E^2F_0}{a^2\rho^3(1-\nu^2)^2}\right]^{1/6}\frac{1}{(f_r^{2/3} - 1)}\left[\frac{4}{15}(3 + 2\xi_r^{5/2} - 5\xi_r)\right]^{1/2} \end{aligned} \tag{4.11}$$

where ξ_m is total strain which includes initial strain due to static precompression and dynamically induced strain, ξ_r is the normalized maximum strain, i.e. ξ_m/ξ_0. The strain ξ_0 is the initial strain associated with the static pre-compression F_0, F_m is the maximum dynamic contact force, and f_r is the normalized force $f_r=F_m/F_0$. Equation (4.11) demonstrates that the speed has a nonlinear dependence on the strain or on the normalized force (Daraio et al. 2006b). The value c_0 represents the sound speed in a chain subjected to force f_r=1 and it is equal to (Nesterenko 2001, Daraio et al. 2006b):

$$c_0 = \left(\frac{3}{2}\right)^{1/2} c\xi_0^{1/4} = 0.9314\left[\frac{2E}{a\rho^{3/2}(1-\nu^2)}\right]^{1/3} F_0^{1/6} \tag{4.12}$$

where the constant c is indicated in Equation (4.10).

When the static pre-compression or its corresponding strain is small and therefore the dynamic characteristics F_m and ξ_m are large and the speed of solitary wave is:

$$V_s = \frac{2}{\sqrt{5}} c\xi_m^{1/4} = 0.6802\left[\frac{2E}{a\rho^{3/2}(1-\nu^2)}\right]^{1/3} F_m^{1/6} \tag{4.13}$$

and its shape can be closely approximated by (Nesterenko, 1983):

$$\xi = \left(\frac{5V_s^2}{4c^2}\right)\cos^4\left(\frac{\sqrt{10}}{5a}x\right) \tag{4.14}$$

4.2 DISCRETE PARTICLE MODEL

In this study the propagation of HNSWs in a weakly compressed 1D chain of particles was simulated numerically by using a discrete particle model (Nesterenko 2001, Yang et al. 2011, 2012b) where the interaction between two adjacent particles is confined to axial displacements

only and these displacements are much smaller than the particles' diameter. A diagram of a chain of *N* beads in contact with a linear medium is shown in Figure 4.3. The first particle represents the striker. Once the striker impacts the second particle, a solitary wave begins to form and propagate.

The second order differential Equation (4.5) was solved using the 4th order Runge-Kutta method. Thus, each equation was separated into two coupled 1st order differential equations about velocity *v* and displacement *u*:

$$\dot{v} = g(u) = \eta_c \left\{ \delta_{back}^{3/2} - \delta_{front}^{3/2} \right\} \tag{4.15a}$$

$$\dot{u} = f(v) = v \tag{4.15b}$$

where δ_{back} is the approach of the *i*-th bead with the previous one ((*i-1)th*) and δ_{front} represents the approach of the same bead with the next one ((*i+1)th*). The Runge-Kutta recurrence formula u_{k+1} and v_{k+1} were given as a timestamp of Δt:

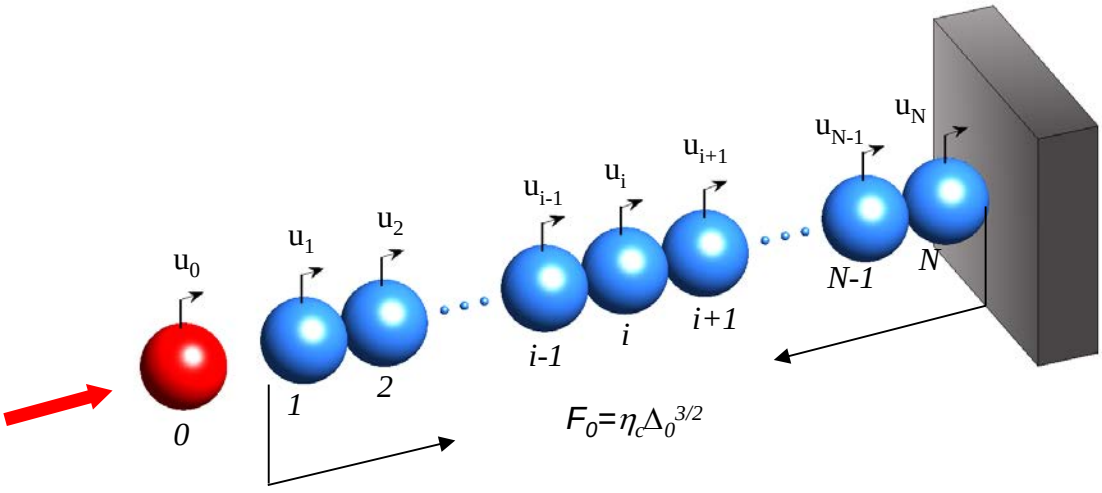

Figure 4.3 Schematics of a 1-D granular system in contact with a linear medium. The meaning of symbols is as follows. u_i: displacement of the i^{th} particle from its equilibrium position; F_0: precompression; δ_0: initial deformation induced by precompression; η_c: normalized sphere-sphere contact stiffness.

$$u_{k+1} = u_k + \frac{\Delta t}{6}(f_1 + 2f_2 + 2f_3 + f_4) \tag{4.16a}$$

$$v_{k+1} = v_k + \frac{\Delta t}{6}(g_1 + 2g_2 + 2g_3 + g_4) \tag{4.16b}$$

where the discrete increment *f* of the displacement are obtained from Equation (4.15b):

$$f_{1,i} = v_i\,, \qquad f_{2,i} = v_i + \frac{\Delta t}{2} g_{1,i}\,, \qquad f_{3,i} = v_i + \frac{\Delta t}{2} g_{2,i}\,, \qquad f_{4,i} = v_i + \Delta t \cdot g_{3,i} \tag{4.17}$$

and the velocity increments $g_{1,i}$, $g_{2,i}$, $g_{3,i}$, $g_{4,i}$ are derived from the Hertz law formulated in Equation (4.16a) as follows. For the striker:

$$g_{1,1} = -\eta_c [u_1 - u_2]_+^{3/2} \tag{4.18a}$$

$$g_{2,1} = -\eta_c [(u_1 + \frac{\Delta t}{2} f_{1,1}) - (u_2 + \frac{\Delta t}{2} f_{1,2})]_+^{3/2} \tag{4.18b}$$

$$g_{3,1} = -\eta_c [(u_1 + \frac{\Delta t}{2} f_{2,1}) - (u_2 + \frac{\Delta t}{2} f_{2,2})]_+^{3/2} \tag{4.18c}$$

$$g_{4,1} = -\eta_c [(u_1 + \Delta t \cdot f_{3,1}) - (u_2 + \Delta t \cdot f_{3,2})]_+^{3/2} \tag{4.18d}$$

For the 2nd through the (N-1)th bead:

$$g_{1,i} = \eta_c \{ \left[\delta_0 - (u_i - u_{i-1}) \right]_+^{\frac{3}{2}} - [\delta_0 - (u_{i+1} - u_i)]_+^{3/2} \} \tag{4.19a}$$

$$g_{2,i} = \eta_c \{ \left[\delta_0 - ((u_i + \frac{\Delta t}{2} f_{1,i}) - (u_{i-1} + \frac{\Delta t}{2} f_{1,i-1})) \right]_+^{\frac{3}{2}} - [\delta_0 - ((u_{i+1} + \frac{\Delta t}{2} f_{1,i+1}) - (u_i + \frac{\Delta t}{2} f_{1,i}))]_+^{3/2} \} \tag{4.19b}$$

$$g_{3,i} = \eta_c \{ \left[\delta_0 - ((u_i + \frac{\Delta t}{2} f_{2,i}) - (u_{i-1} + \frac{\Delta t}{2} f_{2,i-1})) \right]_+^{\frac{3}{2}} - [\delta_0 - ((u_{i+1} + \frac{\Delta t}{2} f_{2,i+1}) - (u_i + \frac{\Delta t}{2} f_{2,i}))]_+^{3/2} \} \tag{4.19c}$$

$$g_{4,i} = \eta_c \{ \left[\delta_0 - ((u_i + \Delta t \cdot f_{3,i}) - (u_{i-1} + \Delta t \cdot f_{3,i-1})) \right]_+^{\frac{3}{2}} - [\delta_0 - ((u_{i+1} + \Delta t \cdot f_{3,i+1}) - (u_i + \Delta t \cdot f_{3,i}))]_+^{3/2} \} \tag{4.19d}$$

For the sphere in contact with the beam:

$$g_{1,N} = \eta_c \left[\delta_0 - (u_N - u_{N-1})\right]_+^{\frac{3}{2}} - \eta_w [u_N]_+^{3/2} \tag{4.20a}$$

$$g_{2,N} = \frac{\eta_c}{m}\left[\delta_0 - ((u_N + \frac{\Delta t}{2} f_{1,N}) - (u_{N-1} + \frac{\Delta t}{2} f_{1,N-1}))\right]_+^{\frac{3}{2}} - \frac{\eta_w}{m}[u_N + \frac{\Delta t}{2} f_{1,N}]_+^{3/2} \tag{4.20b}$$

$$g_{3,N} = \frac{\eta_c}{m}\left[\delta_0 - ((u_N + \frac{\Delta t}{2} f_{2,N}) - (u_{N-1} + \frac{\Delta t}{2} f_{2,N-1}))\right]_+^{\frac{3}{2}} - \frac{\eta_w}{m}[u_N + \frac{\Delta t}{2} f_{2,N}]_+^{3/2} \tag{4.20c}$$

$$g_{4,N} = \frac{\eta_c}{m}\left[\delta_0 - ((u_N + \Delta t \cdot f_{3,N}) - (u_{N-1} + \Delta t \cdot f_{3,N-1}))\right]_+^{\frac{3}{2}} - \frac{\eta_w}{m}[u_N + \Delta t \cdot f_{3,N}]_+^{3/2} \tag{4.20d}$$

4.3 CONTINUOUS BEAM THEORY

In the general formulation of the continuous beam theory the equation of motion of a beam subjected to a transverse distributed force *F(x, t)* and an axial force per unit length *T*, which is considered positive when in tension (Chopra 2007, Tedesco et. al. 1999):

$$\left[EIy''(x,t)\right]'' + m \cdot \ddot{y}(x,t) - T \cdot y''(x,t) = F(x,t) \tag{4.21}$$

where *y(x,t)* is the vertical displacement, *m* is the mass per unit length, *EI(x)* is the flexural rigidity. By using the method of separation of variables as outlined in Tedesco et. al. (1999), the time-independent solution is given by:

$$y(x) = C_1 \sinh \lambda x + C_2 \cosh \lambda x + C_3 \sin \beta x + C_4 \cos \beta x \tag{4.22}$$

In Equation 4.22, $\lambda^2 = s_1^2$ *and* $\beta^2 = -s_2^2$, where:

$$s_{1,2}^2 = \frac{T}{2EI}\left[1 \pm \left(1 + 4m\frac{\omega_n^2 EI}{T^2}\right)^{1/2}\right] \tag{4.23}$$

and the constants C_1, C_2, C_3 and C_4 are evaluated by satisfying the specific boundary conditions. In the study presented in this chapter, fixed-fixed boundaries were considered, i.e.

$$y\big|_{x=0} = y\big|_{x=L} = 0 \tag{4.24a}$$

$$\left.\frac{\partial y}{\partial x}\right|_{x=0} = \left.\frac{\partial y}{\partial x}\right|_{x=L} = 0 \tag{4.24b}$$

From Equation (4.22, 4.23, 4.24a,b), infinite pairs of solutions about λ and β are derived and they represent an infinite numbers of mode shapes. Thus, the natural frequency of the beam can be computed as:

$$\omega_n = \frac{\beta_n}{\sqrt{m}}\sqrt{T + \beta^2 EI} \tag{4.25}$$

After algebraic manipulations, Equation (25) shows that when *T* is equal to the Euler buckling load ω_1=0, i.e. the beam does not vibrate.

We use normal modes $\phi_r(t)$ and normalized coordinate $q_r(t)$ as the *r*th solution of *f(x)* and *g(t)* separately, the general solution of Equation (21) is given by

$$y(x,t) = \sum_{r=1}^{\infty} \phi_r(x)\, q_r(t) \tag{4.26}$$

The differential equation of motion in normal coordinates for the *r*-th mode is:

$$\ddot{q}_r + \omega_r{}^2 q_r = \frac{1}{M_r}\int_0^L F(x,t)\,\phi_r(x)\,dx \tag{4.27}$$

where M_r is the generalized (modal) mass $M_r = \int_0^L m \cdot \varphi_r^2(x)dx$

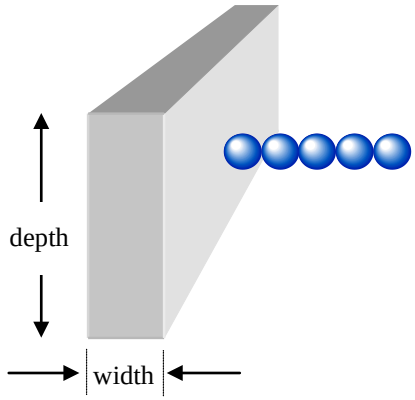

Figure 4.4 Schematics of the chain-beam system modeled to predict the effect of certain materials' parameters on the propagation of HNSWs features. Note that the chain of particles was made of 30 beads.

We coupled the continuous beam theory with the discrete particle model to predict the structural response of the beam subjected to a force function represented by the dynamic force of the solitary wave pulse arriving at the interface between the beam and the 1D chain of particles. To simulate such an interaction, the beam was virtually located at the $(N+1)^{th}$ position of the chain albeit it was not treated as a particle. Thus, the position u_{N+1} in Discrete Particle Model is equivalent to $y(x,t)$ of Equation (4.26) with the coordinate x coincident to the contact point between the chain and the beam in Figure 4.4. The beam acceleration $\ddot{u}_{N+1}$ is then:

$$\ddot{u}_{N+1}(t) = \ddot{y}(x,t) = \sum_{r=1}^{\infty} \phi_r(x)\ddot{q}_r(t) = \sum_{r=1}^{\infty} \phi_r(x)\left[\frac{1}{M_r}\int_0^L F(x,t)\phi_r(x)dx - \omega_r{}^2 q_r\right] \tag{4.28}$$

where the initial normal coordinate q_r at time t_0 is derived by the pre-compression from the chain of beads. From the model, the force applied to the beam by the solitary pulse is:

$$F(x,t) = A_w \delta_{N+1}{}^{3/2}\delta(x-a) \tag{4.29}$$

where δ_{N+1} is the approach between the last bead of the chain and the beam, and $\delta(x\text{-}a)$ is Dirac delta function which is nonzero at the interface point $x=a$.

4.4 NUMERICAL RESULTS

We used the formulation described in the previous two sections to evaluate the effect that mechanical and geometric properties of the beam in contact with a 1-D chain of particles have on certain parameters of the HNSWs propagating in the granules. The dynamical system is schematized in Figure 4.4. In all the simulations, the prismatic beam was 457 *mm* long, clamped at both ends, and placed in contact with the granular matter consisting of 30 beads. In most of the analyses each particle was 19.05 *mm* in diameter, weighing 29 *gr*, and its material had Young's modulus and Poisson's ratio of each particle equal to 200 *GPa* and 0.28, respectively. The first particle represented the striker and its initial velocity $\dot{u}_1$ was 0.240 *m/sec*. This value may be considered close to the experimental value 0.256 m/sec (see Section 6) and accounts for dissipative phenomena not modeled in the discrete particle model. Moreover, as will be discussed in the experimental results, the numerical value of 0.24 m/sec is such that the numerical and experimental amplitudes of the incident waves are very close.

The force profile associated with the propagation of the solitary pulse was measured at the center of the 5^{th} and 10^{th} particle away from the interface. These particles are hereafter indicated as sensor beads 2 (S2) and sensor bead 1 (S1), respectively. Four variables were simulated by means of the models discussed in the previous two sections. We evaluated the effect of the beam's Young's modulus and depth-to-width ratio, the effect of axial load applied to the beam, and we observed the effect of the particles diameter. For each variable, a range of values were considered. Table 4.1 summarizes the settings used in the numerical analyses.

Table 4.1 Parameters used in the numerical simulations.

Variables	Depth (mm)	Width (mm)	Beam's Young modulus (*GPa*)	Particle diameter (mm)	Axial load (kN)
Young's modulus	9.525	19.05	100, 120, …, 180, 220	19.05	0
Axial load	9.525	19.05	200	19.05	-12,-9,-6,…,+36
Depth-to-width ratio	9.525	9.525×(1,2,3,…,10)	200	19.05	0
Particle diameter	9.525	19.05	200	5,10,15,20,25	0

4.4.1 Effect of the Young's Modulus

The effect of the Young's modulus of a 9.525 *mm* wide, 19.05 *mm* deep beam was evaluated. The modulus varied from 100 *GPa* to 220 *GPa* at 20 *GPa* steps whereas the beam's density and Poisson's ratio were kept constant and equal to 7800 Kg/m^3 and 0.28, respectively. The numerical force profiles at 100 GPa and 220 GPa are shown in Figure 4.5. Three main pulses are visible. The first pulse is the incident wave (IW) generated by the striker and traveling towards the chain-beam interface. The subsequent pulse, the primary reflected solitary wave (PSW), is the wave reflected from the interface and propagating back through the granules and arriving at the sensor site. The mechanism that gives rise to the PSW is similar to what is described by Yang et al. (2012b) for chains in contact with plates: this wave is formed by the rebounding motion of granules against the beam; when the incident wave reaches the chain-beam interface, the last particle collides with the beam and is bounced back towards the rest of the chain. The third pulse, hereafter indicated as secondary reflected solitary wave (SSW), is the effect of the beam's motion. In fact, part of the acoustic energy carried by the IW triggers the vibration of the beam. Once the beam completes a half-cycle of its vibration, it impacts the chain giving rise to the

SSWs, visible after 3 *msec*. Thus, the TOF of SSWs is actually the half cycle time of the beam's first vibration mode.

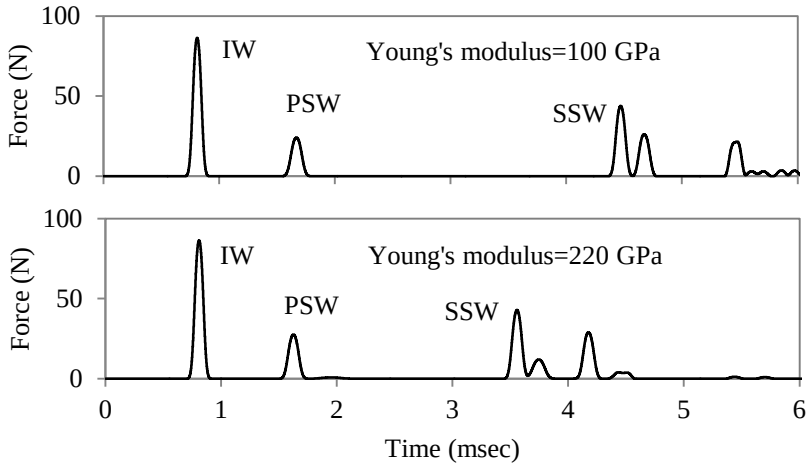

Figure 4.5 Numerical profile of solitary waves propagating in the granular chain in contact with a beam having Young's modulus equal to (a) 100 GPa and (b) 220 GPa.

Figure 4.5 shows that the most evident effect associated with the Young's modulus is the time of arrival of the SSW, whereas there is only a slight change on the time of arrival and amplitude of the PSW. We characterized the wave reflection properties measuring the following features: the time-of-flight (TOF), the amplitude ratio of the PSW, and the amplitude ratio of the SSW wave. The TOF denotes the transit time at a given sensor bead in the granular crystal between the incident and the reflected waves. We defined the amplitude ratios associated with the PSW and the SSW as the ratios of the PSW amplitude divided by the incident wave amplitude and the ratio between the SSW amplitude and the incident wave amplitude, respectively.

To quantify the effect of the beam's Young modulus on the selected features of the HNSWs, Figure 4.6 is shown. The results are presented in terms of the following parameters measured by means of sensor 1, located ten particles away from the interface: ratio PSW1 / IW1;

ratio SSW1 / IW1, time of flight associated with the primary reflected wave; time of flight associated with the secondary reflected wave. Figure 4.6a shows that as the linear medium becomes stiffer the amplitude of the primary reflected wave becomes larger, i.e. the ratio PSW1/IW1 increases. Figure 4.6b demonstrates that the difference in the time of arrival at the sensor site between the primary reflected wave and the incident pulse decreases. As the Young's modulus increases, the beam becomes stiffer, causing more energy to be reflected and less energy converted to beam's vibration. The decrease in the TOF has two causes: the decrease in the penetration depth of the last particle into the beam, the increase in speed of the PSW due to its raise in amplitude (Equation 4.13). As it pertains the secondary reflected wave, its amplitude does not follow a monotonous trend (Figure 4.6c), whereas the time of flight decreases as the modulus of the linear medium increases. The non-monotonous trend is due to fluctuation of the impact velocity of the beam with the chain. This velocity depends on the presence of higher symmetric vibration modes (the anti-symmetric modes have zero displacement at the mid-span). For the TOF of SSW, a larger Young's modulus induces a smaller vibration cycle time, which means a smaller TOF.

To better quantify the effects of the Young's modulus, the parameters discussed in Figure 4.6 were normalized with respect to their corresponding maximum and are presented in Figure 4.7. While the influence of the Young's modulus on the primary reflected wave can vary as much as 12%, the effect on the secondary wave is quite significant.

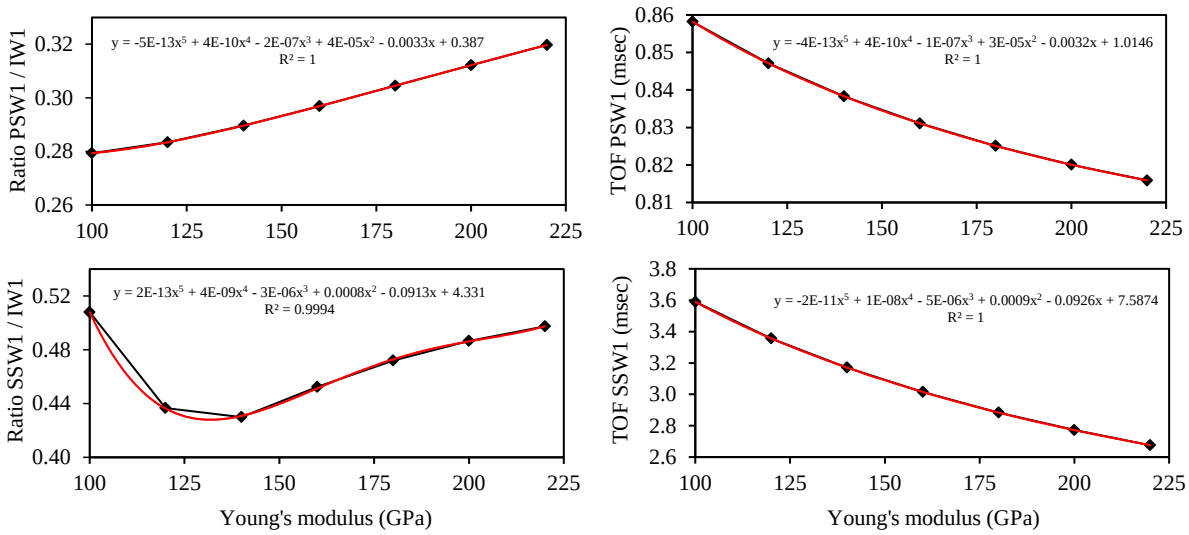

Figure 4.6 Granular medium in contact with a beam made of different elastic modulus. Solitary wave features measured by sensor S1 as a function of the Young's modulus. (a) Amplitude ratio of PSW. (b) Time of flight of PSW. (c) Amplitude ratio of SSW. (d) Time of flight of SSW.

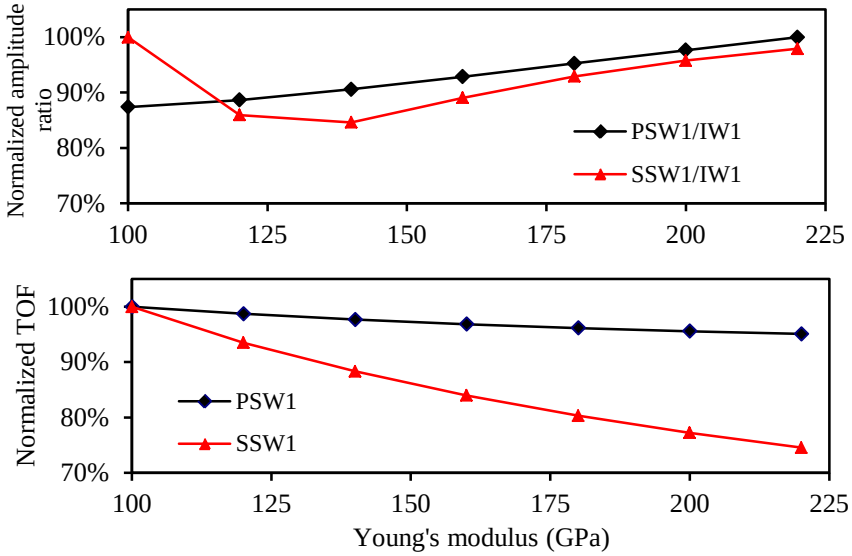

Figure 4.7 Granular medium in contact with a beam made of different elastic modulus. Solitary wave features relative to the primary and the secondary solitary waves measured by sensor S1 as a function of the Young's modulus. (a) Normalized amplitude ratio. (b) Normalized time of flight.

4.4.2 Effect of Axial Load

The effect of axial load on a rectangular beam (9.525 *mm* wide, 19.05 *mm* deep), density=7800 Kg/m^3, Young's Modulus 200 *GPa* and Poisson's ratio=0.28 was evaluated. The load was varied from 96% of the yielding load in tension to 96% of yielding in compression. It should be noted that the slenderness ratio of the beam was such that yielding stress is lower than buckling stress and therefore this particular beam fails occurs before buckling. Thus, for this specific case, the 96% yielding load in compression is equivalent to 69% buckling. The numerical force profiles at the two opposite cases are presented in Figure 4.8. The multiple peaks of SSW are caused by the impact between the bead and the beam (bottom panel) and the bouncing impacts of the sensor bead with adjacent beads (little flat peaks in the top panel). As for the effect of the axial load, the most evident difference between the force profiles is the time of arrival of the secondary reflected wave.

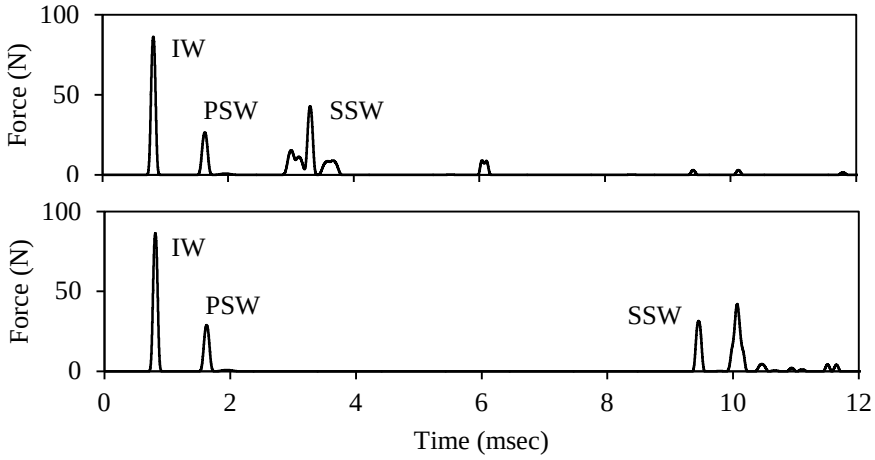

Figure 4.8 Numerical profile of solitary waves propagating in the granular chain in contact with a beam subjected to: (a) 36 kN tensile load; (b) 36 kN compressive load.

Figure 4.9 displays the HNSWs parameters as a function of the axial load. As it goes from compression to tension there is a change in the slope of both the amplitude and the time of flight of the primary solitary waves whereas similar consideration can be drawn for the time of flight of the secondary wave. The amplitude of the secondary wave seems to increase overall, though there is no monotonous trend. This is likely due to the disintegration of the secondary pulse into many pulses whose propagation speed and attenuation are significantly affected by the mechanical properties of the bounding medium (Job et al., 2005; Yang et al., 2011; Yang et al. 2012b).

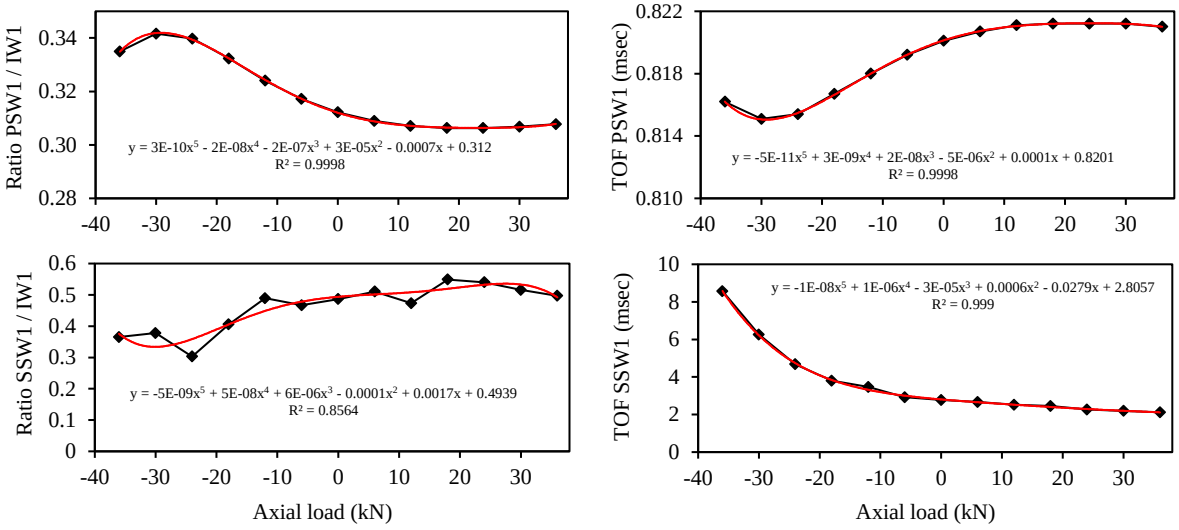

Figure 4.9 Granular medium in contact with a beam subjected to axial load. Solitary wave features measured by sensor S1 as a function of load. (a) Amplitude ratio of PSW. (b) Time of flight of PSW. (c) Amplitude ratio of SSW. (d) Time of flight of SSW. (Negative values indicate compression).

To better quantify the effects of the load, the parameters presented above were normalized with respect to their corresponding maximum value and they are displayed in Figure 4.10. The effect of the axial load on the amplitude of the primary reflected wave is in the order of 10%. Given that the largest load simulated in this study generates a stress equal to 193 *MPa*, the

sensitivity shown by the propagation of HNSWs to the presence of axial load can be exploited in the future as a mean to evaluate the presence of stress in a linear medium in contact with the granular system.

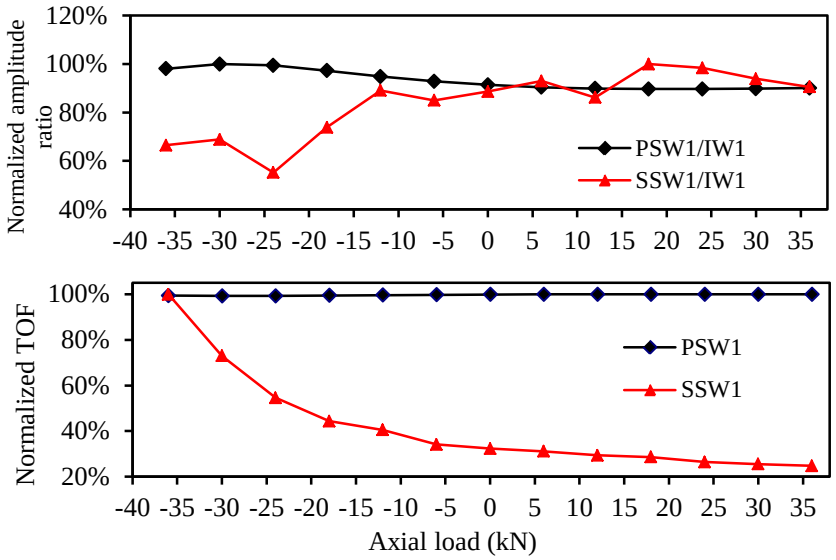

Figure 4.10 Granular medium in contact with a beam subjected to axial load. Normalized solitary wave features relative to the primary and the secondary solitary waves measured by sensor S1 as a function of the axial load. (a) Normalized amplitude ratio. (b) Normalized time of flight.

It is interesting to compare qualitatively the sensitivity to applied stress demonstrated by the HNSWs to the acoustoelastic phenomenon in which the speed of linear waves in a bulk medium or a waveguide depends upon the applied stress. For example, Rizzo and co-authors (Lanza di Scalea et al. 2003, Rizzo and Lanza di Scalea, 2003, 2004), found that the variation of the velocity of ultrasonic wave propagating in cylindrical waveguides made of high-strength steel is in the order of 1% per *GPa* of stress. This implies that the sensitivity to the presence of stress visible on the engineering system modeled in this paper is about 50-fold.

As it pertains to the response associated with the secondary wave, the variation of its time of flight is even larger although non-monotonic. Interestingly, the slope of the curve in the region

of positive load (beam in tension) is much smaller than the slope of the curve in the region of negative load (beam in compression). This could be exploited to assess the transition from compression to tension or vice versa. Finally, there is an apparent change in trend below -36 *KN*. We remark that an analysis at higher compression loads would be meaningless because the beam is not a linear medium and therefore the formulations outlined in the previous sections do not apply.

4.4.3 Effect of the Depth-to-Width Ratio

The effect of the flexural stiffness on the 457 *mm* long beam having density=7800 Kg/m^3, Young's Modulus 200 *GPa* and Poisson's ratio=0.28 was simulated. The flexural stiffness was varied by changing the moment of inertia of the beam. The width of the beam was kept constant and equal to 9.525 *mm* while the depth was varied, such that the depth-to-width ratio spanned from 1 (squared cross-section) to 10, at increment of 1. It is noted here that though the aspect ratio, like 10, makes the depth of the beam comparable with its length, we keep using the continuous beam model since we ignore any deformation of the cross section of the beam. The normalized values of the solitary wave features are presented in Figure 4.11. The data associated with the amplitude and the time of flight show a monotonous trend. When the beam is square most of the incident energy is converted into the secondary wave and only a small fraction of the incident energy is carried back by the primary reflected wave. This means that most of the incident wave energy is converted into the beam's vibration. As the amplitude of the PSW is small also its speed is small, yielding to the highest time of arrival. With the increase of depth, the flexural stiffness of the beam becomes larger and this creates larger bouncing back amplitude

which, in turns, generates larger PSW's velocity. The mechanism is similar to the one described by Yang et al. (2012b) to calculate the rebounding motion of a sphere in contact with a plate.

Similar to what observed in Figure 4.7, larger cross section decreases the penetration depth of the last bead into the beam and increases the velocity of the PSW.

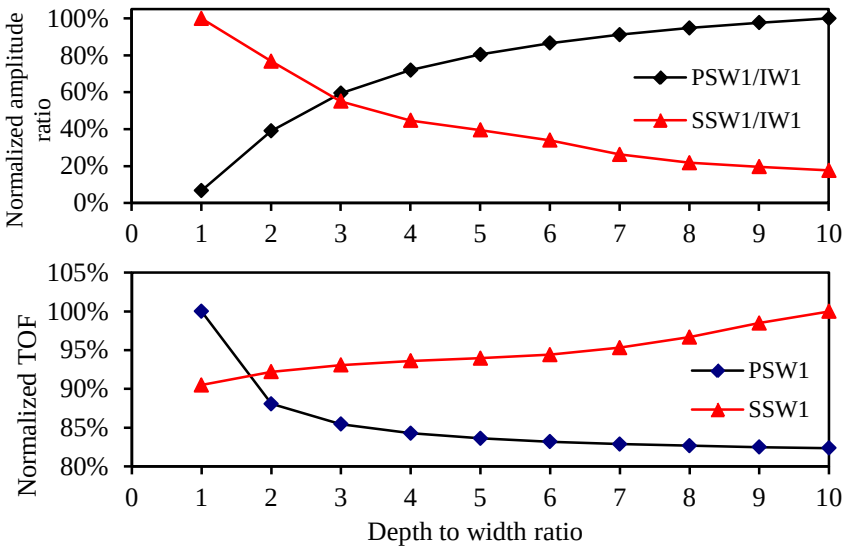

Figure 4.11 Granular medium in contact with a beam of varying depth-to-width ratios. Normalized solitary wave features relative to the primary and the secondary solitary waves measured by sensor S1 as a function of the depth-to-width ratio. (a) Normalized amplitude ratio. (b) Normalized time of flight.

4.4.4 Effect of the Particles' Diameter

The effect of the particles diameter on the characteristics of the HNSWs was considered as well. The characteristics of the beam were: rectangular cross section (9.525 mm wide, 19.05 mm deep), free length=0.457 *m*, density=7800 Kg/m^3, Young's Modulus 200 *GPa* and Poisson's ratio=0.28. Five particle's diameters were considered, namely 5 *mm* to 25 *mm* at 5 *mm* increment. The normalized values presented in Figure 4.12 show monotonous trends. For the 5 *mm* diameter case, the acoustic energy carried by the granular system is not sufficient to trigger the beam's

vibration, or to allow for penetration between the lost particle and the beam's surface. In this case we therefore we obtain perfect rebounding motion of the particle. Thus, no SSW was observed in this case. As the particles become bulkier, the amount of energy carried by the PSW decreases at advantage of the secondary wave. This is similar to the case of sphere diameter much larger than the plate thickness described in Yang et al (2012b). The phenomenon also produces a delay in the arrival time of the primary wave. The complementary response of the reflected waves is clearly visible in the amplitude feature (Figure 12a).

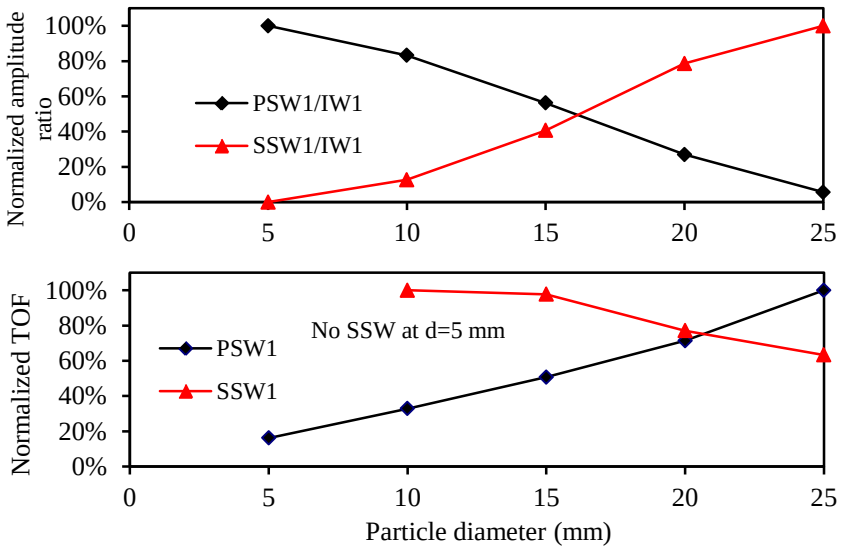

Figure 4.12 Granular medium made of different particle diameters in contact with a slender beam. Normalized solitary wave features relative to the primary and the secondary solitary waves measured by sensor S1 as a function of the granules dimater. (a) Normalized amplitude ratio. (b) Normalized time of flight.

4.5 EXPERIMENTAL STUDIES

4.5.1 Setup

Some of the numerical simulations discussed in Chapter 5 were validated by a series of experiments. The overall setup is presented in Figure 4.13. A chain of 30 beads (19.05 *mm*-diameter, 29 *gr*, low carbon steel beads, McMaster-Carr product number 9529K26) was embedded into a horizontal channel made of structural fiber glass square tube (having sides 25.4 × 25.4 *mm*, and wall thickness 3.175 *mm*, McMaster-Carr product number 8548K21). The first bead acted as a striker by means of the system shown in Figure 4.13b. The system consisted of an electromagnet made of a magnetic wire coil (AWG24) of about 1,350 turns wrapped around a 13 *mm* diameter and 33 *mm* long iron core. The electromagnet lifted the striker along a plastic slider. A DC power supply was used to provide electrical current to the coil. To prevent the movement of the first particle of the chain toward the slider, a small plastic sleeve was glued to the bottom of the electromagnet.

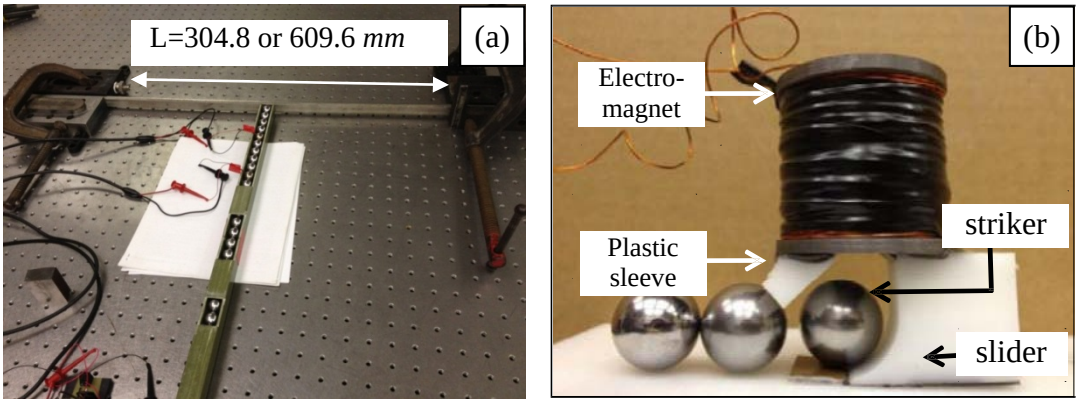

Figure 4.13 (a) Photos of the overall experimental setup. Granular system in contact with a beam made of different materials or different free-lengths. At each beam's end, two metallic plates are secured to the beam by means of a clamp to simulate fixed support. The free-span of the beam "sits" on two small supports to avoid any friction between the beam and the optical table. (b) Close-up view of the actuator used to set the motion of the striker.

The electromagnet was coupled to a switch circuit, driven by a National Instruments – PXI (PCI extensions for instrumentation) running in LabVIEW. Details of the control system are provided in (Ni and Rizzo, 2012b). A LabVIEW front panel was designed to operate the actuator automatically. The solitary waves were measured by using sensor beads located at 5^{th} and 10^{th} position away from the beam. Each sensor particle contained a piezoelectric ceramic disc (circular plate with 0.3 mm thickness and 19.05 mm diameter) with silver electrodes and micro-miniature wiring. The assembling and calibration procedures of the instrumented particles were similar to those described in (Daraio et al. 2005, Ni et al. 2011b, Cai et al. 2013a, b). The sensor particles were connected to the same NI-PXI and the signals were digitized at 10 MHz sampling rate. To assess repeatability, 50 measurements were taken for each case and processed statistically in Matlab. This assembly was successfully used in a recent study (Cai et al. 2013a).

The falling height of the striker was 4.7 *mm*. If rolling friction without slipping is assumed, the striker velocity v = 0.256 m/sec was derived from the conservation of energy:

$$mgh = \frac{1}{2}mv^2 + \frac{1}{2}\left(\frac{2}{5}mr^2\right)\cdot\left(\frac{v}{r}\right)^2 \tag{4.31}$$

where $(2/5)\times mr^2$ is the mass moment of inertia of a sphere.

4.5.2 Effect of flexural stiffness and free-length: setup and results

The first experiment aimed at evaluating the effects related to material type and geometry. In this series of tests, we examined: 1) the interaction between the HNSW transducer and two beams made of different materials, namely aluminum (McMaster-CARR product number 8975K794) and stainless steel (McMaster-CARR product number 8992K68); 2) the interaction between the

granules and beams made of the stainless steel having different free-lengths. Table 4.2 summarizes the properties of the two linear media.

Table 4.2 Geometric and material properties of the beams used in the experiments.

Material	Depth (mm)	Width (mm)	Length (mm)	Young's Modulus (GPa)	Poisson's ratio
Stainless steel	9.525	19.05	1829	200	0.28
Aluminum (Alloy 6061)	10.0	20.0	200	69	0.33

Prior to discussing the experimental results, Figure 4.14 presents the numerical force profiles associated with the stainless steel beam and the aluminum beam. Fixed-fixed boundary conditions were hypothesized. To ease visualization, the forces are offset by 100 N steps. Two interesting phenomena are observed. First, at the interface with the aluminum (Figure 4.14b), the PSW is not formed. The aluminum is much softer than the steel particles, and therefore most of the pulse energy carried through the chain is converted into the kinetic energy associated with the vibration of the beam. Second, the length of the free span affects the time of arrival of the secondary solitary wave. As the span increases the time of arrival of the SSW increases. This is related to the beam's natural frequency of vibration.

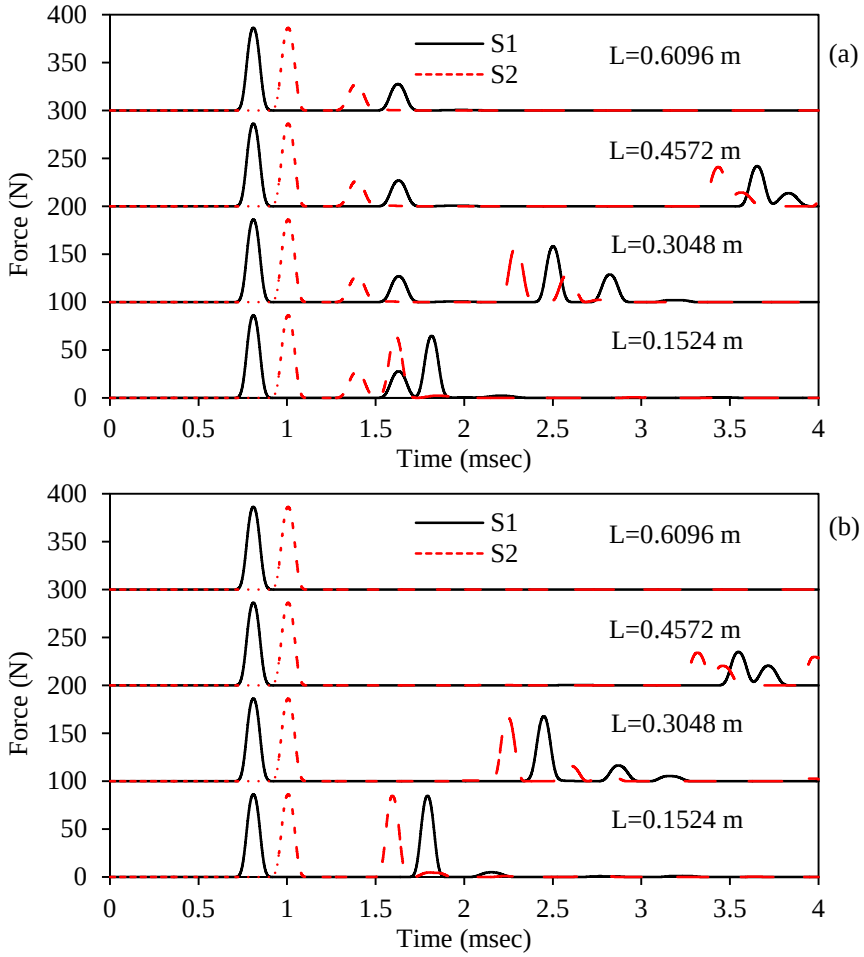

Figure 4.14 Numerical profiles of solitary waves propagating in a granular chain in contact with (a) stainless steel beam and (b) aluminum beam. The results relative to four free-lengths are displayed. The continuous lines refer to the measurements at the center of the particle located 10 particles away from the interface. The continuous lines refer to the measurements at the center of the particle located 5 particles away from the interface.

The experimental results are presented in Figure 4.15. Each panel displays the results associated with four free lengths, and the values of the dynamic forces measured by the bead sensors are offset vertically with a step of 100 *N*. Moreover, to ease the comparison with the numerical results, the trigger time of the experimental waveforms was offset horizontally as well. Overall, the experimental amplitudes of the reflected waves are smaller than the numerical predictions due to dissipative effects in the chain and in the beams. Moreover, the arrival of the SSW at the sensor site is delayed with respect to the numerical prediction. It is possible that the

system used in the setup to hold the beam cannot be idealized as fixed supports but rather as torsional springs.

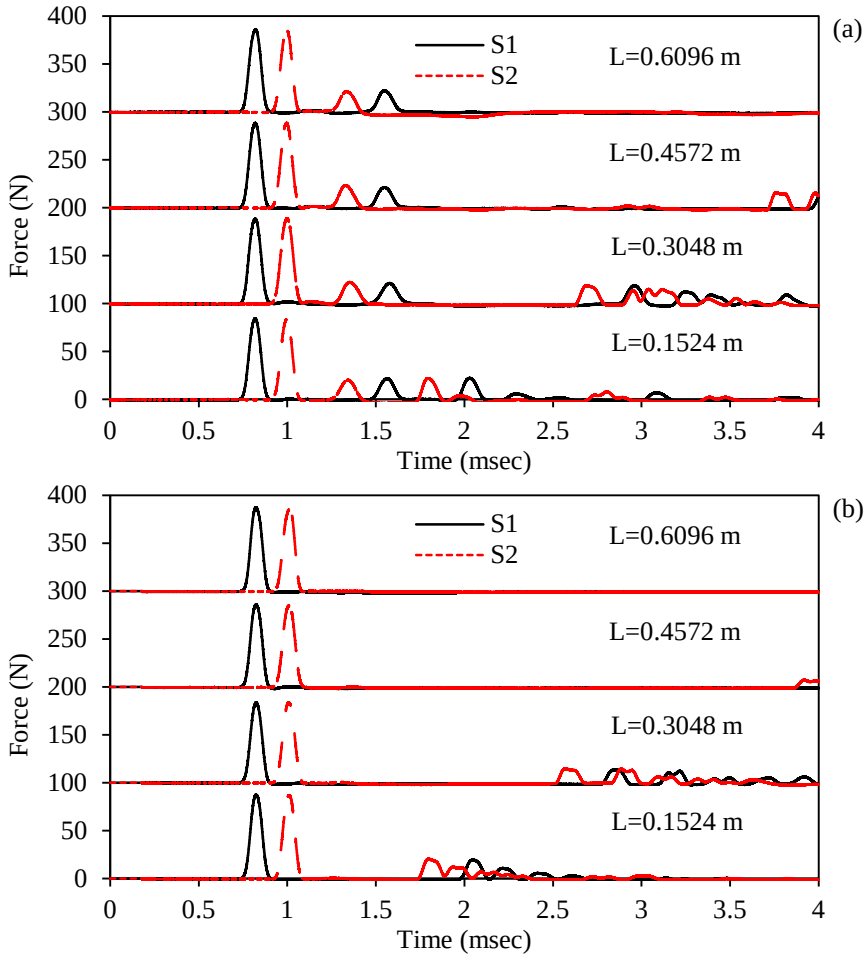

Figure 4.15 Experimental solitary waves propagating in a granular chain in contact with (a) stainless steel beam and (b) aluminum beam. The results relative to four free-lengths are displayed. The continuous lines refer to the measurements at the sensor bead located 10 particles away from the interface. The continuous lines refer to the measurements at the sensor bead located 5 particles away from the interface.

Figure 4.16 shows a few HNSW-based features as a function of the free-length of the stainless steel beam. As is said earlier, dissipative phenomena not included in the model are such that the experimental values are lower than the corresponding numerical prediction. Overall, the increase in free-length has a larger influence on the characteristics of the secondary wave and this is due to the natural frequency of vibration of the beam. As the free length increases, both

the beam's velocity and natural frequency of vibration decrease causing a delay on the time of arrival of the secondary wave and a decrease in amplitude.

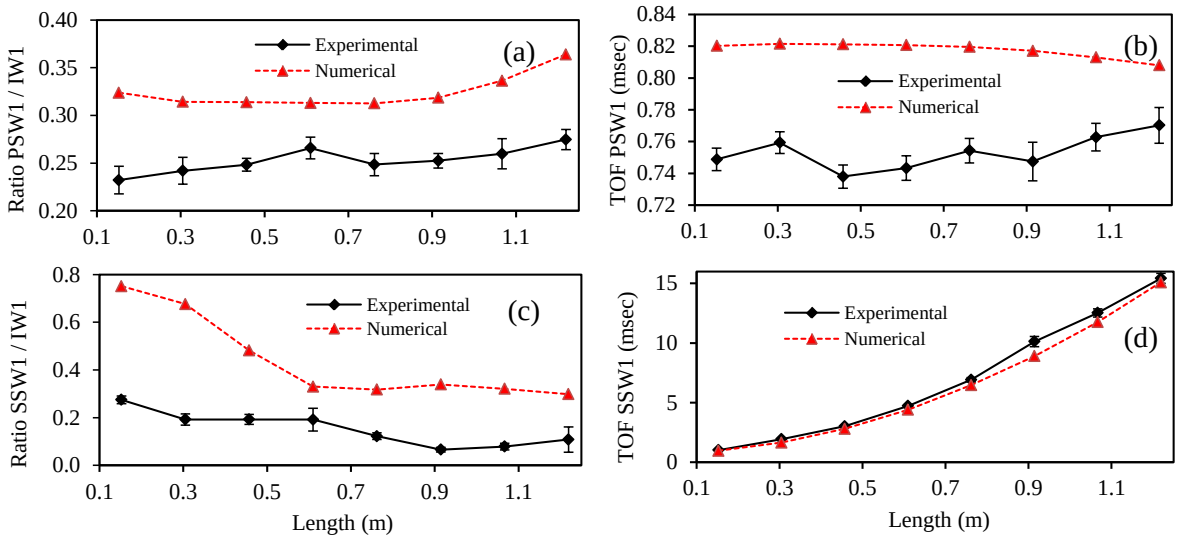

Figure 4.16 Solitary wave features measured by sensor S1 as a function of free length of the beam (a) Force ratio of PSW over IW at Sensor 1; (b) Time of flight between PSW and IW at Sensor 1; (c) Force ratio of SSW over IW at Sensor 1; (d) Time of flight between SSW and IW at Sensor 1.

4.5.3 Effect of thermal stress.

The steel beam was subjected to thermal load to validate the hypothesis that certain HNSW features can be used to predict incipient thermal buckling. The setup is presented in Figure 4.17. The beam's free length was equal to L=1.460 m and a thermal tape (McMaster-CARR product number 3631K63) was used to raise the temperature of the structure. A thermocouple and a strain gauge were used to monitor the beam's temperature and axial strain, respectively. The same granules illustrated in Section 6.1 were used to generate and detect solitary pulses. To assess repeatability, 15 measurements were taken at discrete temperature intervals.

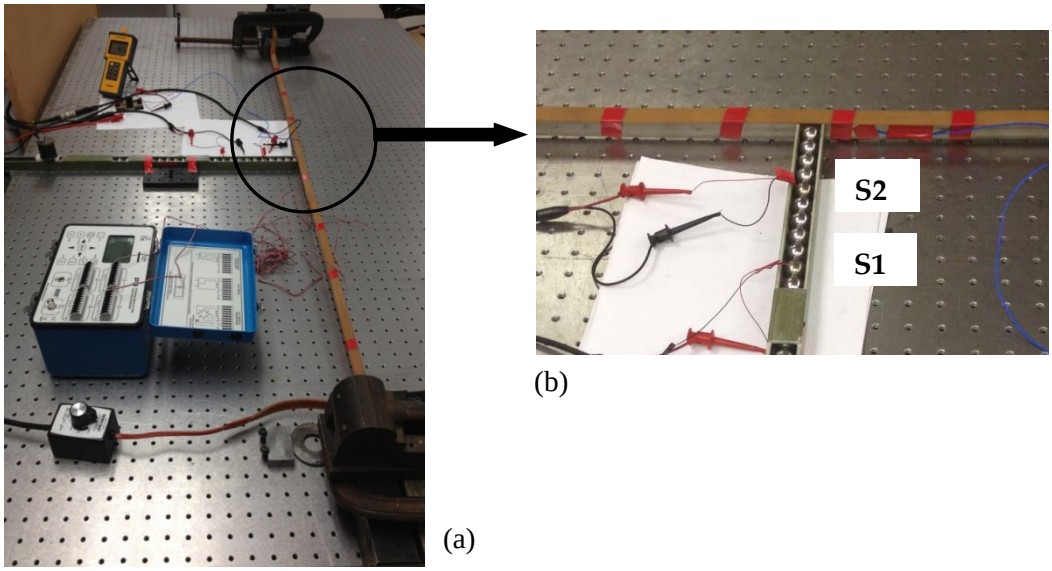

Figure 4.17 (a) Photos of the overall experimental setup. Granular system in contact with a beam subjected to thermal stress. The photo shows the beam's boundary conditions, a thermocouple, a heat tape, and a strain-gage box. (b) Close-up view of the chain-beam interface.

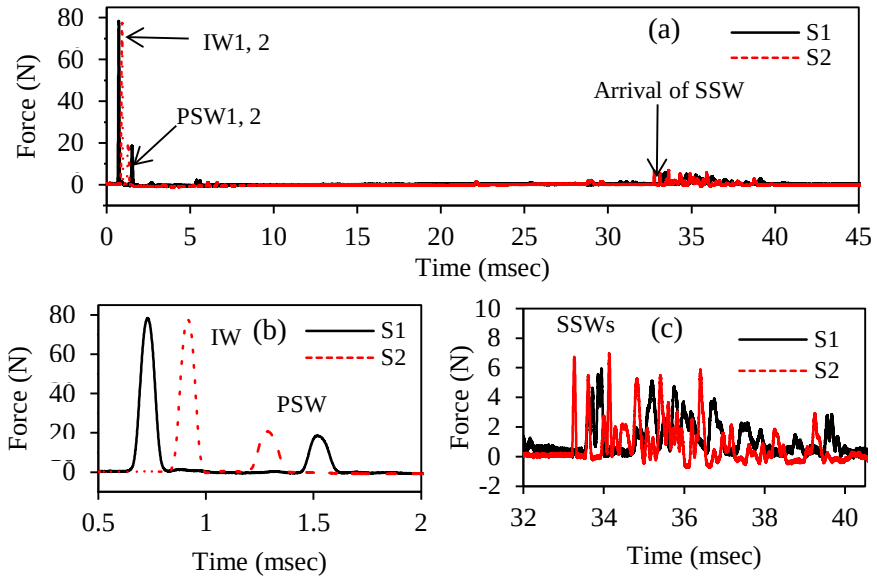

Figure 4.18 (a) Typical waveform of HNSW in thermal buckling test; (b) zoom-in plot of IWs; (c) zoom-in plot of SSWs

A waveform measured when the beam's temperature was 30.8 °C (ΔT = 8.4 °C) is shown in Figure 4.18a. The presence of the incident, primary reflected and secondary reflected waves is visible. The small pulses visible around 5 *msec* are due to the bouncing of the last particle of the

chain. Figure 4.18b and c are close-up views of Figure 4.18a. In Figure 4.18c multiple pulses are visible. After the beam vibrates back and triggers the SSW, the last bead in the chain is stopped again and again by adjacent beads, chased and impacted by the beam several times.

For an ideal stainless steel Euler-Bernoulli beam, 1.46 *m* long, and under fixed-fixed boundary conditions the thermal buckling is expected to occur when the temperature raise ΔT = 8.09 °C according to the Euler buckling load. This value is obtained considering the linear coefficient of thermal expansion α equal to 17.3×10^{-6} (1/°C) and Young's modulus E = 200 *GPa*. In the experiment, however, we observed large lateral deformation suddenly happening (buckling) when the temperature raise ΔT measured by the thermocouple was 29 °C. This discrepancy is mainly attributed to the uneven temperature distribution close to the boundaries and the fact that the boundaries are not ideally rigid in axial direction.

The thermal force *F* induced in the beam was computed from the strain ε measured by means of the thermally compensated strain gauges using the following relationship:

$$F = EA\cdot(\alpha\Delta T - \varepsilon) \tag{4.32}$$

where A is the area of the beam's cross-section. Figure 4.19 shows the time of flight associated with the secondary wave as a function of the axial force. The agreement between experimental and numerical results is very good. As explained in Section 4.4.1, the TOF of SSW is related with the natural frequency. From Equation 4.26 we know that the SSW arrives later when the axial compression increases and at buckling force, the natural frequency is zero which means the TOF of SSW should be infinite and this is also what Figure 4.19 indicates. Thus, we can predict the occurrence of the buckling when the time of flight of SSW approaches infinite.

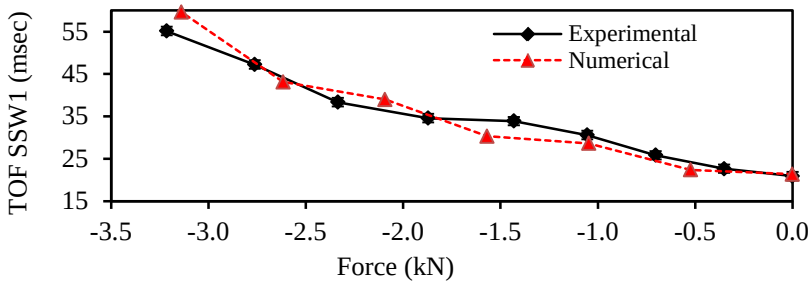

Figure 4.19 Time of flight of the secondary solitary wave measured by sensor bead 1 as a function of the axial load. Experimentally, at temperature raise above 27 °C the TOF of the secondary wave exceeded the time window (60 *msec*) of the digitizer. As such the experimental (and therefore the numerical) data relative to higher loads are not shown. (Negative values indicate compression).

Finally, the wave features as a function of temperature raise are presented in Figure 4.20. With the exception of the feature relative to the time of arrival of the SSW, the other three features do not show any specific pattern. This is likely due to the fact that the axial force generated on the beam is not sufficiently large. At ΔT = 27 °C, the compressive force is slightly above 3.0 *kN* which is a small fraction of the interval ± 35 *kN* examined in Figure 4.8-10.

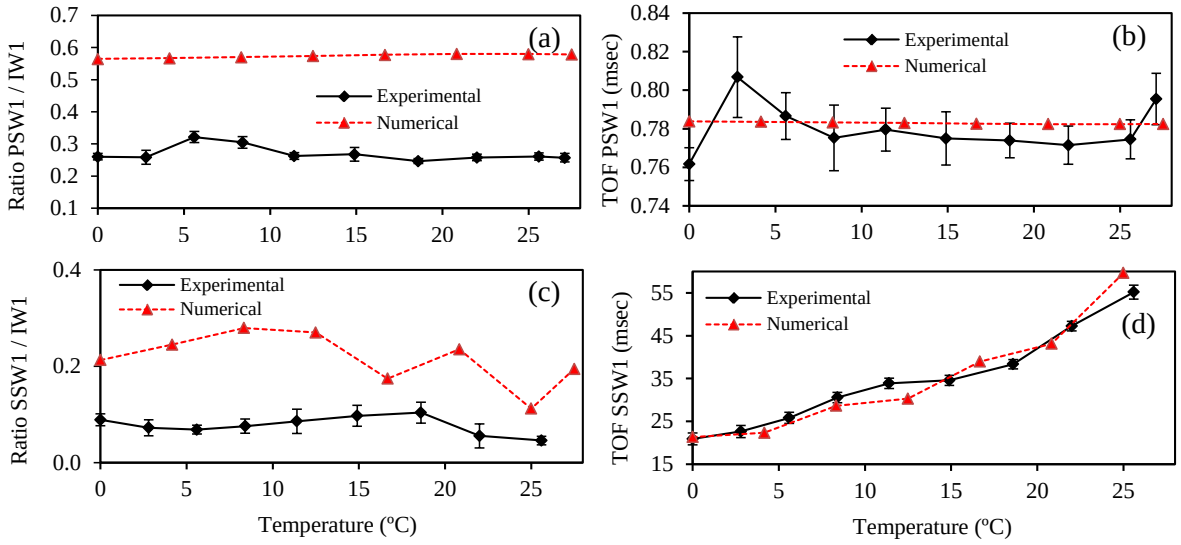

Figure 4.20 Granular medium in contact with a beam subjected to thermal load. Solitary wave features measured by sensor S1 as a function of load. (a) Amplitude ratio of PSW. (b) Time of flight of PSW. (c) Amplitude ratio of SSW. (d) Time of flight of SSW.

4.6 CONCLUSIONS

In the study presented in this chapter we investigated the interaction of highly nonlinear solitary waves with beams of different geometric and mechanical properties or subjected to thermal stress. The solitary waves propagated along a one-dimensional chain of spherical particles in contact perpendicular to the plane of the beam having minimum moment of inertia. We found that the waves reflected at the beam-chain interface are significantly affected by the geometry, material properties, and applied stress. In particular we found that both the time of flight and the amplitude of the waves are affected by the parameters investigated in this study. We quantified these dependencies numerically by coupling a discrete particle model to the continuous beam theory to evaluate the response of beam subjected to a forcing function equal to the solitary wave pulse profile. Some of the numerical models were validated experimentally.

Some of the findings of this study can be used to develop a novel nondestructive evaluation tool to predict the mechanical properties of beam structures and more important to predict incipient thermal buckling. With respect to ultrasonic methods based on acoustoelasticity, the proposed method may provide unique advantages in terms of larger sensitivity, portability, and cost. Future works shall focus on improving the numerical model to account for dissipative phenomena and on testing larger structures.

5.0 CURVED GRANULAR CHAIN

The applications of HNSWs for engineering systems have involved the use of straight 1-D arrays of particles. The physical mechanism of solitary waves' transmission in "deflected" or "curved" chains was unexplored until Daraio et al. (2010) reported flexible redirecting and splitting of solitary waves in a straight granular chain that diverges into two branches using Y-shaped guides. Yang et al. (2012a) studied the propagation of solitary waves in a curved granular crystal enclosed by flexible guides with the focus on the coupling between the granules and the deformable media for impact mitigation. However, no studies systematically characterized the effects of chain deflection and radius of curvature on the solitary waves' transmission and reflection.

In the framework of this project and in collaboration with California Institute of Technology (Caltech) and the University of South Carolina (USC), we investigated experimentally and numerically how the characteristics of solitary waves are affected by the geometry of a bent granular chain. Particularly, we evaluated the effect of the radius of curvature and the deflection angle between two straight granular segments on the transmission efficiency of the waves. For the experimental study, we connected two straight granular segments supported by modular guiding rails that could be configured in different curvatures and deflection angles. We measured the waves' characteristics using sensors located before and after the curved section of the chain. The results were compared with numerical simulations based on

a discrete element model that accounted for nonlinear and dissipative effects in the particles' interactions. We found that solitary waves propagate in a curved chain through the contact points between grains and maintain their compact shape. Even under drastic bends, such as 90° and 180° turns, the solitary waves preserved a significant portion of the momentum and energy. This suggests the use of granular chains as flexible wave-guides for momentum and energy transmission of elastic waves. If the granular chains exhibit sharp turns, with radii of curvatures as small as a one spherical particle's diameter, we observed that the solitary waves are partially transmitted across the bends and secondary reflected solitary pulses are formed. In the context of this project, the investigation of curved chains is essential to demonstrate that rails can be probed by placing a granular medium in contact with the web (see the setup presented in Ch. 8)

5.1 EXPERIMENTAL SETUP

To evaluate the effect of the granular chain's geometry on the propagation of HNSWs, we assembled modular guide rails in a variety of configurations. Each configuration was built by connecting two straight channels with curved rails, which had different radii of curvature and bend angles. Figure 5.1(a) displays one of the configurations used to evaluate the effect of the angle θ at constant radius of curvature R_c. The front and rear straight chains were composed of N_1 = 18 and N_3 = 15 spheres respectively, confined by structural fiberglass square tube (having sides 25.4 × 25.4 mm, and wall thickness 3.175 *mm*, McMaster-CARR product number 8548K21), with the first particle being the striker bead. The curved channels were made of Delrin acetal resin to reduce friction. The elastic modulus and Poisson's ratio of the Delrin guide were E_G = 3.2 GPa and ν_G = 0.35, respectively. The particles were stainless steel bearing-quality

balls (type 302, McMaster-Carr) with a diameter D = 19.05 mm, mass m = 29 g, elastic modulus E = 200 GPa, and Poisson's ratio v = 0.28. The number of particles (N_2) in the curved section was varied depending on the bend angle and the curvature.

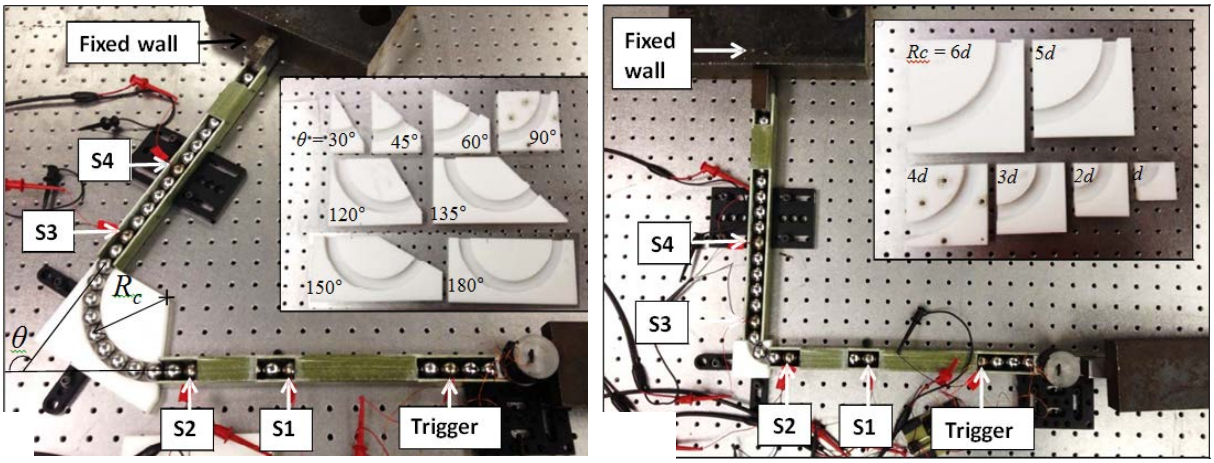

Figure 5.1 Digital images of the experimental setups. (a) Setup to study the effect of variable deflection angles θ at a given radius of curvature Rc. The setup presented in the photo has θ = 120° and a radius of curvature Rc = 4d (bead diameter d = 19.05 mm). The inset shows an assortment of eight different curved guide rails with θ = [30°, 45°, 60°, 90°, 120°, 135°, 150°, 180°] and Rc = 4d. (b) Setup to study the effect of different radii of curvature at a given deflection angle. The setup presented in the photo has θ = 90° and Rc = d (bead diameter d = 19.05 mm). The inset shows an assortment of six different guide rails with a right angle and Rc = [1, 2, 3, 4, 5, 6]×d. (Cai et al. 2013a)

We conducted two sets of experiments. In the first set, we investigated the effect of the deflection angle θ on the amplitude of the propagating solitary waves. We considered nine different angles (θ = [0°, 30°, 45°, 60°, 90°, 120°, 135°, 150°, 180°]) keeping the radius of curvature constant and equal to R_c = 76.20 mm. The photo of the setup is shown in Figure 5.1(a) with the different elbows presented in the inset. These angles tested correspond to N_2 = [1, 3, 3, 5, 7, 9, 9, 11, 13] included in the curved rail. To ensure the contact between adjacent particles, the whole system leaned against a reaction wall mounted at the end of the third segment.

In the second set of experiments, we systematically varied R_c in order to evaluate the effect of the chain's curvature on the solitary wave's properties. We devised six different segments that deflected the direction of the wave propagation by 90°. We considered R_c equal to

19.05 × [1, 2, 3, 4, 5, 6] mm. Figure 5.1(b) displays the setup and the different bent sections used. The corresponding number N_2 of beads along the curve was equal to N_2 = [1, 3, 5, 7, 7, 9]. The bent section with the largest radius of curvature ($R_c = 6d$) hosted nine spheres, while the smallest ($R_c = d$) contained only a single particle.

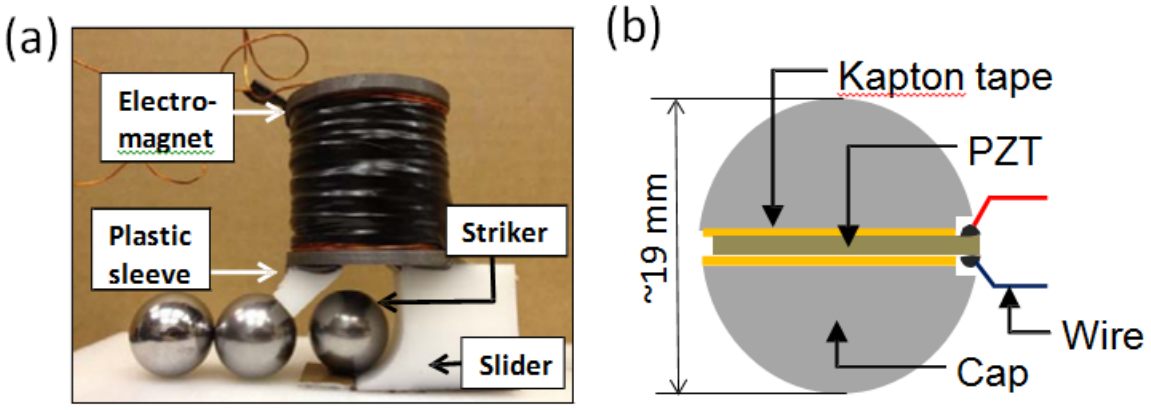

Figure 5.2 (a) Photo of the electromagnet employed to lift the striker particle along a plastic slider. (b) Schematic of a PZT-embedded sensor particle used for capturing the propagation of solitary waves. (Yang et al, 2011, Cai et al. 2013a)

For both sets of experiments, the solitary waves were excited by the transducer shown in Figure 5.2(a). It consisted of an electromagnet made of a magnetic wire coil (AWG24) of about 1,350 turns wrapped around a 13 mm diameter and 33 mm long iron core. The electromagnet lifted a striker particle (19.05 mm-diameter) along the plastic slider. A DC power supply (BK precision Model 1672) was used to provide electrical current to the coil. The drop height of the striker was 4.7 mm, resulting in the striker velocity v ~ 0.30 m/s. To prevent the movement of the first particle of the chain toward the slider, a small plastic sleeve was glued to the bottom of the electromagnet. As the electrical resistance of the coil depends on the coil temperature, the power supply was used in current control mode to keep the current constant. The electromagnet was coupled to a switch circuit, driven by a National Instruments – PXI running in LabVIEW. With

the switch closed, the electrical current passed through the coil allowing the motion of the striker. A LabVIEW front panel was designed to operate the actuator automatically.

Five sensor particles were assembled and used to measure the propagation of the HNSWs generated by the mechanical impact of the striker. Each sensor bead contained a piezoelectric ceramic disc (circular plate with 0.3 mm thickness and 19.05 mm diameter) with silver electrodes and micro-miniature wiring (Figure 5.2(b)). The assembling and calibration procedures of the instrumented particles were similar to those described in (Daraio, 2005). To quantify the effect of the geometry on the properties of the solitary waves, two sensor beads, namely S_1 and S_2, were positioned along the first segment at the 11^{th} and 16^{th} positions (see Figure 5.1). These sensors measured the characteristics of the solitary waves before they reach the elbow. Two sensors, S_3 and S_4, were positioned along the 2^{nd} and 7^{th} positions of the straight segment after the bend in order to capture the waveforms and to measure the wave's speed after the elbow. The sensor particles were connected to an oscilloscope and the signals were digitized at 10 MHz sampling rate. To assess repeatability, 50 measurements were taken for each case and processed statistically in Matlab.

5.2 RESULTS AND DISCUSSION

To predict and explain experimental results, a numerical simulation in Matlab was run by Prof. J. Yang at the University of South Carolina. In his simulation, the propagation of solitary wave in granular crystals was simulated using the discrete element model (DEM, similar with the discrete particle model introduced in Section 4.4, but in a curved channel and considering dissipation).

5.2.1 Effect of the deflection angle

Figure 5.3 shows the temporal force profile measured by the four sensor particles, normalized with respect to the force magnitude (A_{S1}) measured by the first sensor S_1, when $\theta = 0°$. The experimental results (presented with solid lines) are superimposed to the numerical results (presented with dotted lines). The profiles are shifted vertically to ease visualization. We observe the formation of a single compactly supported pulse. We find that the amount of attenuation of this incident solitary wave is not significant, as suggested by the ratios of the peak amplitude measured by the different sensors with respect to that measured by sensor S_1 (A_{s2}/A_{s1} = 0.984, A_{s3}/A_{s1} = 0.964, and A_{s4}/A_{s1} = 0.975). The solitary wave reflects from the hard wall positioned at the end of the rear segment, and it is again measured by the sensors as shown by the second pulse in each profile. The reflected pulse is followed by a smaller pulse which denotes secondary solitary waves generated at the rigid wall at the end of the chain. We find that the overall shape of the propagating pulses is identical throughout the chain, and the experimental and numerical

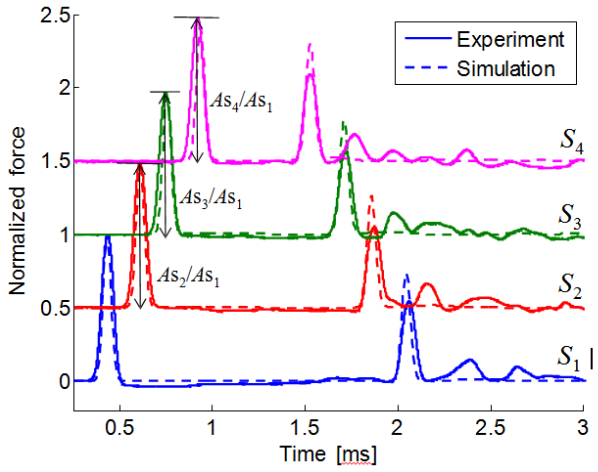

Figure 5.3 Temporal force profiles of solitary waves propagating along a straight granular chain (θ = 0°). Each force profile recorded from one of four sensors (S_1, S_2, S_3, and S_4) was normalized with respect to the maximum force magnitude of S_1 measurement (denoted as As_1), and is shifted vertically by 0.5 to ease visualization. Experimental and numerical results are represented by solid and dotted curves, respectively. (Simulation data provided by Prof. J. Yang, Cai et al. 2013a)

results are in very good agreement. The noticeable attenuation of the reflected solitary waves is due to losses at the end wall. As noted above, the numerical simulation was done by Prof. J. Yang at the University of South Carolina.

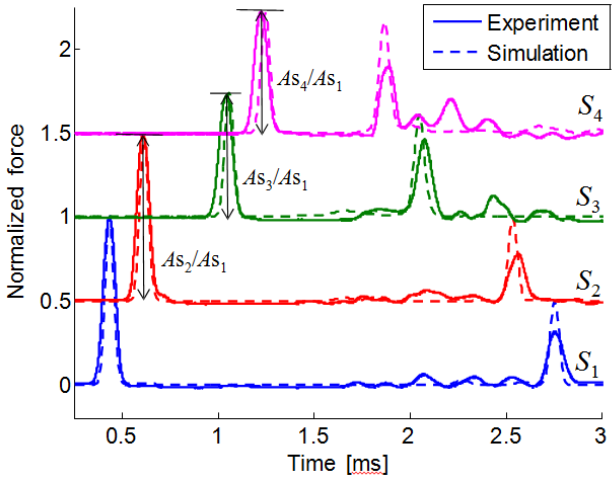

Figure 5.4 Temporal force profiles of solitary waves propagating along a curved granular chain with θ =90° and R_C = 6×d. We find that the amplitude of the solitary wave traveling after the curved section, measured by sensor beads S_3 and S_4 is attenuated noticeably. This is different from the conservative trend of solitary wave propagation in a straight chain in Figure 5.3. (Simulation data provided by Prof. J. Yang, Cai et al. 2013a)

The transmission of solitary waves through a 90°-curved chain is illustrated in Figure 5.4, which refers to R_c = 6d, where d = 19.05 mm is the bead diameter. Compared to the straight chain, we clearly observe the attenuation of solitary waves in the signals measured from S_3 and S_4 after the curved section. The normalized peak amplitude of sensors S_3 and S_4 are As_3/As_1 = 0.723 and As_4/As_1 = 0.722, respectively. Thus, it is evident that the presence of the 90° elbow mostly contributes to the decrease of the amplitude of the traveling wave. This is due to the loss of force components to the guiding rail through the lateral contacts in the curved section. A small fraction of the force loss is due to the presence of five more particles (when compared to the 0° case) between sensors S_2 and S_3. Despite the reduction in the force amplitude, we observe that the shape of the incident wave is preserved remarkably well after the bend, as shown in S_3 and S_4

signals around 1.0 and 1.2 ms-time. Moreover, there are negligible reflections generated by the elbow. Thus, it is demonstrated that the granular chains can efficiently transmit solitary waves without significant distortion even in a sharp turn such as 90°.

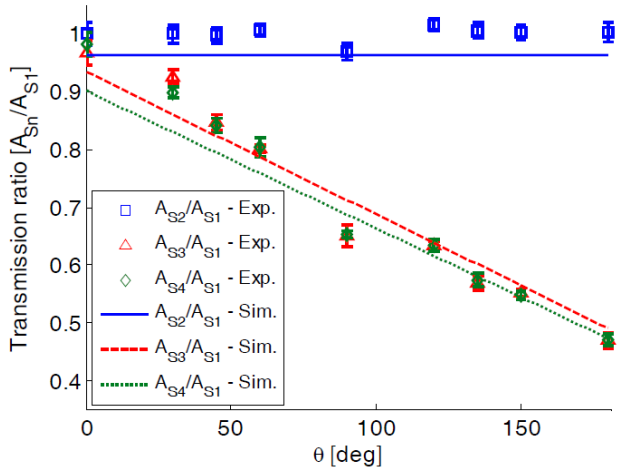

Figure 5.5 Transmission ratios of solitary waves through curved segments as a function of the deflection angle θ. The discrete points with error bars (95%-confidence interval) represent the experimental values, while lines denote numerical results obtained from DEM. (Simulation data provided by Prof. J. Yang, Cai et al. 2013a)

The transmission ratio of the solitary waves before and after the bent section was quantified for all nine deflection angles considered. Figure 5.5 shows the transmission ratio A_{Sn} / A_{S1} (n = 2, 3, 4) as a function of the angle θ. Each dot indicates the average value of the 50 measurements taken at each angle, and the vertical error bars denote a 95.5% (2σ) confidence interval. The barely visible error bars demonstrate the repeatability of the testing. Figure 5.5 shows that the amplitude of the solitary waves linearly decreases with the increase of the deflection angle. Notably, when the solitary wave is redirected by 90°, the transmission ratio is 0.65. At 180°-turn, 47% of the solitary wave's amplitude is transmitted to the rear straight segment. These experimental values are superimposed to the numerical results obtained using the DEM described in Section 5.3. We find that the numerical and experimental results are in excellent agreement. Note that rotational mechanics of granules was not taken into account in the

DEM model. This means that the primary mode of energy and momentum transmission in 1D granular chains is through axial contacts. Thus, the capability to transmit the wave along the chain is attributed to the axial "point" contact between granules, which leads to the formation of robust solitary waves. This is in contrast to random, dissipative granular architectures in which particles' rotational mechanics cannot be neglected.

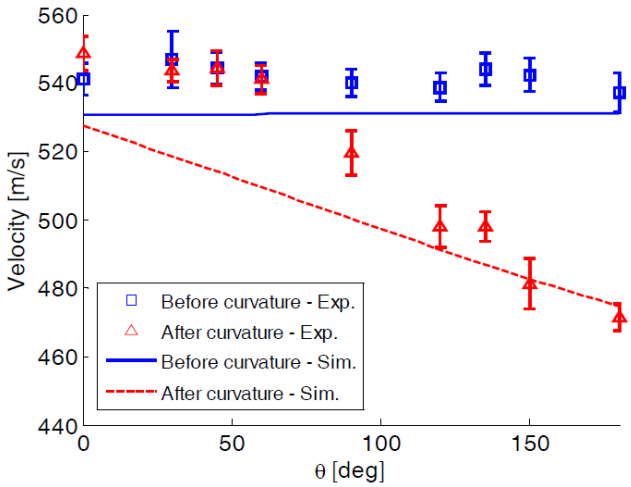

Figure 5.6 Velocities of solitary waves as a function of deflection angles θ, measured before (solid) and after (dashed) deflection. The discrete points with error bars (95%-confidence interval) represent the experimental values, while lines denote numerical results obtained from DEM. (Simulation data provided by Prof. J. Yang, Cai et al. 2013a)

The velocities of the solitary pulse before and after the curved segment are reported in Figure 5.6 as a function of the deflection angle. Experimentally, we observe a linear decrease of the speed. At 180°, the speed of transmitted solitary wave is about 13% lower than that of the straight chain. The general trend of the velocity curve is very similar to that of the transmission ratio in Figure 5.5. This is due to the unique nature of nonlinear waves that exhibit strong dependence of wave speed on its amplitude. In the case of highly nonlinear solitary waves, the wave's propagation speed, v_s, is related to the wave's maximum amplitude, F_m, as $v_s \sim F_m^{1/6}$ (Nesterenko 2001, Sen et al. 2008). We notice some discrepancies between the experimental and numerical results, though their responses are qualitatively similar. Such discrepancies might be

caused by the inaccurate simulation parameters, such as striker velocity and material properties, or by more complex dissipative effects in experiments than those accounted for in the numerical model.

5.2.2 Effect of the curvature

As summarized in Table 5-1, we studied six different radii of curvature (R_c) that deflected the trajectory of the wave propagation direction by 90°. The numerical and experimental normalized force profiles for the smallest R_c are presented in Figure 5.7. The amplitude of the traveling pulse measured by sensor S_2 is 99.2% of the amplitude measured by the first sensor, i.e. $A_{S2} / A_{S1} = 0.992$, and the wave maintains its robust, single-hump shape. The presence of the bend determined a significant attenuation. In fact, the relative amplitudes of the solitary waves' peaks were 0.390 and 0.384 respectively, when measured from S_3 and S_4. This is a further attenuation compared to the 90°-deflection with a larger radius of curvature ($R_c = 6d$).

Table 5.1 Geometric properties of the curved granular chains investigated in this study.

Experiment	N1	N2	N3	θ °	Rc (*mm*)
Set 1: effect of the deflection angle	18	1	15	0	76.20
		3		30	
		3		45	
		5		60	
		7		90	
		9		120	
		9		135	
		11		150	
		13		180	
Set 2: effect of the radius of curvature	18	1	15	90	19.05
		3			38.10
		5			57.15
		7			76.20
		7			95.25
		9			114.3

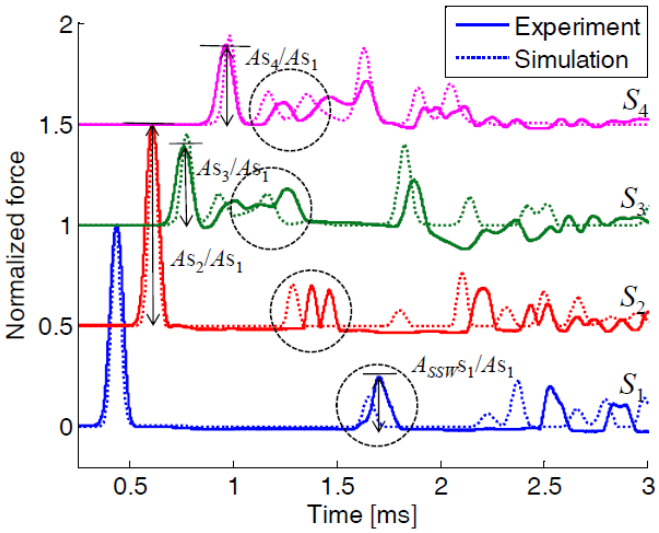

Figure 5.7 Temporal force profiles of solitary waves propagating along a curved granular chain with $\theta=90^o$ and $R = d$. Compared to the results from a larger curvature (e.g., $Rc = 6\times d$ in Figure 5.4), we find that the solitary waves are further attenuated after the deflection. The presence of secondary solitary waves generated by the elbow is emphasized with dashed circles. (Simulation data provided by Prof. J. Yang, Cai et al. 2013a)

In the bent chains tested in this study, the propagation of solitary waves is obstructed by the guiding structure. The momentum carried by the incident wave is split between the transmitted pulse and a secondary reflected solitary pulse, and it is also partially dispersed to the guiding material. If the curvature is low (i.e. if the radius of curvature is high), the interaction between the spheres and the rail is not significant, and no secondary pulses are formed (for example, when $Rc = 6d$). We found experimentally that the mechanism of formation of secondary waves at the elbow is not only affected by the chain curvature, but also by the deflection angle and the combination of spheres' and rail's material properties. According to the findings in (Yang et al 2011), we speculate that the softer the guiding rail is, the more likely is the secondary solitary wave's formation, due to the higher impedance mismatch between the particles and the rail.

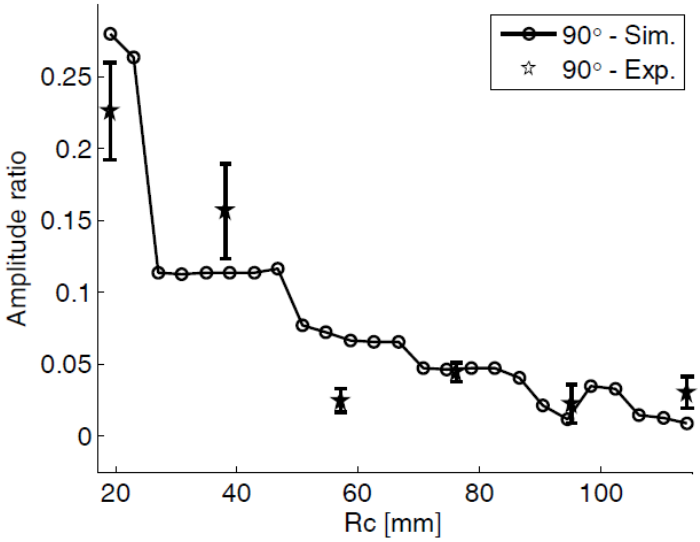

Figure 5.8 Amplitude ratios of secondary solitary waves relative to those of incident solitary waves. The circular dots connected with a solid line represent simulation results by Prof J. Yang, while star marks with error bars denote experimental data, all viewed from the sensor S_1. (Simulation data provided by Prof. J. Yang, Cai et al. 2013a)

We numerically calculated the ratios of secondary solitary waves' amplitude (A_{SSW,S_1}) to those of the incident waves (A_{s1}) based on the S_1 signals from a 90°-bend chain [see Figure 5.7]. The results are shown in Figure 5.8. As predicted, we observe larger magnitudes of secondary solitary waves for the granular chains with smaller radii of curvature. The sudden drops in the curves are caused by the discrete change of particle numbers in the curved section. Experimental data, marked in stars, follow the trend qualitatively. We also performed numerical simulations for other angles, and we found that the magnitudes of secondary solitary waves tend to increase as the deflection angle changes from 0° to 90°. However, beyond the 90° bend, there was no clear correlation between secondary solitary waves' amplitudes and the deflection angles.

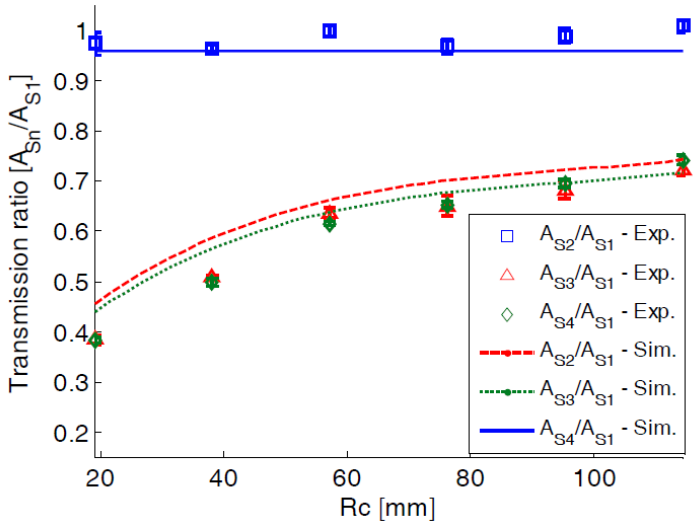

Figure 5.9 Transmission ratios of solitary waves through curved segments as a function of the radius of curvature R_c. The discrete points with error bars (95%-confidence interval) represent the experimental values, while lines denote numerical results obtained from DEM. (Simulation data provided by Prof. J. Yang, Cai et al. 2013a)

Figure 5.9 reports the transmission efficiency of solitary waves as a function of the radius of curvature. The amplitude of the pulse prior to the bend is almost one, showing negligible dissipation of the pulses in the straight segments, between the sensors S_1 and S_2. However, the amplitude of the pulse after the bend is reduced as the radius of curvature becomes smaller. We find that the experimental results (represented by the dots in Figure 5.9) match reasonably well the numerical results (represented by the curves). The noticeable discrepancy evident in the results obtained for the small radii of curvature might be originated from the tangential interactions of the particles in experiments, which were neglected in our numerical DEM approach. The velocities of the solitary waves before and after the various curvatures are plotted in Figure 5.10. For the chains with the larger curvatures (i.e., a sharp 90°-turn), we observe more reduction of the transmitted solitary waves' speed. Again, such decrease in speed is attributed to the attenuation of solitary waves due to the interaction with the curved mechanical channels.

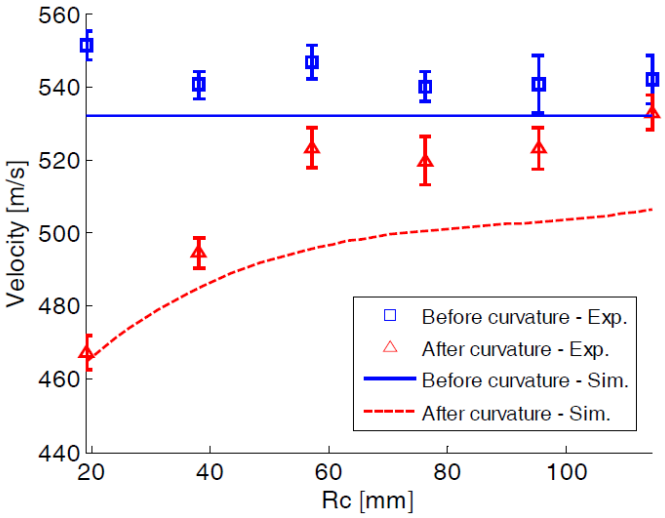

Figure 5.10 Velocities of solitary waves as a function of the radius of curvature *Rc*. The discrete points with error bars (95%-confidence interval) represent the experimental values, while lines denote numerical results obtained from DEM. (Simulation data provided by Prof. J. Yang, Cai et al. 2013a)

5.3 CONCLUSIONS

In this chapter, we investigated the propagation of highly nonlinear solitary waves in a curved chain composed of spherical particles. We characterized the effect of the bend's geometry on the amplitude and speed of the propagating waves. We systematically varied the deflection angle and the radius of curvature between two straight chains. Experimental results were compared to numerical results based on a discrete element model (DEM), which included dissipative losses in the axial interactions. We found that the attenuation of solitary waves is highly dependent on the chain deflection angles and curvatures. Notably, as a single pulse propagates through the bent chain, 71% of its initial force amplitude is preserved even under the 90° turn, and 50% of its force amplitude is preserved after a 180° turn. We also observed the formation of secondary

solitary waves in the chains with a sharp turn (i.e., a small radius of curvature) that are caused by interactions with the guiding rails.

Overall the measured transmission ratios for the curvatures tested were in the range of 40~70%, implying noticeable loss of energy through the bent chains. However, it should be noted that for a radius of curvature larger than approximately three times of the particle diameters, the original shape of a solitary pulse is well preserved without being disintegrated into a group of solitary waves. Thus, despite the loss of energy, such bent chains can serve as an information transmission line for engineering applications.

6.0 SENSORS TO MEASURE NONLINEAR SOLITARY WAVES

As is said earlier, it has been demonstrated that HNSWs propagating in granular crystals have the potential to be used as acoustic lenses (Spadoni and Daraio 2010), vibration absorbers (Fraternali et al. 2009), impurity detectors (Sen et al. 1999, Hong and Xu 2002), acoustic diodes (Boechler et al. 2011) and as a tool for nondestructive testing (Ni, 2012a, b, c; Yang, 2012c). In some of these engineering applications, the measurement of the dynamic force is necessary. To date, this measurement is attained either by means of one or more sensor beads placed in the chain (Daraio et al. 2005, 2006a,b, Job et al. 2005, 2007; Nesterenko et al., 2005; Yang, 2011; Carretero-González, 2009; Ni, 2011a, b) or by using a force sensor mounted at the base of the chain (Coste et al. 1997, Coste and Gilles 1999; Daraio et al. 2005, 2006a,b; Job et al. 2005). As shown in previous chapters, sensor beads usually consists of two half beads bonded to a thin piezoelectric crystal in order to form a sensor particle able to measure the dynamic force at its center. The main advantage of this assembly is two-fold: it can be placed anywhere in the chain; it does not alter the characteristics of the propagating wave, since the geometry and the material property of the sensor are essentially identical to those of the other particles composing the chain. However, the manufacture of sensor beads requires machining and therefore can be time-consuming and costly. Moreover, once in place, the bead should not be allowed to rotate in order to maintain its sensitivity constant and the wires are prone to accidental breakages. A force sensor instead measures the characteristics of the wave at the end of the chain. This configuration is unpractical

when the same end needs to be in contact with another material or structure. Finally, few studies exploited the photoelasticity to measure the mechanical wave propagation in photoelastic grains (Zhu et al. 1996; Geng et al. 2003). However, this approach is not suitable for metallic or other non-photoelastic materials and might be expensive.

In the study presented in this chapter, we investigated numerically and experimentally two alternative sensing systems to measure the propagation of solitary waves in a 1-D chain of metallic particles. The first design replaces the sensor beads with piezo rods having thickness and diameter comparable to the size of the particles composing the chain. The second system considers the use of coils wrapped around a segment of the chain to create a magnetostrictive sensor (MsS). The work presented in this chapter was reported in (Ni et al. 2013) and the figures shown in this Chapter were firstly published there.

6.1 EXPERIMENTAL SETUP

In order to compare the novel sensing systems to the conventional one, a plastic tube with inner diameter of 4.8 *mm* and outer diameter of 12.7 *mm* was filled with twenty nine 4.76 *mm*-diameter, 0.45 gr, low carbon steel beads (McMaster-Carr product number 96455K51). An identical bead was used as striker. For convenience, the particles are herein numbered 1 to 30 where particle 1 identifies the striker and particle 30 represents the sphere at the opposite end of the chain. The stroke of the particle 1, equal to 7.2 *mm*, was governed by an electromagnet mounted on top of the tube and remotely controlled by a switch circuit connected to a National Instruments PXI running in LabVIEW. Figure 6.1 schematizes the setup described above.

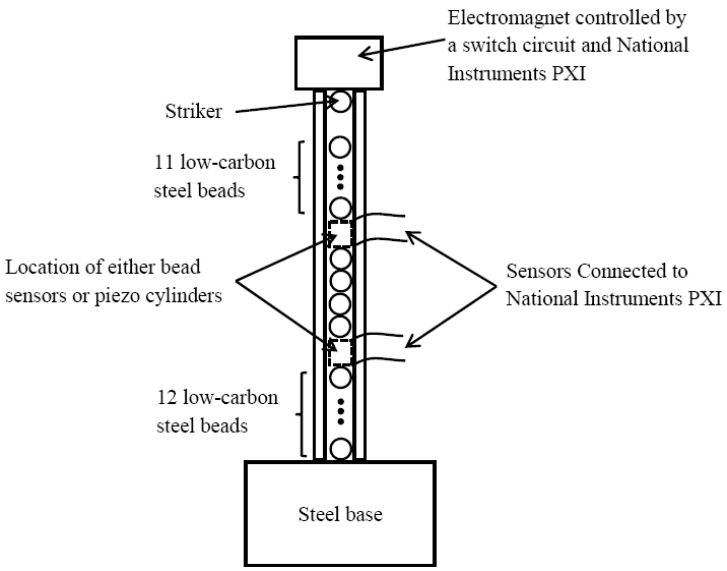

Figure 6.1 Schematic diagram of the experimental setup

Three pairs of sensors were used in this study: bead sensors, rod-form piezos, and MsSs. Each bead sensor was assembled by embedding a zirconate titanate based piezogauge (3 *mm* by 3 *mm* by 0.5 *mm*) inside two half steel spheres, as shown in Figure 6.2(a). They were located at the positions 13 and 18 in the tube. Figure 6.2(b) shows instead one of the two piezoelectric cylinders. They were custom made (Piezo Kinetics Inc. ND0.187-0.000-0.236-509) with 36AWG × 25.4 *mm* soldered tinned copper lead wires. The rods had nominal dimension 4.76 *mm* outer diameter and 6 mm height. According to the manufacturer, their mass was 0.8144 *g*, Young's modulus 63 *GPa*, and Poisson's ratio equal to 0.31. When they were used, the piezo cylinders replaced the bead sensors at location 13 and 18 in the tube. Finally, each MsS consisted of a 7 *mm* coil made of AWG36 magnetic wire and 1100 turns wrapped around a plastic tube having inner diameter of 12.7 *mm* and 1.6 *mm* thick. A permanent bridge magnet (McMaster-Carr product number 5841K12) was fixed to the coil as shown in Figure 6.2(c) in order to create a constant magnetic field parallel to the longitudinal axis of the chain. Figure 6.2(d) shows the schematic of the sensor once the plastic tube containing the chain of particles was inserted. The

two magnetostrictive transducers were mounted such that their centers were located at the same elevation of particles 13 and 18.

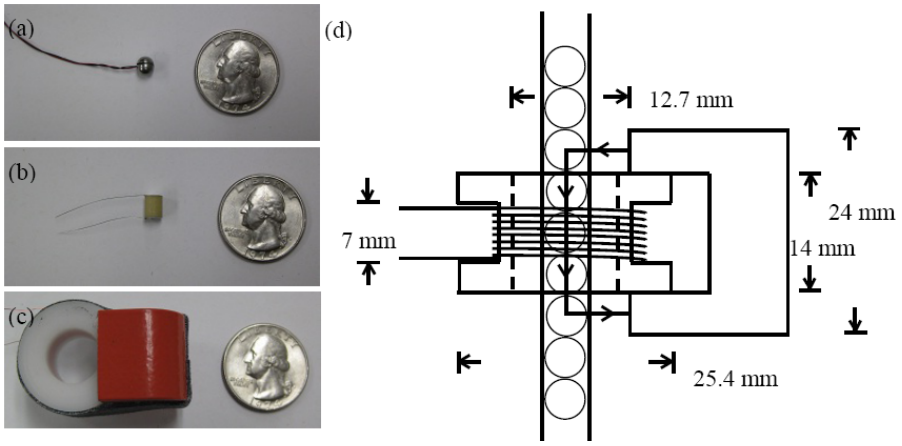

Figure 6.2 Sensing technologies used in this study. (a) Bead sensor formed by a thin piezoelectric crystal embedded between two half particles, (b) commercial piezo rod, (c) magnetostrictive sensor formed by a coil and a bridge magnet, (d) Schematic diagram of one magnetostrictive sensor assembled with the tube filled with spherical particles.

The capability and the repeatability to measure the amplitude and speed of the HNSWs was evaluated by taking 500 measurements at 10 *MHz* sampling rate for each sensing configuration.

6.2 BACKGROUND

A single solitary wave pulse is commonly induced by mechanically impacting the first bead of the chain with a striker having the same mass of the particles composing the chain. When a bead sensor is inserted in a chain, the force measured is the average of the dynamic forces at the bead's ends (Daraio et al. 2005). Similarly, the force measured by a piezoelectric cylinder is the

average of the dynamic forces at the two cross-section ends. Both sensing configurations are based on the use of piezoelectric crystals.

The MsS takes advantage of the efficient coupling between the elastic and magnetic states of the ferromagnetic particles and in particular of the magnetostrictive phenomena that convert magnetic energy into mechanical energy and vice versa (Calkins et al, 2007). The magnetostriction principle can be used in the active or in the passive mode based upon the Faraday's law and the Villari's effect, respectively. According to the Faraday's law an electrical current passing along a coil induces a magnetic field that is perpendicular to the current's direction. If the coil enwinds a ferromagnetic material, an alternating current passing through a wire creates a time-varying magnetic field within the coil that, in turn, produces a change of magnetostriction of the material. The subsequent deformation known as Joule's effect (Joule, 1847) produces a mechanical wave. According to the Faraday's law the voltage output in the coil can be expressed as (Calkins et al. 2007; Kleinke et al. 1994, 1996; Tumanski 2007):

$$V = -N\frac{d\varphi}{dt} \tag{6.1}$$

where V is the induced voltage in the coil, N is the number of turns of the coil, $\varphi = BS_c$ is the magnetic flux. Here B is the magnetic induction, S_c is the area of coil in the magnetic field. Equation (6.1) can be written as:

$$V = -NS_c\frac{dB}{dt} \tag{6.2}$$

The inverse mechanism can be used for the detection of waves. A pulse propagating in the ferromagnetic material modulates an existing magnetic field by means of the Villari's effect (Calkins et al. 2007; Villari 1865), thereby exciting a voltage pulse in the receiver coil. In both transduction and detection, a constant magnetic field (bias) is superimposed to enhance the

coupling between the elastic and magnetic states, *i.e.*, to increase the signal-to-noise ratio of the mechanical wave generated and detected by the magnetostrictive transducer. The magnetostrictive transducers have been designed, built and used for the generation and detection of ultrasonic guided waves in strands, solid cylinders, and pipes (Lanza di Scalea et al. 2003; Rizzo et al. 2004, 2005a, b, 2006, 2007).

In the design of the MsS used in the present study we exploited the Villari effect to detect the propagation of nonlinear solitary waves across the chain. The particles are the magnetostrictive material subjected to a biased magnetic field and are surrounded by a coil. We hypothesized that the change of the magnetic induction is proportional to the change of the dynamic contact force between neighboring particles. The output voltage was proportional to the time-derivative of dynamic contact force:

$$V \propto \frac{dF}{dt} \tag{6.3}$$

Therefore, the dynamic force associated with the solitary wave propagation is proportional to the integral of the sensor output voltage. Based upon the geometry of the MsS [see Figure 6.2(d)], we assumed that the permanent magnet biased four contact points, which implied that the dynamic force measured by the coils sensor could be reasonably considered the average of four dynamic forces at these points.

6.3 NUMERICAL MODEL

6.3.1 Formulation

The experimental setup was simulated using a chain of spherical particles in contact with a wall which was considered as a half-infinite medium, as shown in Figure 6.3. We adopted the discrete particle model (Nesterenko, 1983; Yang et al. 2011) to predict the characteristics of the nonlinear solitary pulses generated by the impact of a striker. In the model the motion of the particles was considered in the axial direction, and the interaction between two adjacent spheres was governed by the Hertz's law. The equation of motion of the i-*th* particle can be expressed as (Nesterenko 1983; Yang et al. 2011; Carretero-González et al. 2009):

$$m_i\ddot{u}_i = A_{i-1}\delta_{i-1}^{3/2} - A_i\delta_i^{3/2} + \gamma_{i-1}\dot{\delta}_{i-1} - \gamma_i\dot{\delta}_i + F_i \quad , \quad i = 1,2,\ldots,N \tag{6.4}$$

where:

$$A_i = \begin{cases} 0 & , \quad i = 0 \\ A_c = \dfrac{E\sqrt{2R}}{3(1-\nu^2)} & , \quad i = 1,2,\ldots,N-1 \\ A_w = \dfrac{4\sqrt{R}}{3}\left(\dfrac{1-\nu^2}{E} + \dfrac{1-\nu_w^2}{E_w}\right)^{-1} & , \quad i = N \end{cases} \tag{6.5}$$

$$\gamma_i = \begin{cases} 0 & , \quad i = 0 \\ \gamma_c & , \quad i = 1,2,\ldots,N-1 \\ \gamma_w & , \quad i = N \end{cases} \tag{6.6}$$

$$\delta_i = \begin{cases} [-u_1]_+ & , \quad i = 0 \\ [u_i - u_{i+1}]_+ & , \quad i = 1,2,\ldots,N-1 \\ [u_N]_+ & , \quad i = N \end{cases} \tag{6.7}$$

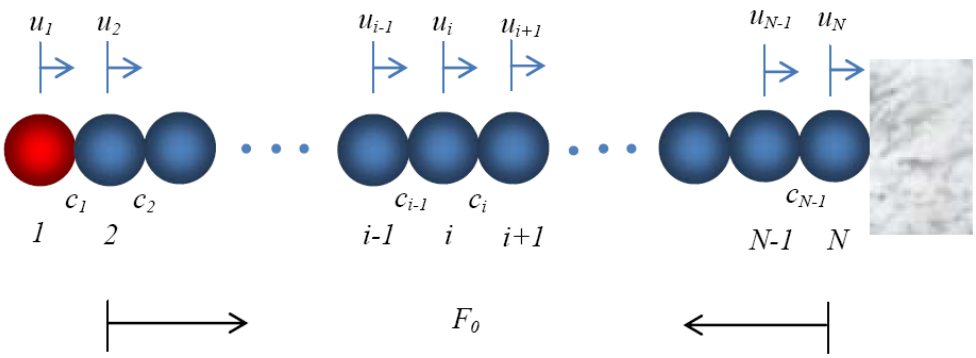

Figure 6.3 Schematic diagram of the one-dimensional discrete element model. The c_1, c_2,…, c_N indicates the points of contact between two neighboring particles. When the presence of the piezo rod is modeled, the spheres 13 and 18 are replaced by solid rods.

Here, the subscripts *c* and *w* refer to the point of contact between two neighboring particles and the point of contact between the last particle and the half-infinite wall, respectively. The values of *R*, *m*, and *u* are respectively the radius, mass, and axial displacement from the equilibrium position of the particle. *A* is the contact stiffness between adjacent beads (A_c) or between the last bead and the wall (A_w). γ is a coefficient that takes into account the dissipative effects associated with the contact of the chain with the inner tube's surface and the wall (Yang et al., 2011; Carretero-González et al. 2009). *F* is the sum of the body force, e.g., gravity, and external forces applied on the chain. The dot represents the time-derivative while the operator $[]_+$ returns the value of the variable if the variable is positive, otherwise it returns 0. Finally, *E* and ν are the Young's Modulus and the Poisson's ratio, respectively, of the beads (E_c, ν_c) and of the wall (E_w, ν_w).

The impact of the striker was simulated by setting the initial displacement $u_0=0$ and the initial velocity $\dot{u}_0 = \sqrt{2gh}$, where *g* is the gravitational constant and *h* is the experimental falling height (*h* = 7.2 mm). The other initial conditions were $u_i = 0$ for $i = 1, 2, \ldots, N$, $\dot{u}_1 = \dot{u}_0$ and $\dot{u}_i = 0$

for $i = 1, 2, \ldots, N$. The differential Equation (6.) was solved to calculate u and $\dot{u}$ for each particle by using the fourth order Runge-Kutta method.

The model of the chain with the instrumented beads did not consider the fact that they are slightly heavier than the other spheres. This is because it was demonstrated (Daraio et al. 2005; Job et al. 2005) that the effect of the mass difference on the wave propagation can be neglected in the model. As such, particles 13 and 18 had the same mass of all the other particles. Moreover, because the piezogauge-half sphere contact stiffness is much higher than the sphere-sphere contact stiffness, the sensor still could be considered as a rigid body.

In order to model the presence of the piezo rods, the modeled chain comprised two solid rods having the same geometric and material properties of the piezoelectric cylinders at position 13 and 18. And the mass and contact stiffness (terms A_i) at positions 13 and 18 were replaced accordingly. Finally, the model relative to the presence of the coil and the bias magnet, considered the tube filled with 29 particles. The presence of the magnetic bias was included by considering four particles per coils subjected to a static compressive force equal to 1.8 N. This value was estimated by comparing the experimental wave speed of the incident solitary wave to the analytical prediction provided by the long-wavelength limit (Nesterenko, 1983; Daraio et al. 2006b; Ni et al. 2011b). Irrespective of the sensing system considered the model included the static pre-compression due to the self-weight of the particles, and the dissipation coefficients γ, whose determination will be discussed in Section 5.1.

6.3.2 Numerical Results

The numerical model was applied to simulate the three setups described in Section 2. To predict the measurements of the three types of transducers, the numerical values of the force-time

profiles at contact points c_8, c_{11}, c_{12}, and c_{13} (see the notation in Figure 6.3) are presented in Figure 6.4. The figure shows the presence of a single solitary wave, whose amplitude and time of arrival are almost the same for all three types of sensors. The pulse measured by MsS at contact points c_{11}-c_{13} has a slightly earlier arrival due to the presence of the magnetically induced pre-compression. The presence of the cylinder alters the temporal force profile due to the following mechanism. As the single pulse propagates, the particle 11 compresses the next particle giving rise to the first peak visible in Figure 6.4(b). Because the piezo rod is heavier than particle 12, particle 12 bounces back. Thus, the corresponding amplitude of the dynamic force is higher and it is visible in Figure 6.4(c). By bouncing back, particle 12 gets closer to sphere 11 originating the small hump visible in Figure 6.4(b). This reflected wave propagates backward to the top of the chain and it appears also in Figure 6.4(a) at around 170 microseconds. Meantime, after particle 12 is compressed by particle 11 for the second time, its velocity becomes slightly larger than that of the cylinder. This compresses again particle 12 against the rod, as demonstrated by the small pulse in Figure 6.4(c) at 200 microseconds. This creates a state of compression between the cylinder and its neighboring particle 14, which gives rise to a secondary pulse that trails the incident wave and is visible in Figure 6.4(d) at 220 microseconds. The figure also indicates that the amplitude of the wave passing through the cylindrical sensor reduces significantly when compared to the same pulse monitored by the bead sensor or the MsS.

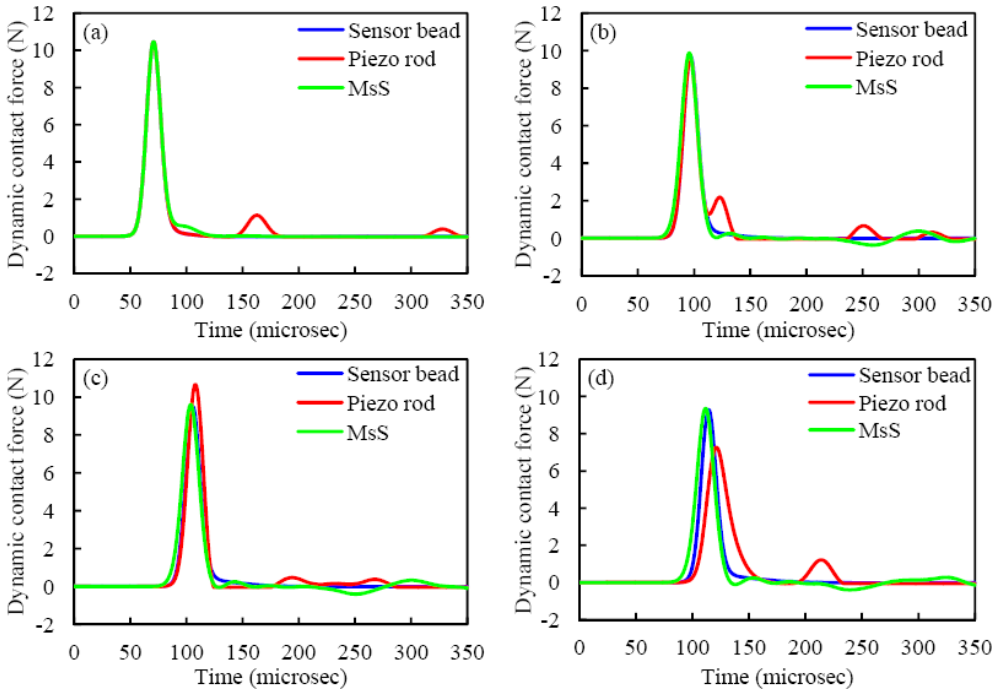

Figure 6.4 Discrete particle model results showing the temporal force profile for all three sensing configurations at contact points: (a) c_8, (b) c_{11}, (c) c_{12}, and (d) c_{13}.

The numerical results of the force profiles at position 13 for the three sensing systems are shown in Figure 6.5. Figure 6.5 (a) refers to the sensor bead. The dashed lines represent the dynamic forces at the contact points c_{12} and c_{13}, whereas the continuous line is the average value of the two dynamic contact forces and it represents the force measured by the sensor bead (Daraio et al. 2005). Figure 6.5(b) presents the results relative to the rod. Similar to Figure 6.5(a), Figure 6.5(b) shows the values of the force at the contact points of the cylinder with the particles 12 and 14 (dashed lines) and the averaged value (continuous line). Because the cylinder's mass and stiffness are different than those of the spheres, the incoming wave is partially reflected at the interface, thus reducing the amplitude of the transmitted pulse.

Finally, Figure 6.5(c) shows the results associated with the presence of the coil centered at location 13. Owing to the length of the coil and the position of the magnetic bias (Figure 6.2(d)) the dynamic forces at contact points c11 to c14 are presented. Because the force

measured by the MsS is the average of four dynamic contact forces at contact points 11 to 14, its amplitude is smaller and its duration is longer with respect to the dynamic force measured by the other two sensing systems.

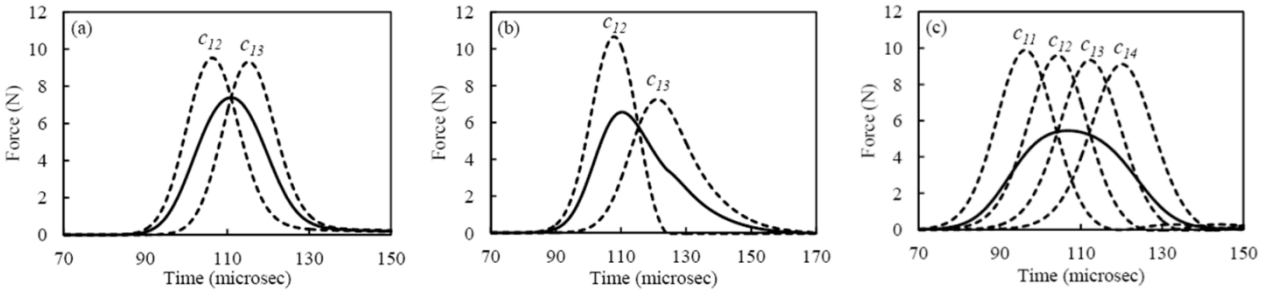

Figure 6.5 Discrete particle model results showing the temporal force profile at some contact points (dashed lines) and as measured by three sensors (solid lines): (a) bead sensor, (b) piezo rod, (c) magnetostrictive sensor.

6.4 EXPERIMENTAL RESULTS

Although the dissipation coefficients can be determined empirically by measuring the magnitudes of the dynamic forces at different positions in the chain (Yang, 2011; Carretero-González, 2009), we adopted another approach that is illustrated here. Figure 6.6 shows the voltage output measured by both spherical sensors. The first pulses represent the main solitary wave traveling from the impact point to the wall, while the second pulses are the waves reflected from the rigid wall. We characterized the HNSW by means of three parameters: the time-of-flight (TOF), the speed, and the amplitude ratio (AR). The first parameter denotes the difference in the transit time at a given position between the incident and the reflected wave. The speed can be simply computed by dividing the distance between two sensors over the difference in the arrival time of the two amplitude peaks. Finally, we define the AR as the ratio of the reflect wave amplitude over the incident pulse amplitude.

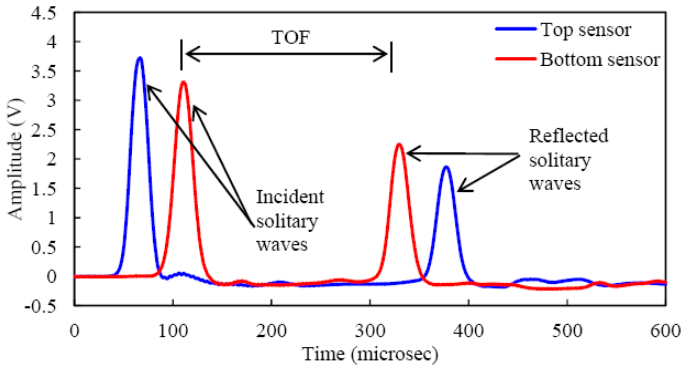

Figure 6.6 Typical waveforms measured by the bead sensors.

In order to calibrate the numerical model to our experimental setup, the dissipation was taken into account. Because the force amplitudes of both incident and reflected solitary pulses were proportional to the voltage-force conversion factor, their AR was independent upon this conversion factor. We computed the dissipation coefficient by considering the 500 experimental measurements of the amplitude ratios AR_{top} and AR_{bottom} measured by the sensors located at positions 13 and 18, respectively. For different combination of dissipation coefficients γ_c and γ_w, the numerically predicted $AR_{top\text{-}num}$ and $AR_{bottom\text{-}num}$ were calculated. Then an objective function y:

$$y(\gamma_c, \gamma_w) = norm\left(\left[\frac{AR_{top-num} - AR_{top}}{AR_{top}}, \frac{AR_{bottom-num} - AR_{bottom}}{AR_{bottom}}\right]\right) \tag{6.8}$$

was defined in terms of the difference between numerical and experimental results. We optimized this function by finding the combination of γ_c and γ_w that minimized the value of the objective function subjected to the following constraints: $\gamma_c \geq 0$ and $\gamma_w \geq 0$. The result of the optimization process yielded to $\gamma_{c=}$ 4.8 kg/s and $\gamma_{w=}$ 0. As it is not very plausible that there is no dissipation at the wall, the result of the optimization may suggest that the dissipation along the chain might be more dominant than the energy loss from the last particle-wall interaction.

As is said earlier, when the piezoelectric cylinders and MsSs were used, the sensor beads were replaced by the two piezo rods and two spheres, respectively. Because the coefficient γ_c accounts for the dissipation along the entire chain, we assumed that the replacement of two particles out of 29 had negligible effect on the value of γ_c. Thus, the value γ_c = 4.8 kg/s was applied to all three kinds of sensing technology.

In applications such as nondestructive testing, voltage measurements are sufficient to correlate the characteristics of the solitary pulses to the properties of the structure or material under inspection. However, other engineering applications may require the quantitative measurement of the dynamic force associated with the traveling pulse. Thus, the relationship between this force and the output voltage from the sensor needs to be known. To establish this relationship, we adopted the following procedure for all sensing configuration. The experimental time profiles, expressed in Volts and collected using the experimental setup described in Section 6.2 were compared to the force profiles (expressed in Newton) computed with the discrete particle model described in Section 6.4. The model considered the effect of dissipation.

Figure 6.7(a,c,e) shows the voltage output associated with the three transducers pair. One out of 500 measurements is displayed. With respect to Figure 6.7(a,c), Figure 6.7(e) shows negative values of the output voltage. When the solitary pulse travels through the particles surrounded by the MsS, there is an increase in compression due to the contribution of the dynamic contact force. This increase generates a positive gradient of the magnetic flux visible in the positive output voltage. When the pulse propagates away, the compression between adjacent spheres decreases, creating a negative gradient of the magnetic flux. This negative gradient is represented by the negative portion of the signal in Figure 6.7(e). Similarly, the dashed lines in Figure 6.7(b,d,f) shows the corresponding numerical predictions. Because the overall shapes of

the incident experimental and numerical temporal profiles were almost identical, a conversion factor K_i associated with each measurement i was calculated as:

$$K_i = \frac{F_{Num}}{V_{i,Exp}} \quad (i = 1,2,\ldots,500) \tag{6.9}$$

.

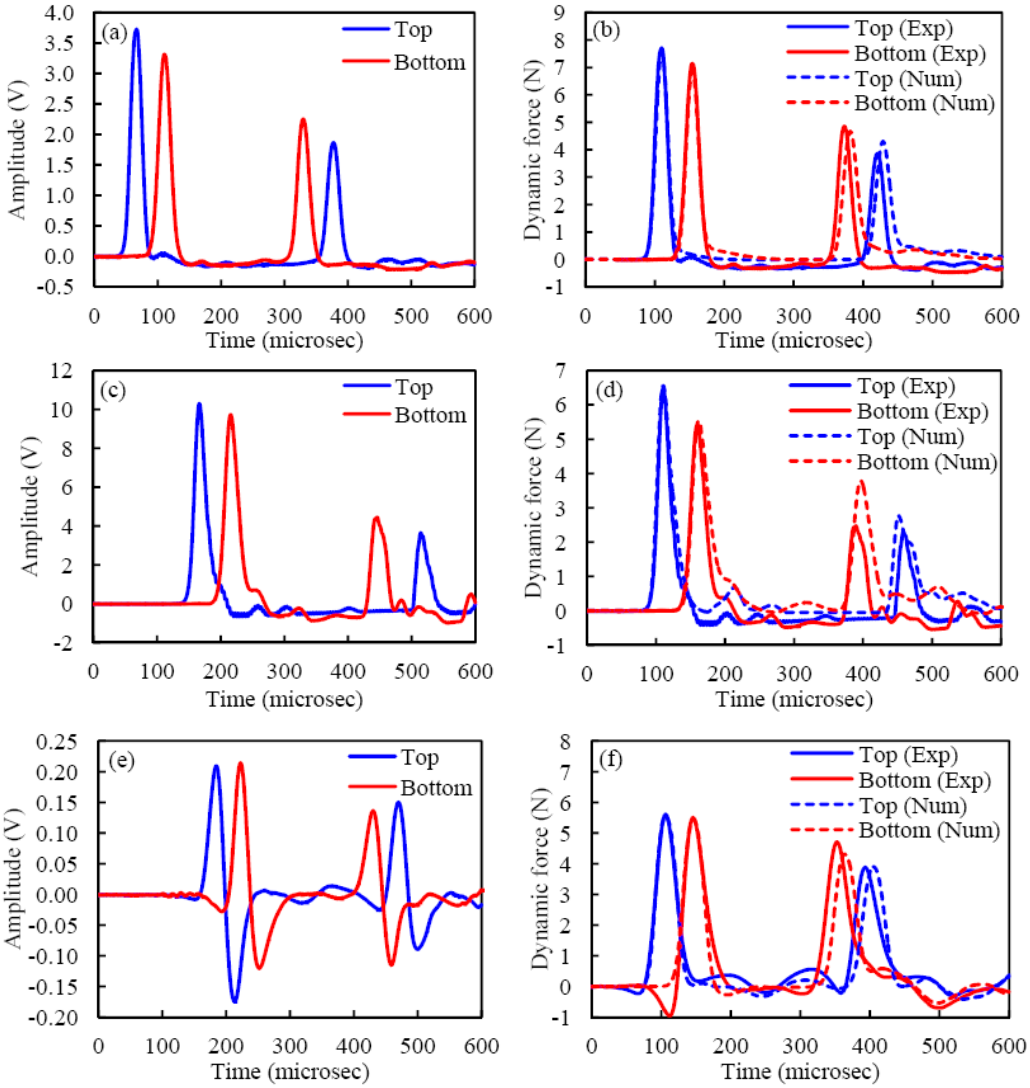

Figure 6.7 (a) Experimental results for bead sensors, (b) comparison of experimental and numerical results for bead sensors, (c) experimental results for cylindrical sensors, (d) comparison of experimental and numerical results for cylindrical sensors, (e) experimental results for magnetostrictive sensors, (f) comparison of experimental and numerical results for magnetostrictive sensors.

Here $V_{i,Exp}$ is the maximum experimental output voltage, and F_{Num} is the maximum amplitude of the dynamic force determined numerically. A unique conversion factor K was then established by averaging 500 ratios. Table 6-1 summarizes the coefficients determined for every transducer. The small standard deviations prove the repeatability of the setup and the consistency of the novel sensing systems. It is noted that, as the force measured by the MsS is related to the integral of the voltage (see Equation (6.3)), the corresponding units for factor K are different from the others.

Table 6.1 Calibration coefficients adopted in this study

	Calibration coefficient *K*	**Relative standard deviation (%)**	**Unit of *K***
Bead sensor top	2.072	4.71	N/V
Bead sensor bottom	2.160	4.31	N/V
Cylindrical sensor top	0.632	4.00	N/V
Cylindrical sensor bottom	0.557	4.01	N/V
MSS top	0.131	1.44	N/V·sec
MSS bottom	0.156	1.56	N/V·sec

6.5 COMPARISON OF THE NUMERICAL AND EXPERIMENTAL RESULTS

In the last part of our study, we quantitatively compared the shape of the experimental and numerical force profiles. Figure 6.7(b) shows the time series associated with the bead sensors. For convenience of representation, the experimental data are shifted horizontally in order to overlap the numerical and experimental peak of the incident pulse at the particle 13. Clearly, the plot shows good agreement between the experiment and the numerical model and a slight discrepancy is only visible for the reflected waves.

Similarly, Figure 6.7(d) refers to the results relative to the piezo rod. The figure shows that the amplitude of the incident pulse measured by the bottom cylindrical sensor is slightly smaller than the numerical prediction and the amplitudes of the reflected pulses are smaller than the corresponding numerical predictions. One possible reason is that the numerical model may underestimate the attenuation at the bead-cylinder interface, when the effect of possible static friction between the cylinder and the inner wall of the tube is ignored.

Finally, Figure 6.7(f) shows the experimental force profiles measured by the MsSs and the corresponding numerical result. By integrating the signal in Figure 6.7(e) and multiplying the integral with the calibration coefficient K listed in Table 6-1, Figure 6.7(f) is obtained. The presence of the magnetically induced precompresson reduces the attenuation and increases the pulse's velocity, thus reducing the TOF. The figure reveals the presence of a trough preceding the arrival of the main peak at both sensors. The origin of this response is not fully understood yet but we speculate that it might be associated with the presence of the permanent magnetic field. Nonetheless, the ability of the MsS to capture the presence and characteristics of HNSWs is evident. Overall Figure 6.7(b,d,f) shows very good agreement between the numerical and the experimental results relative to the incident pulse. There is some noticeable discrepancy in the time of arrival and amplitude of the reflected wave. This is likely due to the modeling of the rigid wall at the base of the chain.

To assess and compare the capability of the novel transducers to measure the characteristics of the HNSW propagating in a straight chain of particles, Table 6-2 and Table 6-3 are presented. Table 6-2 summarizes the numerical and experimental values of the TOF and AR associated with the propagating pulse. The experimental values represent the average and the standard deviation (std) of the 500 measurements. The small variation between numerical and

experimental values suggest that the two novel transducers perform equally well to the sensor bead. The small standard deviation also remarks the repeatability of the sensing systems. The speed of the incident and reflected solitary pulses are presented in Table 6-3. The small differences between numerical and experimental results indicate that all three types of sensors are able to measure the wave speed accurately. The smallest standard deviation, which was found for the magnetostrictive transducer, indicates the highest degree of repeatability of the setup. The speed of the solitary wave depends upon the setup.

Table 6.2 Experimental and numerical time-of-flight and amplitude ratio

Sensor Type	Sensor Position	Time of flight (microsec)				AR			
		Numerical	Experimental		Difference (%)	Numerical	Experimental		Difference (%)
			Mean	Std			Mean	Std	
Bead	Top	318.7	309.8	2.6	2.79	0.57	0.55	0.04	3.51
	Bottom	227.5	219.9	1.6	3.34	0.68	0.73	0.02	7.35
Cylindrical	Top	341.0	337.0	5.3	1.17	0.42	0.37	0.03	11.9
	Bottom	234.9	228.4	3.0	2.77	0.68	0.60	0.07	11.8
MSS	Top	298.8	287.3	0.9	3.85	0.70	0.69	0.02	1.43
	Bottom	217.6	207.0	0.7	4.87	0.79	0.86	0.01	8.86

Table 6.3 Experimental and numerical speed of the incident and reflected HNSW pulse

Sensor Type	Type of Wave	Numerical (m/s)	Experimental (m/s)		Difference (%)
			mean	std	
Bead	Incident	540.0	547.0	13.1	1.30
	Reflected	505.6	514.1	16.0	1.68
Cylindrical	Incident	486.3	512.0	14.6	5.28
	Reflected	458.7	422.9	38.6	7.80
MSS	Incident	596.8	602.1	1.75	0.89
	Reflected	576.6	584.8	3.36	1.42

This is not surprising as the the solitary waves exhibit unique physical properties when compared to linear elastic waves. One of these properties is the dependency of the speed to the pulse's amplitude and to the level of precompression in the chain. Thus, the wave speed

measured by the MsSs was the largest because they induce precompression magnetically. The speed measured by the piezo rods was the smallest as the presence of the solid rod diminishes the amplitude of the traveling pulse.

6.6 CONCLUSIONS

In this chapter we presented the results of numerical and experimental studies where three sensing systems for the measurements of highly nonlinear solitary pulses propagating in a chain of spherical particles. The transducers were a conventional pair of instrumented beads, and two novel designs based on the utilization of a pair of piezo rods, and a pair of coils. The latter aimed at exploiting the magnetostrictive properties of the particles.

We compared the experimental results to the numerical predictions obtained by means of a discrete particle model. We found that the two novel designs performed equally well when compared to the conventional sensor beads, which require micromachining and must not be allowed to rotate in order to keep their sensitivity constant. From this study the following consideration can be made. Owing to its geometry the piezoelectric cylinder is not prone to rotation and does not require the machining of half-particles. However it may originate unwanted secondary pulses that trails the incident wave and attenuates the amplitude of the incident pulse. To prevent this problem, the cylindrical sensor should have the same mass of the other particles composing the chain, and the sphere-cylinder contact stiffness should be the same as the sphere-sphere contact stiffness. Based on the contact mechanics theory, in order to have same contact stiffness, the elastic modulus of the cylinder should be approximately equal to 55% of the particle material's elastic modulus (Yang et al., 2011), which may not be feasible in practice for

piezoelectric material. Moreover the wiring of the cylinder may be too brittle and therefore prone to rupture. Conversely, the use of coils has multi-fold advantage: it can be mounted outside the chain; it is noncontact; is can slide at convenience at any position along the chain. However, this design can be used only when the particles composing the chain are sensitive to magnetostriction, *i.e.*, they are able to convert magnetic energy into mechanical energy and vice versa. In fact, the magnetostrictive sensors exploit the coupling between the dynamic deformation of the magnetostrictive material to which they are applied and the variation of magnetic field surrounding the material. As confirmed by the empirical results, the voltage output is proportional to the dynamic deformation caused by the passage of the solitary wave pulse (Equation (6.3).

7.0 LABORATORY TESTS

In this chapter we present the results of the experiments conducted to evaluate the feasibility of HNSWs to predict the occurrence of buckling in thermally loaded structures. This chapter is organized in two main sections. The first section reports on the experimental tests conducted at the Laboratory for Nondestructive Evaluation and Structural Health Monitoring studies, directed by Prof. Rizzo. Some of the results have been presented in Section 4.5. Then, we report on the experiments conducted at the University of Pittsburgh's Watkins-Haggart Structural Engineering Laboratory. The overarching objective of these tests was to investigate the hypothesis that one or more features associated with the propagation of HNSWs are able to predict the occurrence of incoming thermal buckling and/or estimate the rail neutral temperature.

In the next chapter we will report the results of tests conducted at the University of California San Diego, in collaboration with Prof. Francesco Lanza di Scalea.

7.1 TESTS AT THE LABORATORY FOR NDE AND SHM STUDIES

7.1.1 Effect of flexural stiffness and free-length: setup and results

To validate some of the findings obtained through the numerical modeling, we considered the effects related to material type and geometry on the characteristics of the solitary waves propagating along a chain in contact with the linear medium. In this series of tests, we examined: 1) the interaction between the HNSW transducer and beams made of two different materials, namely aluminum and stainless steel; 2) the interaction between the transducer and beams having different free-length. The results shown in Section 4.5 are part of a paper submitted recently (Cai et al. 2013b).

To test the effect of the flexural stiffness on the HNSWs reflections, we did the test with the same setup shown in Figure 4.13(a) but with different free length L=0.0127 × 1, 2, 3, 4, 5, 6, 7, 8 *m* (also 0.5, 1, 1.5, 2, 2.5, 3, 3.5, 4 *ft*) and we observed the response of the solitary waves propagating in the chain in contact with the beam. The experimental time waveforms are shown in Figure 7.1(a). For the sake of clarity, the values of the dynamic forces were offset. A close up-view of the IWs and PSWs is presented in Figure 7.1(b) while Figure 7.1(c) shows a close-up view of SSWs. As discussed in Section 4.3 the multiple pulses trailing the SSW are the effects of multiple impacts of the beam on the chain. Multiple SSWs are caused by multiple impacts between the chain and the beam. Figure 7.1(d) shows the increase of the time of arrival with respect to the L=0.0127 × 2 *m* case as a function the beam's span. The numerical data in Figure 7.1(e) are compared to the experimental data and the agreement is very good. Figure 7.1(f) shows the force ratio of PSW over IW at Sensor 1 and Sensor 2. There seems to be a little trend

but still too small compared to its variation to get any confirmative conclusion. No clear trend is found from the TOF curves for Sensor 1 at Figure 7.5(g) and Sensor 2 at Figure 7.1(h).

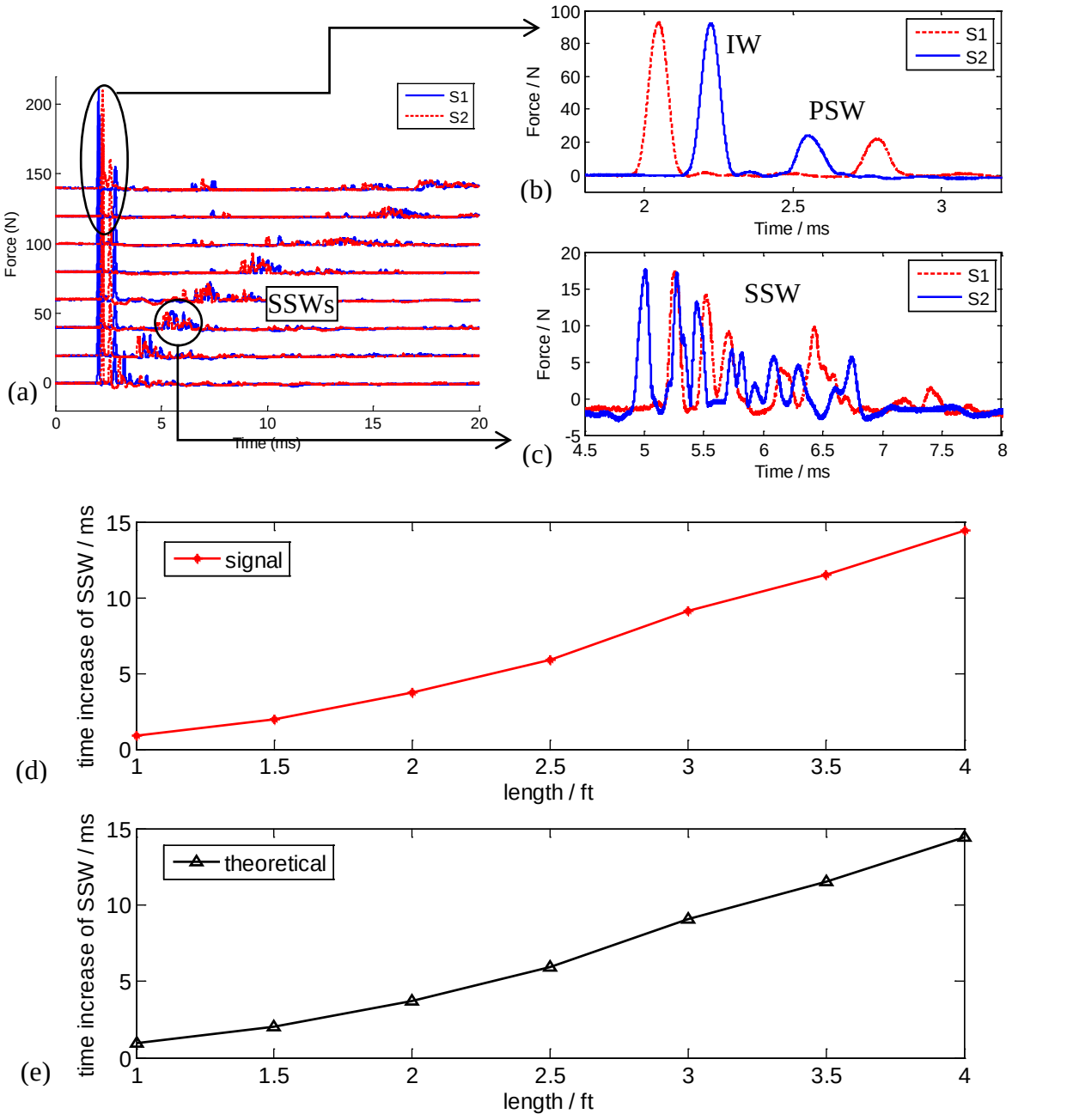

Figure 7.1 (a) typical waveforms with different clamped length L=0.0127 × 1, 2, 3, 4, 5, 6, 7, 8 *m* (b) zoom-in plot of IW and PSW (c) zoom-in plot of SSWs (d) mean value of time increase (difference) of each SSW (e) theoretical calculation of time increase of half cycle in the first natural vibration mode (f) force ratio of PSW over IW at Sensor 1 and Sensor 2 (mean value) (g) Time of flight between PSW and IW at Sensor 1 (h) TOF of flight between PSW and IW at Sensor 2

(f)

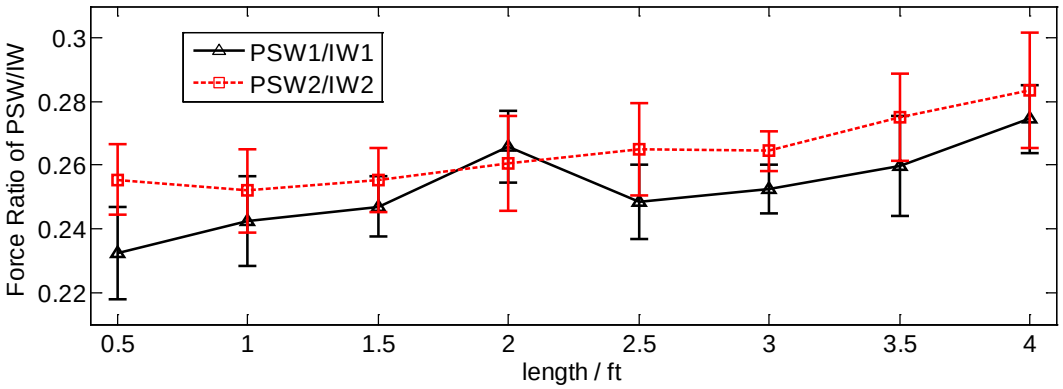

(h)

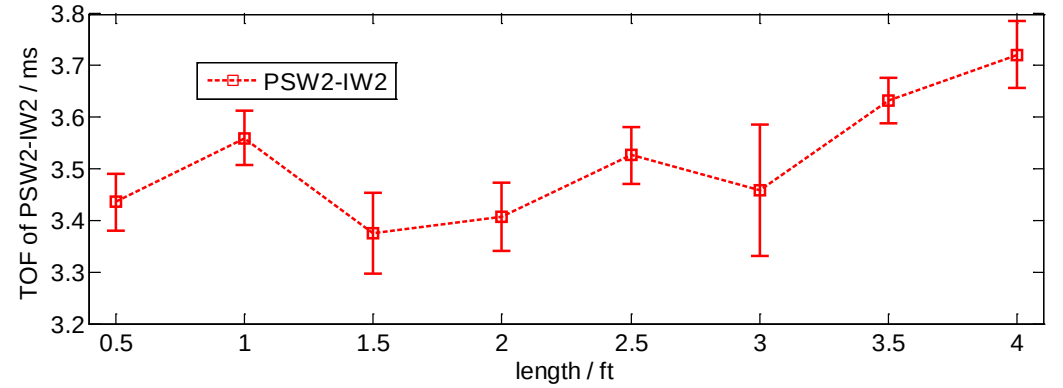

(g)

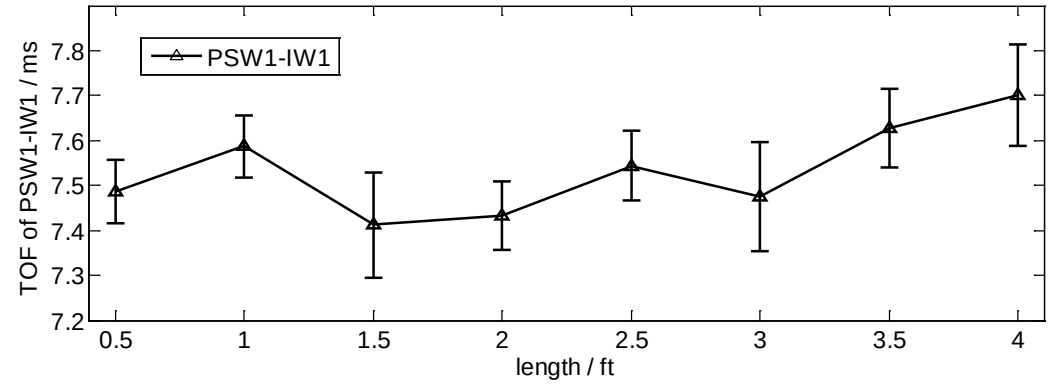

Figure 7.1 (continued).

7.1.2 Effect of thermal stress. Test 1

We applied thermal load to a steel beam. The results were presented in Section 4.5.

7.1.3 Effect of thermal stress. Test 2

The same steel beam was tested against a L-shaped HNSW transducer. The L-shape transducer was designed to better meet the need associated with the test of rails (see Chapter 8). Based upon the outcome of the research discussed in Chapter 5, we designed, built, and assembled the curved channel transducer shown in Figure 7.2.

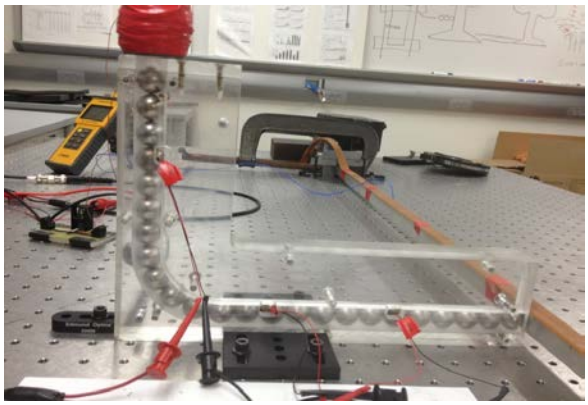

Figure 7.2 L-shape HNSW transducer in contact with a steel beam subjected to thermal load

The transducer was made of cast acrylic (McMaster-CARR product number 8560K363), it was 12” long, 8.43” tall and 0.5” thick. The radius of curvature at the center line was 2.25” and able to hold 5 beads in curved segment. The transducer hosted twenty-four 19.05 mm spherical particles. The test was repeated twice and the results are presented in Figure 7.3, which shows the values of the time of flight of SSW as a function of the temperature increase as measured by the two sensor beads embedded in the transducer. The experimental values are overlapped to the results of the numerical simulation and the agreement is very good.

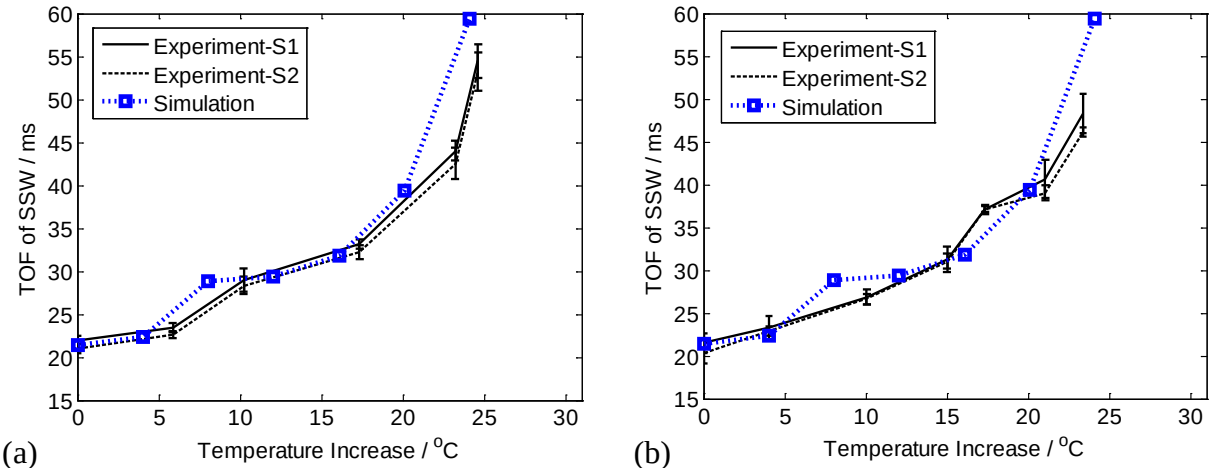

Figure 7.3 Comparison between experimental results and simulation results about TOF of SSWs using new transducer with curved frame. (a),(b) represent results in two tests with the same setup

The other wave features in the first experiment of the two including the force ratios of PSW/IW, SSW/IW and TOF of PSW/IW at Sensor 1 and Sensor 2 are plotted in Figure 7.4. Although the numerical model, predict some variation associated with the temperature raise, the experimental results do not provide a clear trend and firm conclusions on the effect of thermal load on the primary reflected waves cannot be drawn.

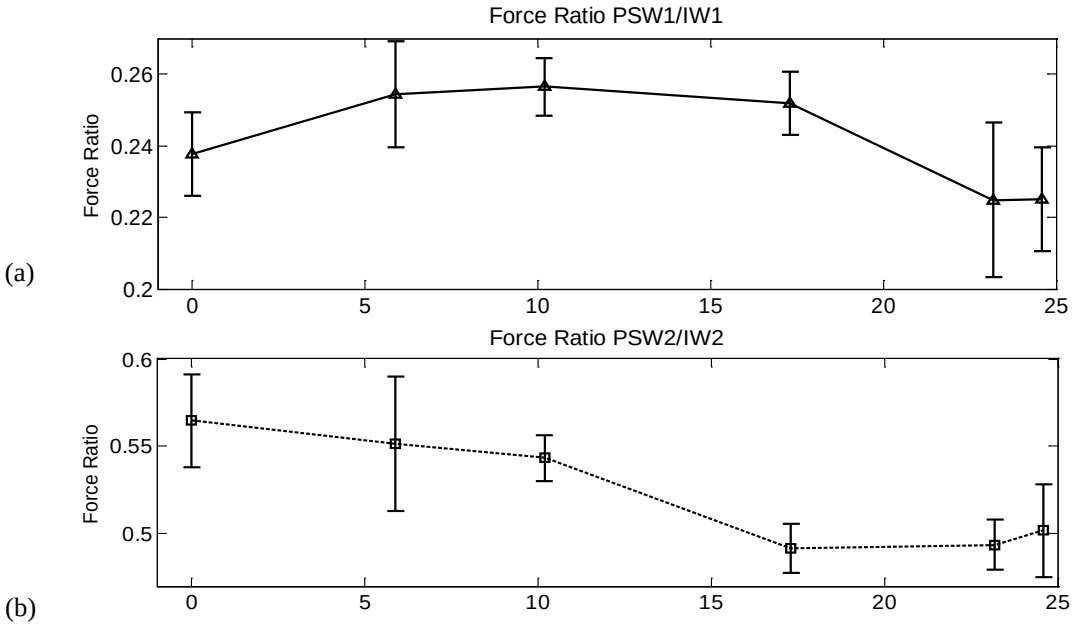

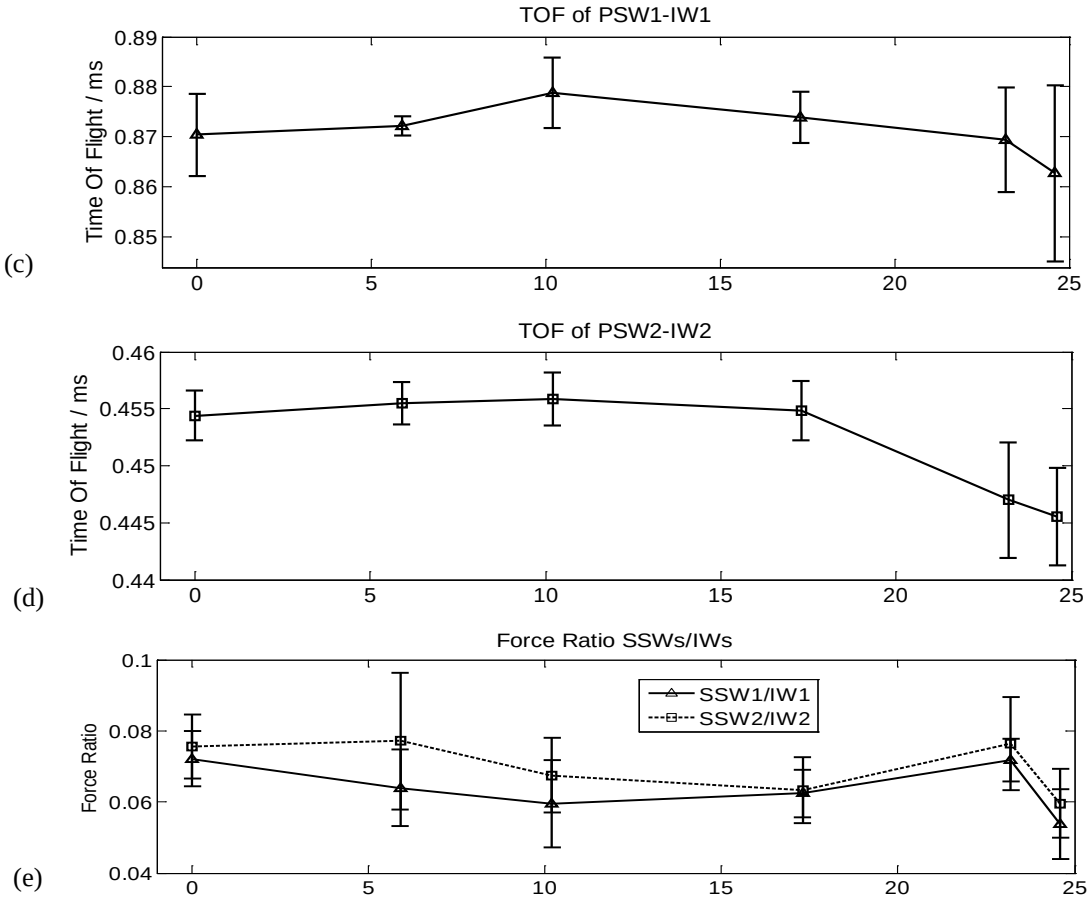

Figure 7.4 Effect of the temperature increase on: (a) Force Ratio of PSW1/IW1; (b) Force Ratio of PSW2/IW2 (c) TOF of PSW1-IW1; (d) TOF of PSW2-IW2; (e) Force Ratio of SSWs/IWs.

7.2 TESTS AT THE WATKINS-HAGGART LABORATORY

We conducted different experiments using the setup presented in Figure 7.5, where a beam was mounted on an 600 DX Instron© loading machine and it is subjected to thermal load by means of the same thermal tape used in the experiments described in sections 7.1 and section 7.2. A thermocouple was used to measure the temperature and two strain-gages were bonded to the test specimen. Finally a L-shape transducer was used for the generation and detection of HNSWs. Three sensors beads were embedded in the transducer. The first sensor, S1, was used as a trigger

and was located in the vertical segment. Two sensors, namely S2 and S3, were instead located in the horizontal segment and they were used to analyze the data, and to evaluate the effect of thermal loading.

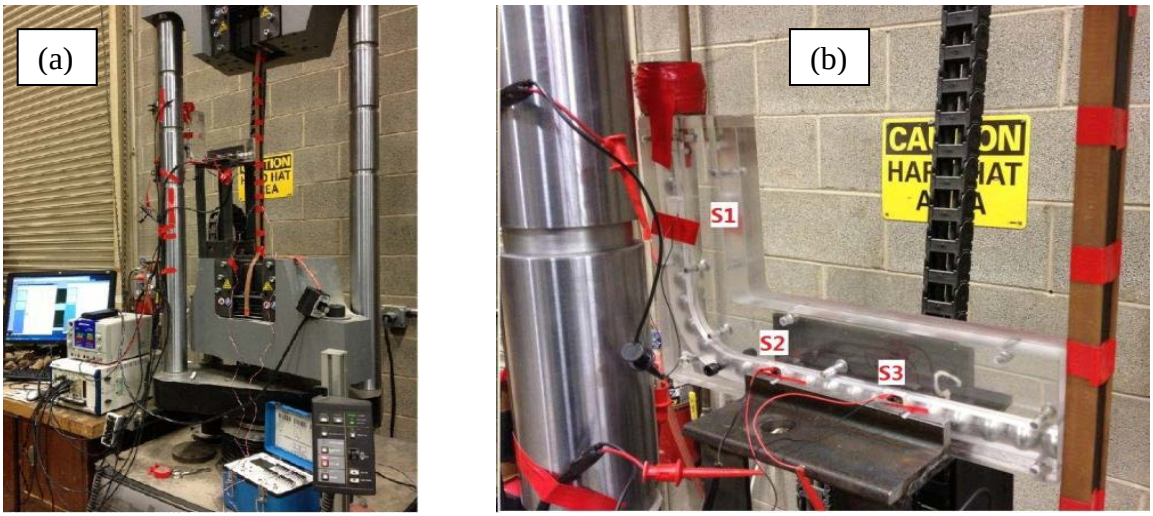

Figure 7.5 Tests at the Watkins-Haggart Structural Engineering Laboratories. (a) Photo of the whole setup; (b) close-up of the L-shape transducer in contact with a beam subjected to thermal loading.

7.2.1 Test 1

A stainless steel beam (type 304, 3/8'' thick, 3/4'' Wide, 6' long, McMaster CARR product number 8992K68) was clamped with free length L=30 *in* to the Instron© machine. The beam was loaded in tension and then held in tension while the heat tape applied thermal load. Due to the presence of the heat tape the state of stress in the beam changed from tension to compression. Three tests were conducted and the test protocols are summarized in Table 7.1. For each experiment 3 heating–cooling cycles were performed. The main difference on the protocol among the three test is the pre-tension load and then the thermal load necessary to the achieve

16% of buckling load. It should be noted that, owing to physical constraints associated with the Instron machine, it was not possible to achieve larger compression force.

The data from the sensor beads were recorded at discrete temperature intervals. For each interval, ten measurements were taken in order to evaluate the repeatability of the setup. The same sensor beads described in previous sections were used.

Table 7.1 Test protocol of each test

	Tension /kN	Percentage of yielding (F_y=37.5)	Compression /kN	Temperature /°C	Percentage of buckling (F_{cr} = -18.6 kN)	Cycles
Test 1	8	21%	-3.0	$t_{ambient}$*+31°C	16%	3
Test 2	15	40%	-3.0	$t_{ambient}$+50°C	16%	3
Test 3	20	53%	-3.0	$t_{ambient}$+64°C	16%	3

*$T_{ambient}$ =21°C is the ambient temperature.

A typical waveform recorded during the experiment is shown in Figure 7.6 as recorded by Sensor 2 and Sensor 3. As noted in previous experiments, the SSWs appeared as a cluster of pulses. We considered the amplitude and the time of arrival of the first peak of the cluster. The applied load on the machine was recorded by means of the Instron's software.

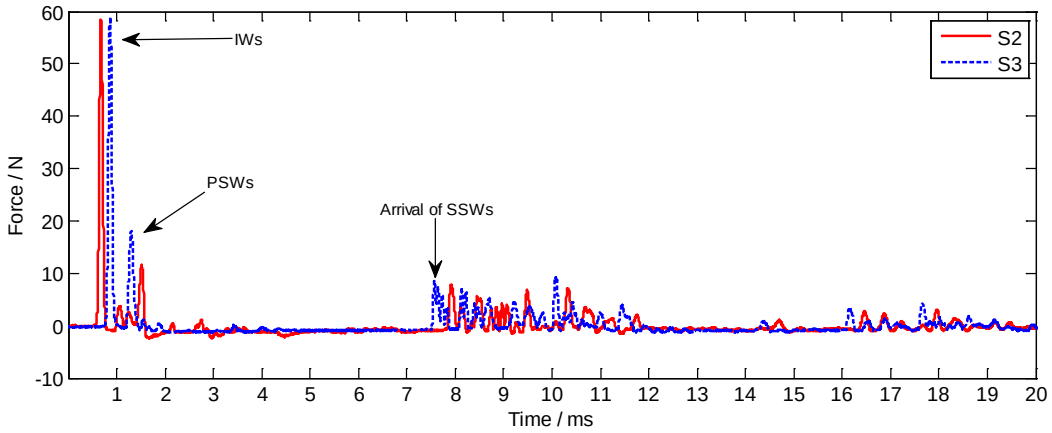

Figure 7.6. Tests at the Watkins-Haggart Structural Engineering Laboratories. Typical force profile measured by sensor beads S1 and S2.

Figures 7.7(a-f) show the difference in the time of arrival between secondary solitary wave and the incident wave as measured by both sensor beads and for Tests 1, 2, and 3. The values are plotted as a function of the thermal load, as measured by the strain gage. The panels of Figure 7.7 present the average value and the corresponding standard deviation. It should be noted that in this section **the positive load refers to tension**.

(a)

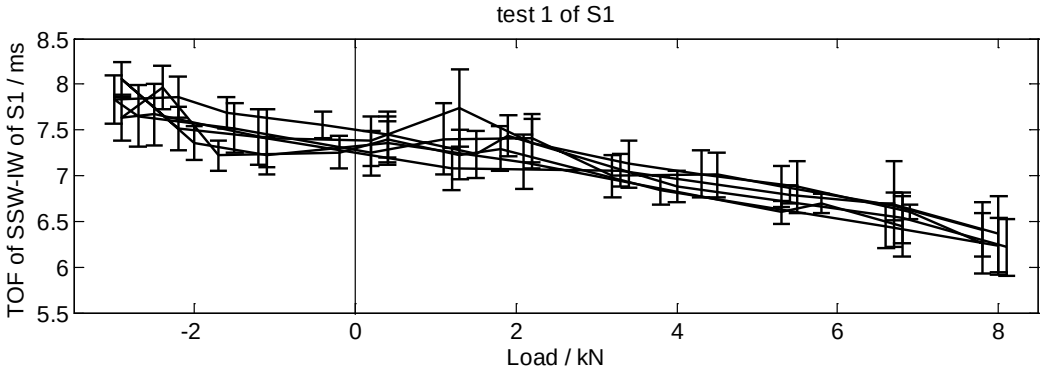

(b)

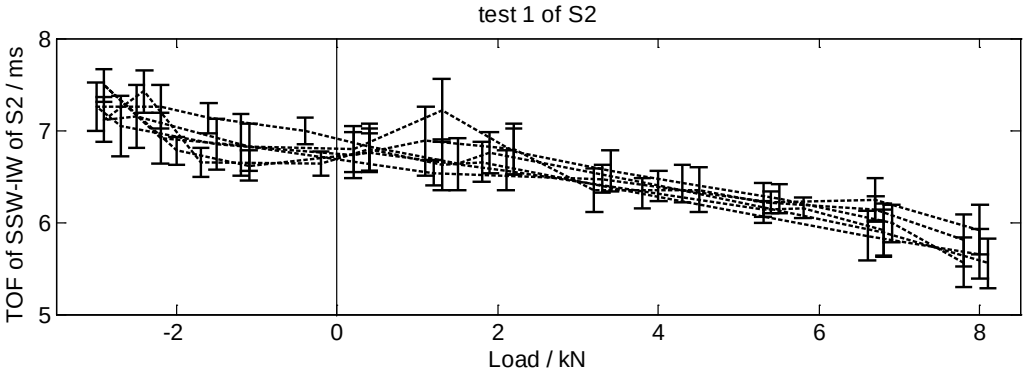

(c)

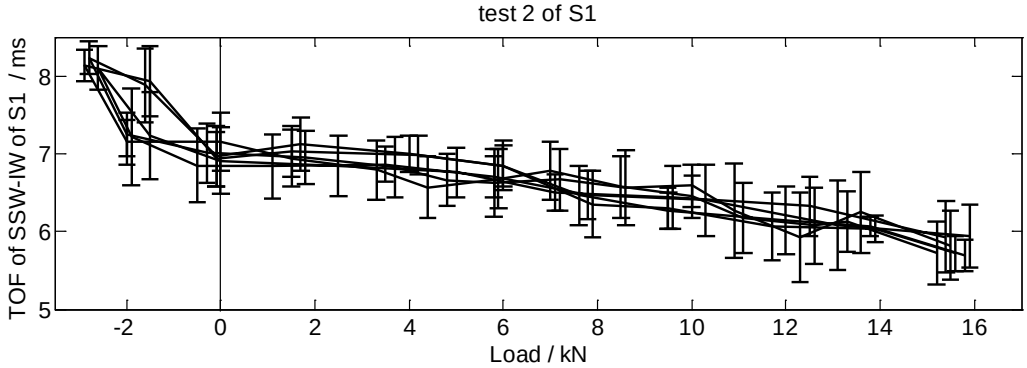

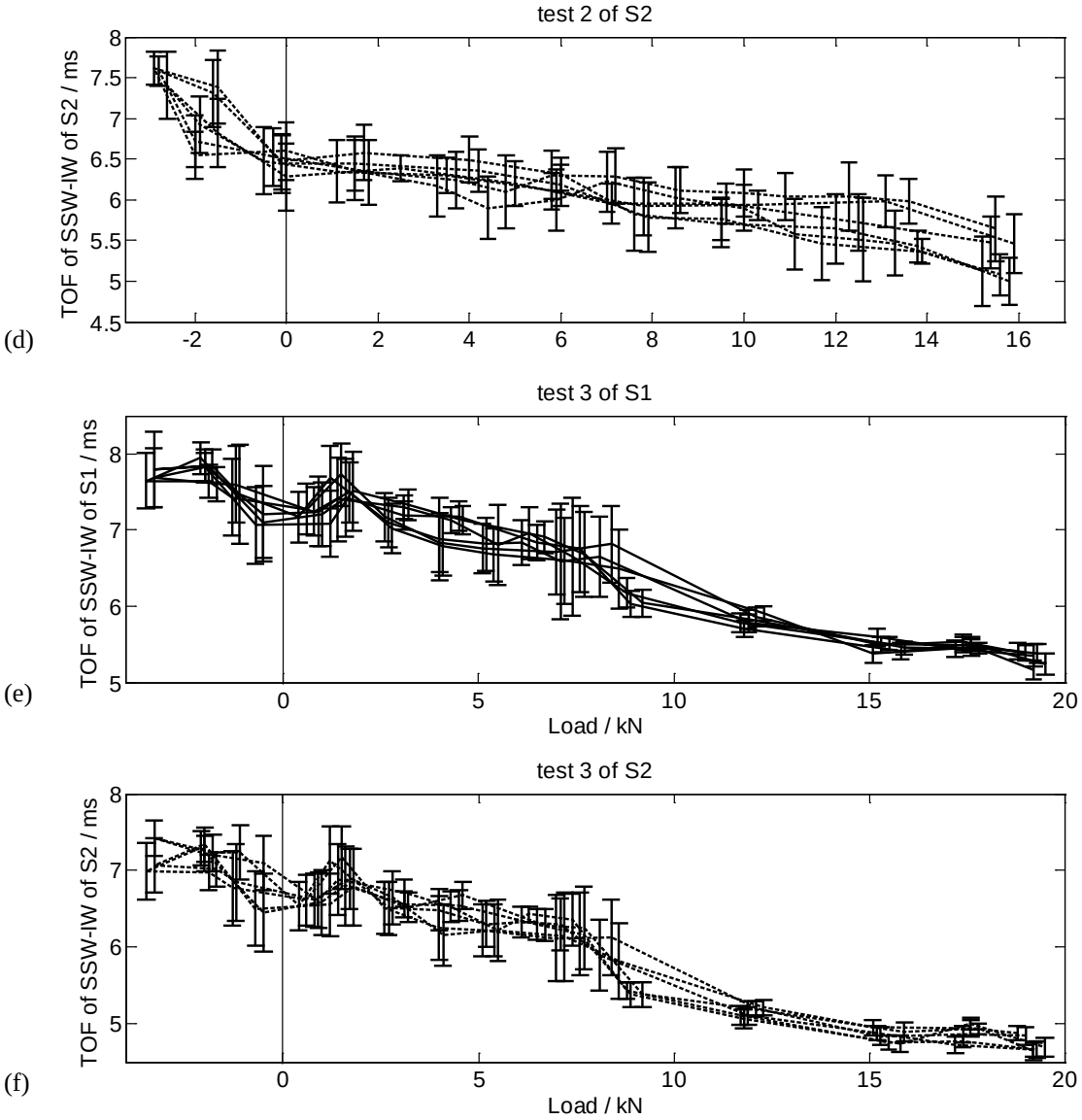

Figure 7.7 (a) TOF of SSW-IW at sensor 1 in test 1; (b) TOF of SSW-IW at sensor 2 in test 2; (c) TOF of SSW-IW at sensor 1 in test 2; (d) TOF of SSW-IW at sensor 1 in test 2; (e) TOF of SSW-IW at sensor 1 in test 3; (f) TOF of SSW-IW at sensor 1 in test 3; (g) linear interpolation of the three tests

To assess the repeatability of the experiment and the results from both sensors, Figure 7.8 compares the linear fitting associated with the experiments. The linear interpolation equations are calculated using least square method to minimize the squared residuals between the experimental values and fitting values. The linear interpolation is written as the form of $p(x) = p_1 x + p_2$. The coefficients p_1 and p_2 are summarized in Table 7.2.

Figure 7.8 shows that the TOF associated with the SSW is inversely proportional to the sign of the applied load. Thus, it decreases is the tensile load increase, and it increase when the compressive load increases. Compared with compression tests done in Figure 7.8 (TOF of SSW: 21~+∞ ms), TOF of SSWs have not so much space to vary in tension tests here (0~7 ms). That meant TOF of SSWs was not so sensitive to tension than compression.

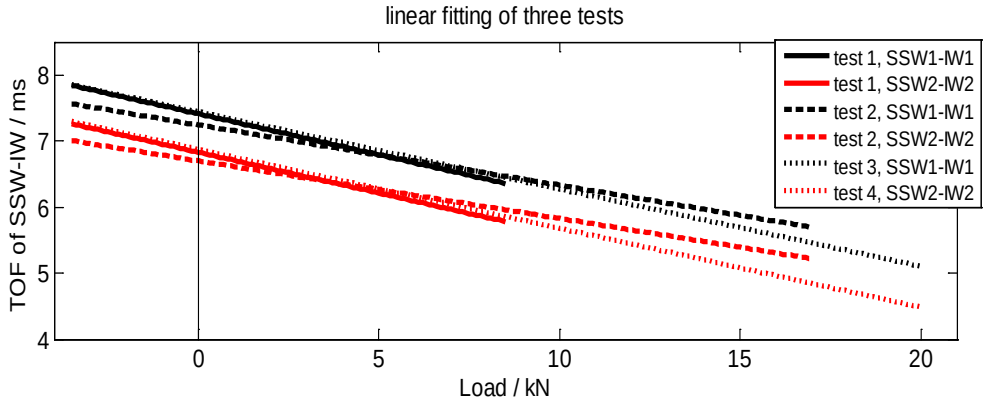

Figure 7.8 Linear interpolation of experimental data associated with a beam subjected to thermal stress. Time of flight of the secondary solitary wave as a function of the thermal load.

Since TOF of SSWs change from a value (21 *ms* in that condition) in zero stress to finite at buckling, there is a lot of space for TOF of SSWs to change. That means TOF of SSWs becomes more and more sensitive to the compression when get closer to buckling. However, for the case in tension, TOF of SSWs can only change from a value (8 *ms* in the test with loading machine) to zero. That means TOF of SSWs is not so sensitive to the loading.

Table 7.2 Coefficients of the linear interpolation of the experimental data.

	S1 of test 1	**S2 of test 1**	**S1 of test 2**	**S2 of test 2**	**S1 of test3**	**S2 of test 3**
P_1	-0.1237	-0.1234	-0.0912	-0.087	-0.1168	-0.1195
p_2	7.4099	6.8282	7.2436	6.6982	7.4414	6.8744

8.0 TEST ON RAILS

We tested the proposed technology at the Powell Laboratory at the University of California, San Diego. This is a large-scale test facility designed to study novel NDE methodologies to detect RNT in rails. Two photos of the test facilities are presented in Figure 8.1.

Figure 8.1 Test facility at UCSD

8.1 SETUP

The technology presented in this report was tested in two pre-tensioned rails composed of 70 *ft*-long tracks. The two tracks were an AREMA 141 section, hereafter indicated as the east rail (No. 1), and an AREMA 136 hereafter indicated as the west rail (No. 2). The rails are heated by means of a controlled heating system consisting of a rail switch heating wire attached to one side of the rail web.

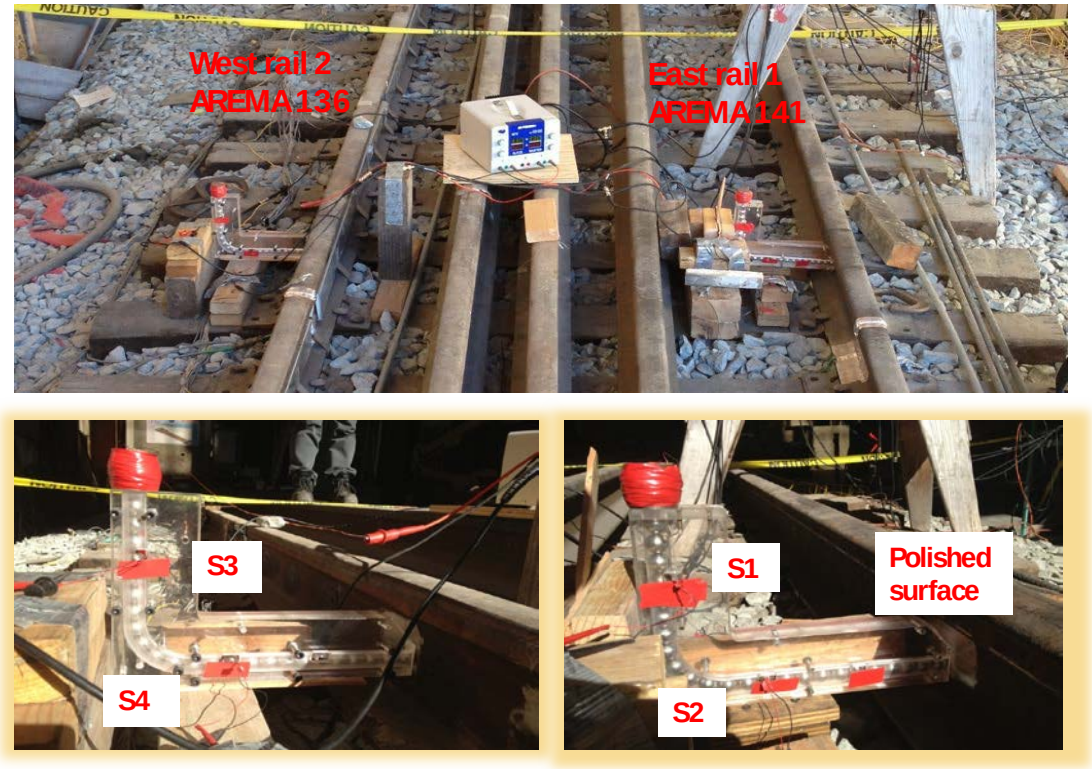

Figure 8.2 Close up view of the L-shaped transducer hosting the nonlinear medium to support the propagation of nonlinear solitary waves. The figure on top shows the power supply used to drive the electromagnet that enables the automatic action of the striker.

Two L-shaped HNSW transducers were used. The transducers were located such that one end of each chain was in contact with the rail web and located at the middle between two consecutive ties. The transducers contained 24 spherical particles, 19.05 mm in diameter, made

of stainless steel. At each transducer, the stroke of the striker was automatically driven by the action of an electromagnet remotely connected to a PXI unit that was also used to store the signals for post-processing analysis. The same PXI was used to control all the operations necessary to conduct the experiments. Each L-shape transducer contained two sensor beads, one located in the vertical segment and one located along the horizontal segment. Figure 8.2 shows a few photos of the experimental setup. Arrangements were made to prevent any accidental movement of the transducer, i.e. to prevent any unwanted detachment of the chain from the rail web. On the top panel of Figure 8.2, the power supply used to drive the current to the electromagnetic is clearly visible.

Five heating-cooling cycles were monitored over a three days period and the experimental protocol is summarized in Table 8.1. Two sampling rates were considered, 1 MHz and 5 MHz. For the first two heating ramps, we took one measurement every 5 seconds, and then we took 10 measurements every ten minutes. During the first two cooling ramps we took 15 measurements every 3℃. These measurements were taken manually, i.e. controlling the NI-PXI manually. Finally the last three cooling cycles were automatically monitored by taking ten measurements every two minutes.

Table 8.1 Experimental protocol of each test

Experimental Protocol		
Cycle 1	Heating	1MHz, 50msec, 1 measurement / 5 sec. continuously
	Cooling	1MHz, 50msec, 15 measurements /3℃ manually
Cycle 2	Heating	1MHz, 50msec, 1 measurement / 5 sec. continuously
	Cooling	1MHz, 50msec, 15 measurements /3℃ manually
Cycle 3	Heating	5MHz, 20msec, 10 measurements /2 min. automatically
	Cooling	5MHz, 20msec, 10 measurements /3 min. (auto)
Cycle 4	Heating	5MHz, 20msec, 10 measurements /2 min. (auto)
	Cooling	5MHz, 20msec, 10 measurements /3 min. (auto)
Cycle 5	Heating	5MHz, 20msec, 10 measurements / 2 min. (auto)
	Cooling	5MHz, 20msec, 10 measurements /3 min. (auto)

8.2 RESULTS

The force and the temperature data recorded by the data acquisition system embedded to the rail system are plotted as a function of time in Figure 8.3. For the sake of simplicity in the representation of the results, the three days of tests were merged. As it can be seen in Figure 8.3, two complete heating-cooling cycles were completed at each of the first two days of test. The third day one cycle was executed. The discontinuity visible at the border between two consecutive days was due to the further cooling that the rails experienced overnight. This means that at the beginning of testing on day 2 and day 3, the state of tension in the rail was higher than at the end of day 1 and day 2. For all cycles, the heating ramp usually lasted about 90 minutes to go from room temperature (~15 °C) to 60 °C. The cooling ramp lasted about 300 minutes.

Finally, it must be emphasized that in what follows, negative values of load refers to a state of compression.

Table 8.2 Rail Neutral Temperature during the heating/cooling cycles

	Cycle 1		**Cycle 2**		**Cycle 3**		**Cycle 4**		**Cycle 5**	
	heating	**cooling**	**heating**	**cooling**	**heating**	**cooling**	**heating**	**cooling**	**heating**	**cooling**
Rail 1	36.4	40.2	37.4	40.5	35.5	45.4	39.4	40.8	37.3	46.7
Rail 2	42.6	48.7	42.8	49.3	45.2	55.13	44.0	49.3	46.7	55.9

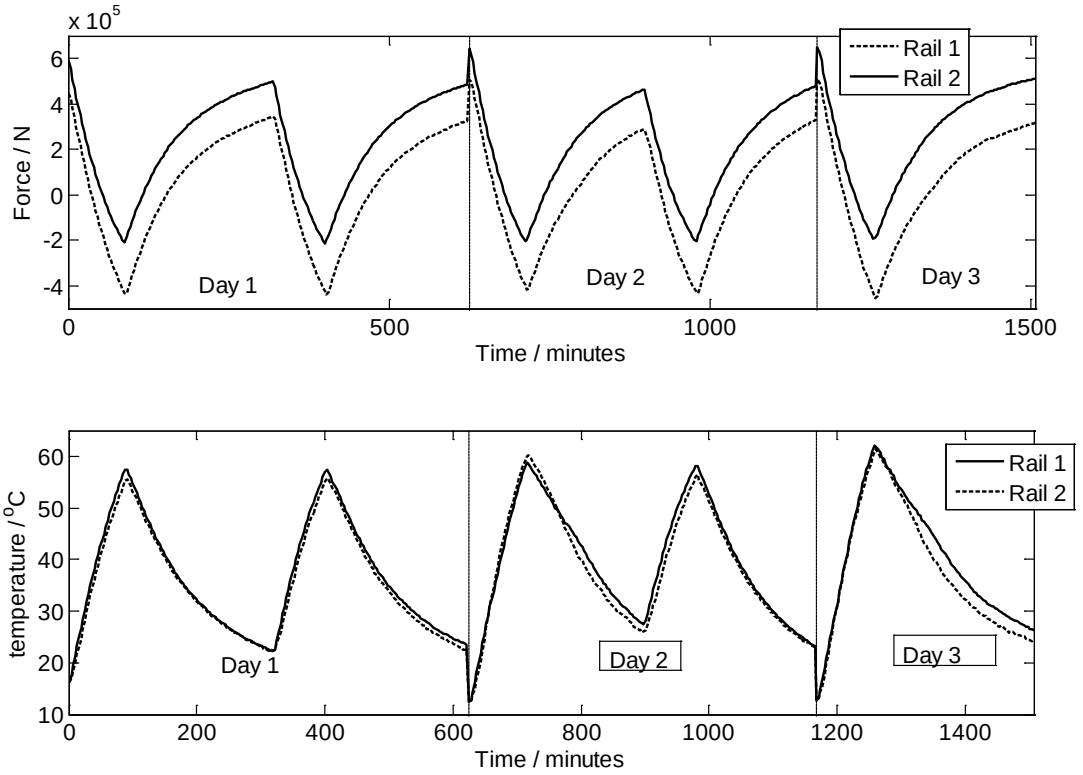

Figure 8.3 (a) Temperature (°C) as a function of testing; (b) Force (lb) as a function of the testing time

The same manual data were compared to the RNT computed by the data acquisition system embedded with the rails at UC San Diego. The manual data are overlapped to the automatic measurements in Figure 8.4 for both the east and the west rail. It is evident from the figure, that the RNT was different for the two rails and even for the same rail was not constant over the three days period. No firm conclusions can be given regarding such unexpected variability of the RNT. By overlapping the different values we can assume that the RNT for the AREMA 141 (rail 1, east rail) was 36.4 °C while the RNT for the AREMA 136 (rail 2, west rail) was 42.6 °C.

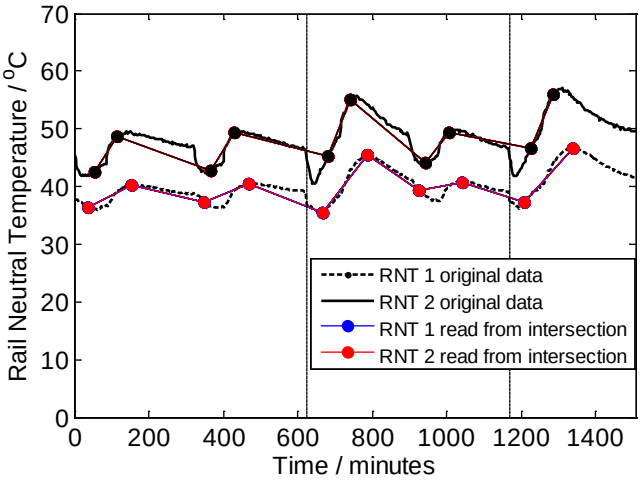

Figure 8.4 Rail neutral temperature as a function of the experiment test time. The vertical dashed lines separate the day test.

A typical waveform recorded during the experiments is shown in Figure 8.5. It refers to the sensors S1 and S2, which were embedded in the transducer in contact with the AREMA 141. The two pulses indicated as IW are the incident waves measured by Sensor 1 and Sensor 2. PSW2 represent the leading pulse associate with the reflection from the rail. Two important observations can be made. First, the secondary solitary wave is not formed. This is likely due to the stiffness of the rail with respect to the mass of the spherical particles. This is similar to the case examined numerically where a chain made of 5 mm particles in contact with a beam did not give rise to secondary reflected waves. The second observation is that many solitary pulses were generated. This is due to a combination of factors: the curved shape of the transducer and the bulkiness of the rail. The curvature of the transducer induces reflections and split of the main energy carrier at the curved segment. This is accentuated by the presence of the rail that induces a larger bouncing effect of the last particle of the chain at the interface.

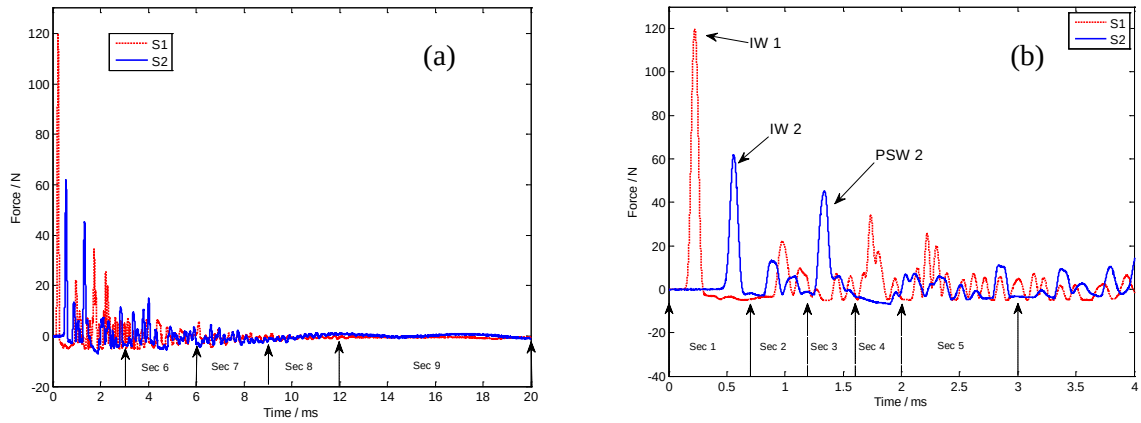

Figure 8.5 (a) a typical waveform (b) waveform after zoom in of 0~4 *ms*

In what follows the force amplitude, force ratio and the time of flight associated with the propagation of the main reflected wave is considered. Figure 8.6 shows the amplitude of the solitary wave peak as a function of the test time. The vertical continuous lines separate the heating from the cooling ramp and vice versa. The figure clusters the values measured associated with the incident waves (IWs) and the primary reflected waves (PSWs) from the AREMA 141 (sensors S1 and S2) and the AREMA 136 (sensors S3 and S4). The figure shows that the two L-shape transducers provided very similar quantitative values in terms of the incident wave which is dependent upon to the speed of the striker and the manufacturing of the vertical segment. As for the incident wave measured by the sensor beads along the horizontal segment, the difference in the amplitude between sensor S2 and sensor S4 is more evident. In this case, the difference is attributed to the design and manufacturing of the curved section.

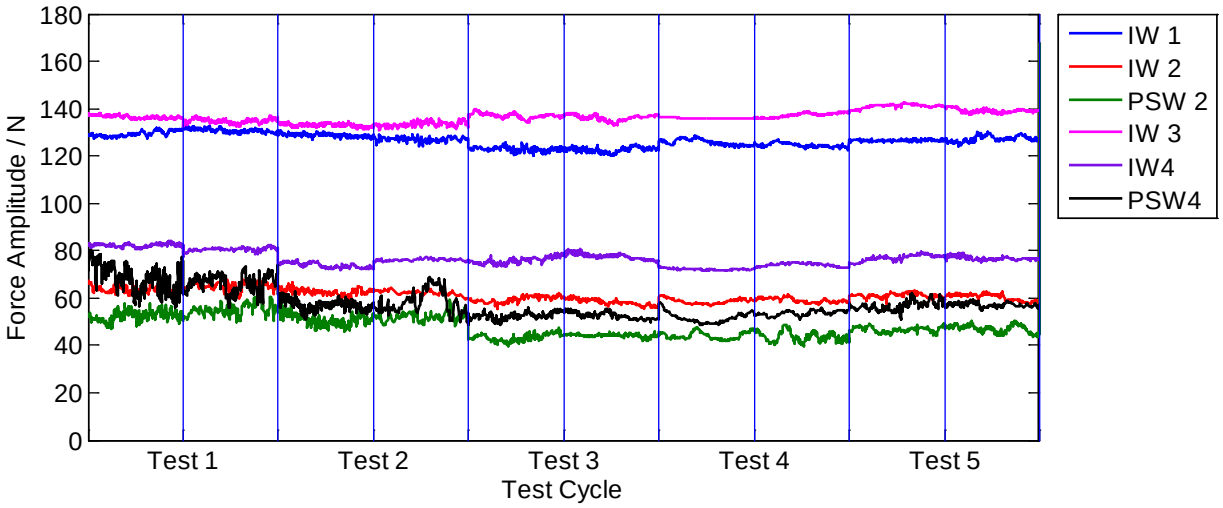

Figure 8.6 Force amplitude of the incident and the primary reflected waves

In order to quantify the effect of the buckling load, and normalize any influence of the striker speed, the ratios of the force amplitudes are presented in Figure 8.7 for both rails and both sensors. In particular we present the ratio between the incident waves (IW2/IW1 and IW4/IW3), and the ratio between the reflected and the incident wave at the sensor bead located in the horizontal segment of the transducer, i.e. PSW2/IW2 and PSW4/IW4. Overall we can say that the amount of energy lost at the reflection is smaller that the amount of energy lost by the solitary pulse when it travels along the curved segment. In fact, 15% to 30% loss is visible for the ratios PSW2/IW2 and PSW4/IW4; the incident wave lost 40% of its energy as it travels along the curved section of the L-shaped transducer mounted on the AREMA 136. The incident wave lost 50% of its energy as it travels along the curved section of the L-shaped transducer mounted on the AREMA 141. The latter two data are believed to be dependent mainly on the design of the transducer and its placement on the field.

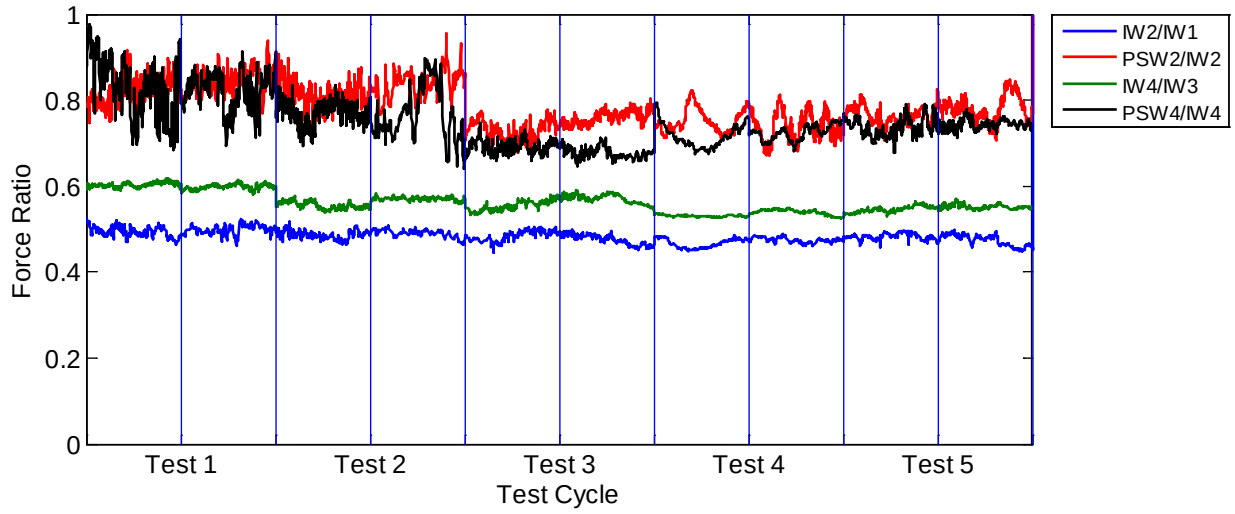

Figure 8.7 Force ratio as a function of time

Figure 8.8 present similar data relative to the difference in the time of arrival. The data relative to the incident waves for both waves are basically identical, with the exception of a few outliers visible towards the end of the cooling ramp during the first cycle. Most notably, we observed a difference in the data relative to the reflected waves from both transducers. This may be attributed to the different local conditions of stiffness associated with the two rails. Overall both Figures 8.7 and 8.8 do not show evident trends that link the HNSWs to the applied stress.

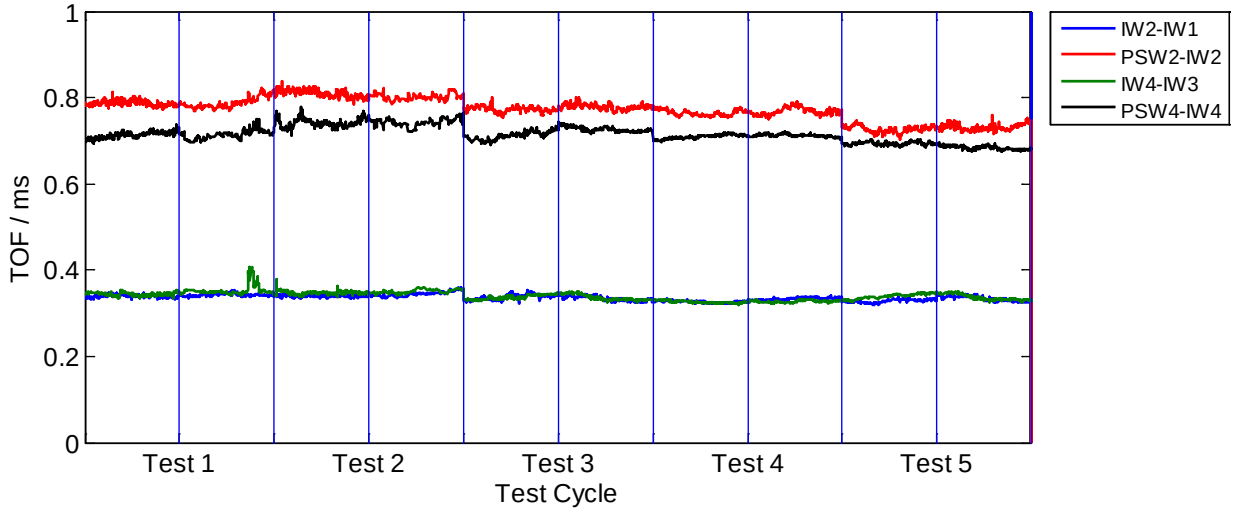

Figure 8.8 Time of flight (TOF) as a function of the heating-cooling cycles

As the simplified numerical model presented in Ch. 4 predicted small variations of the solitary wave features, we report in what follows some of the solitary wave features superimposed to the measured force. Figure 8.9 shows the average value and the standard deviation associated with the following parameters: amplitude ratio IW2/IW1; amplitude ratio PSW2/IW2; amplitude ratio IW4/IW3; amplitude ratio PSW4/IW4. The first and the third panel, which refer to the incident waves, show some fluctuations that should not be related to the rail conditions. The values displayed in the second and fourth panel are not showing any particular trend and no conclusion can be drawn with the exception of few heating ramps where the results associated with the solitary wave features seem to follow the loading ramp (see circled area).

Similarly to Figure 8.9, Figure 8.10 shows the results associated with the time of flight. As for the data relative to the force amplitude, the time of arrival of the solitary pulse seems not to be related to the level of stress on the rail.

To portray a comparison between the characteristics of the solitary wave considered in this chapter and the variability of the RNT, Figures 8.9 and 8.10 were plotted by replacing the values relative to the force with the rail neutral temperature measured manually.

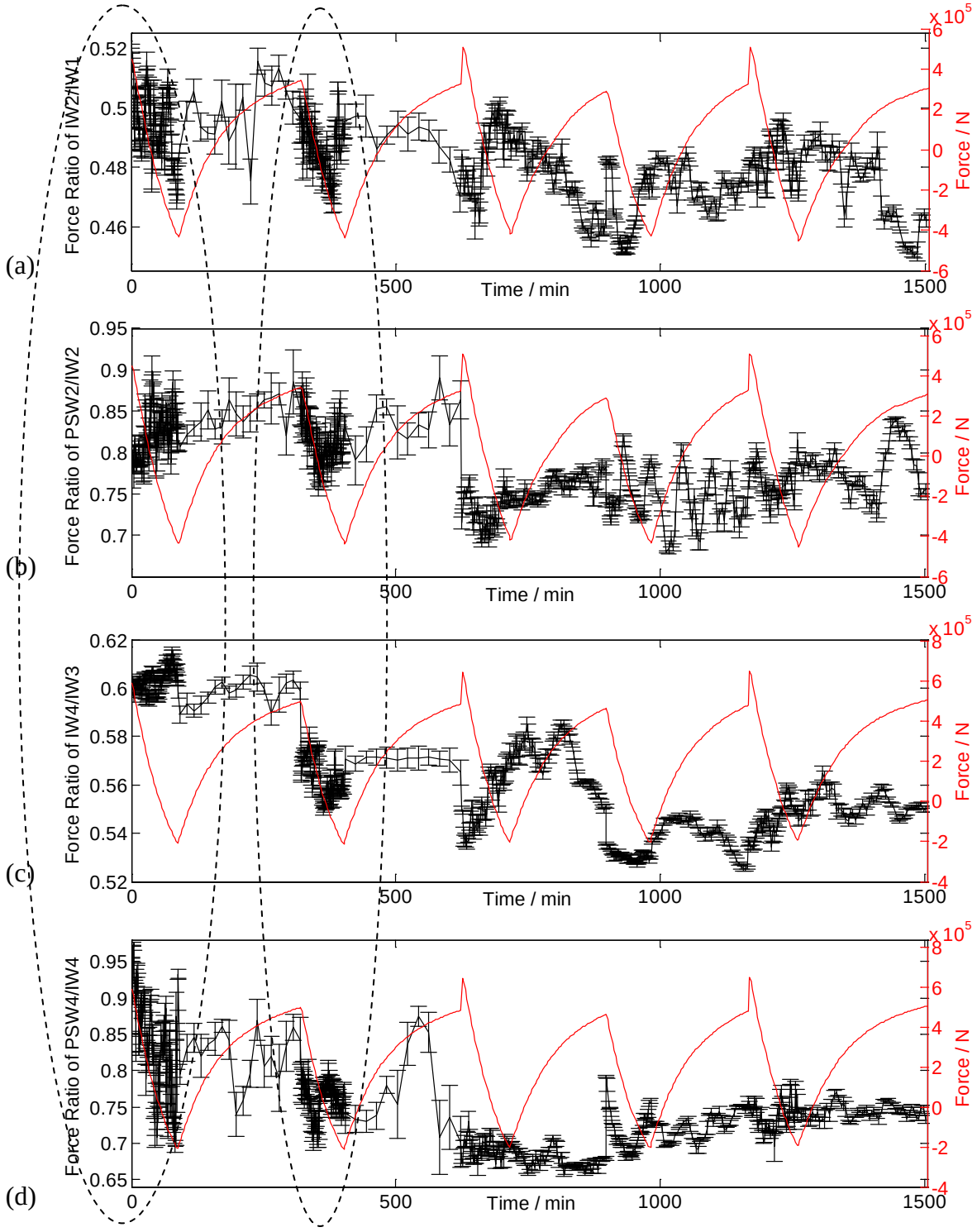

Figure 8.9 Mean value and Standard deviation of wave features: (a) Force Ratio IW2/IW1 + Force in Rail 1; (b) Force Ratio PSW2/IW2 + Force in Rail 1; (c) Force Ratio IW4/IW3 + Force in Rail 2; (d) Force Ratio PSW4/IW4 + Force in Rail 2

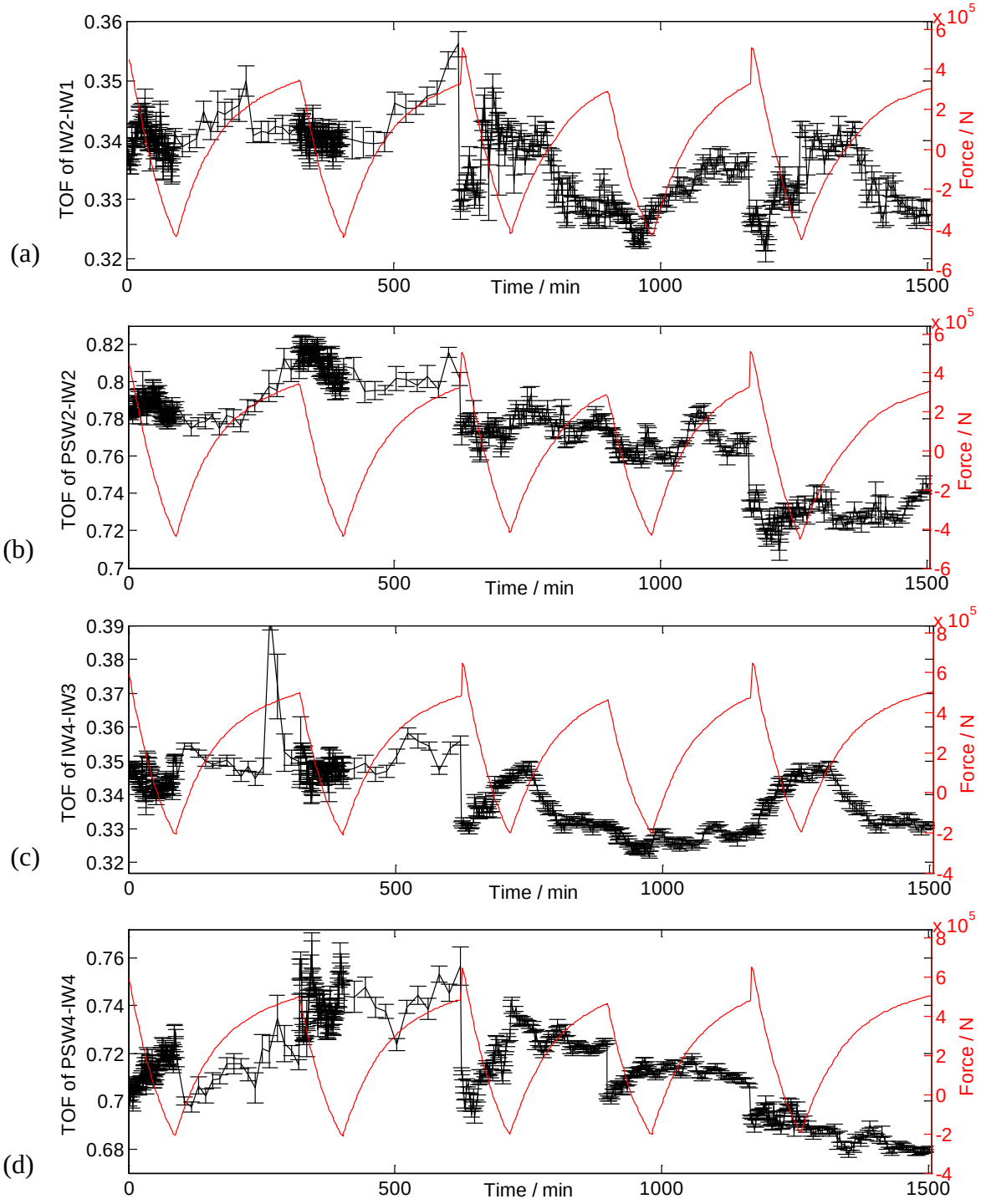

Figure 8.10 (a) TOF of IW2-IW1 in Rail 1; (b) TOF of PSW2-IW2 in Rail 1; (c) TOF of IW4-IW3 in Rail 2; (d) TOF of PSW4-IW4 in Rail 2

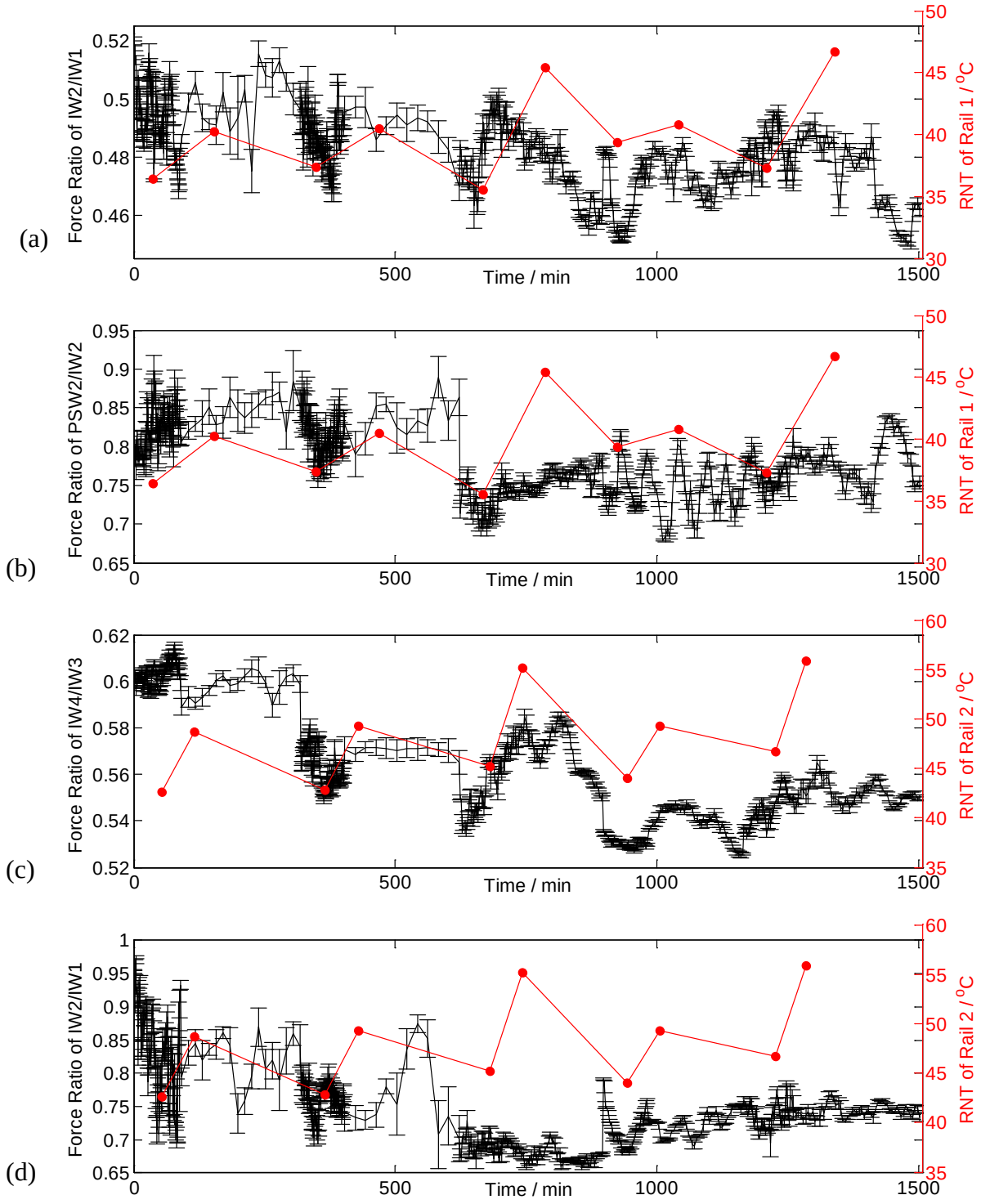

Figure 8.11 Mean value and Standard deviation of wave features: (a) Force Ratio IW2/IW1 + Force in Rail 1; (b) Force Ratio PSW2/IW2 + Force in Rail 1; (c) Force Ratio IW4/IW3 + Force in Rail 2; (d) Force Ratio PSW4/IW4 + Force in Rail 2. The RNT is overlapped.

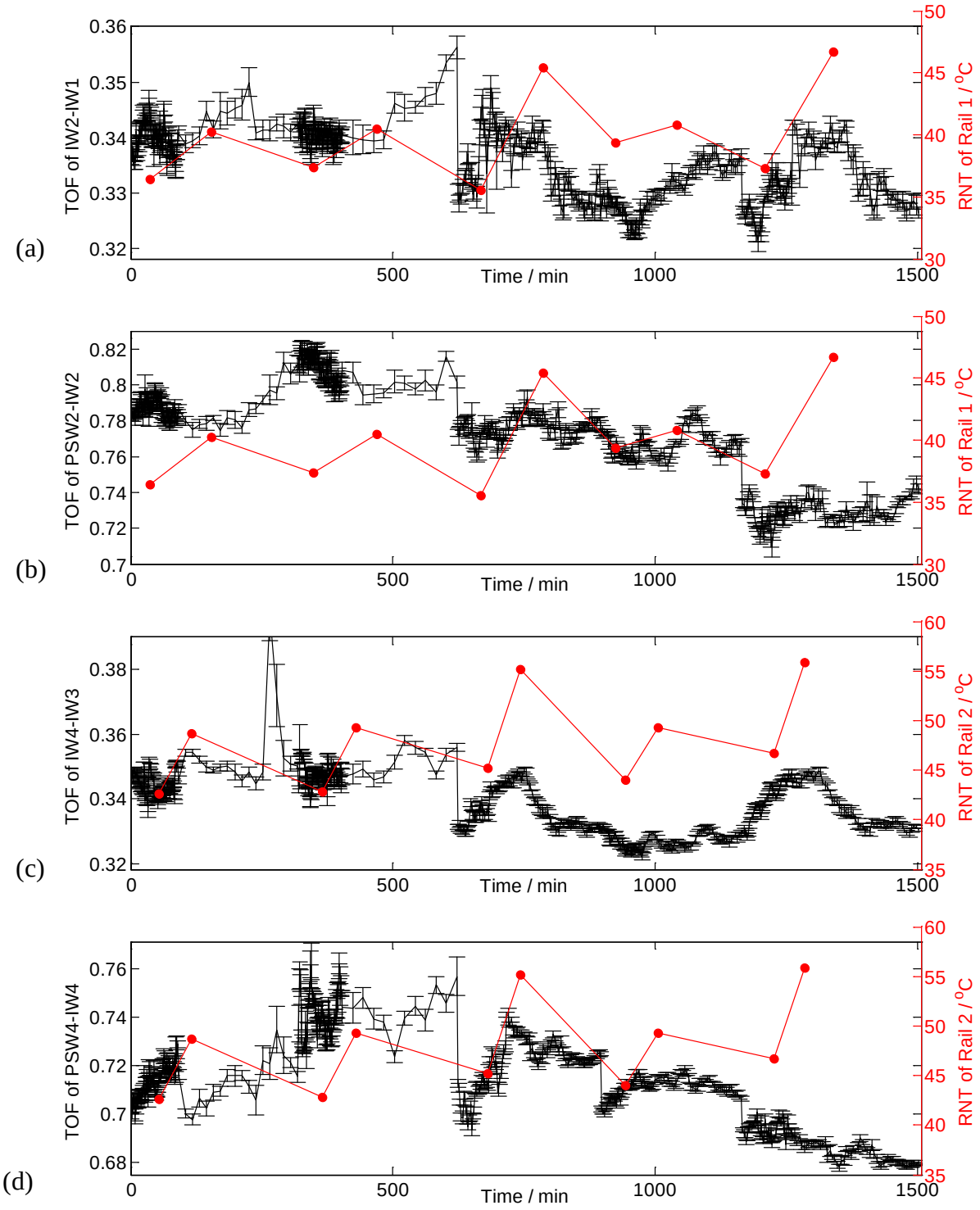

Figure 8.12 (a) TOF of IW2-IW1 in Rail 1; (b) TOF of PSW2-IW2 in Rail 1; (c) TOF of IW4-IW3 in Rail 2; (d) TOF of PSW4-IW4 in Rail 2. The values of the RNT are superimposed.

Finally, we summarize some of the findings by showing Figure 8.13a which displays the difference in the time of arrival between the reflected and the incident wave at the sensor bead located at the horizontal section of the L-shape transducer. The results from both rails are presented. The figure is compared to the rails neutral temperature. It can be seen that over the three days of test the separation between the values of the time of flight between the two rails is very similar to the graph of the RNT. Moreover, there variability visible in the solitary wave feature is also visible in the RNT data.

(a)

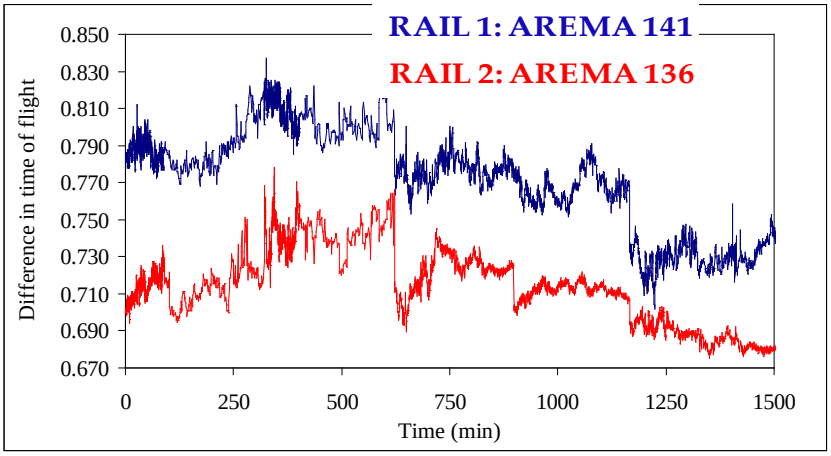

(b)

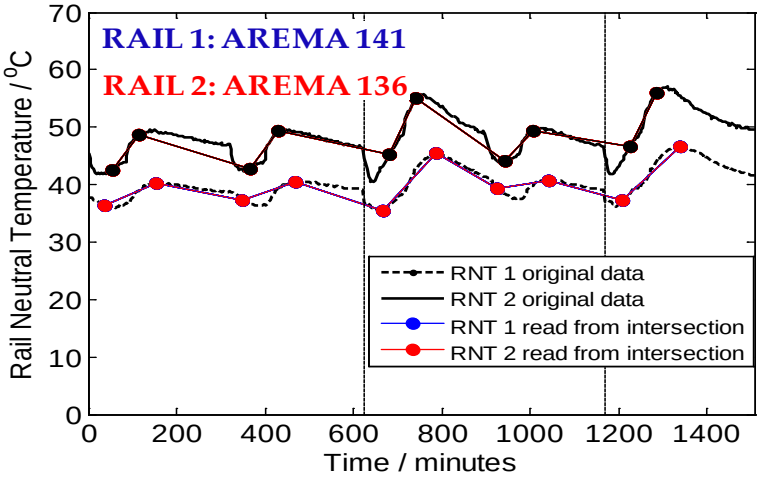

Figure 8.13 (a) Time off light difference between the reflected and the incident wave at the sensor bead located close to the rail for both AREMA 136 and AREMA 141 rail. (b) RNT as a function of the experimental time.

9.0 CONCLUSIONS AND FUTURE STUDIES

In this report we presented the results of a pilot study on the use of highly nonlinear solitary waves for the nondestructive assessment of rails subjected to thermal load. A numerical model was developed to predict the response of solitary waves impacting the surface of slender beams that were, in turn, subjected to a wide variety of material, geometric, properties and applied stress. Some of these simulations were successfully validated experimentally in a series of experiments conducted at the University of Pittsburgh. Then, this pilot technology was tested for the first time in a large-scale Continuous Welded Rail at the University of California, San Diego. These experiments did not prove unequivocally that the proposed technology enables the detection of incipient buckling or the determination of the rail neutral temperature.

During the execution of the project we also demonstrated for the first time:

1) New designs of solitary wave transducers in shape and geometry other than that conventionally used by the scientific community.
2) New designs of noncontact sensors for the detection of solitary waves

Future studies may focus on the following tasks:

- Design magnetostrictive transducers for the L-shape transducers with large (19.05 mm) particles. These transducers may reduce the standard deviation associated with the

experimental measurements and may prove more robust to the challenges associated with field test.

- Use magnetostrictive-based transducers to monitor the propagation of HNSWs in presence of small (< 5 mm) and large (>20 mm) spherical particles.
- Improve the numerical model to replace the continuous beam model with one of the models available in literature to describe the structural response of rail-tie systems under stress.

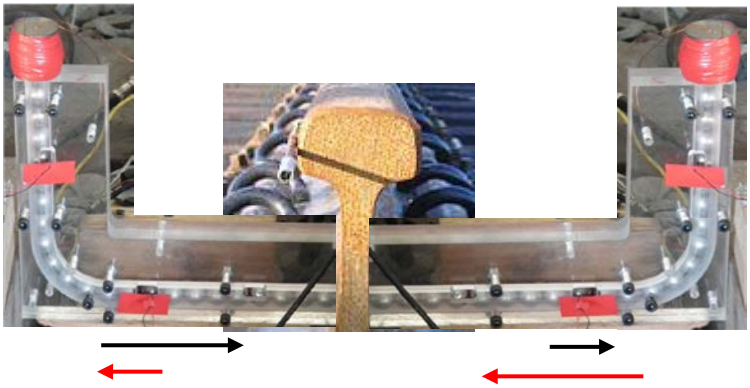

Figure 9.1 Possible test configuration for future studies

- Modify the design of the L-shape transducers to reduce the amount of unwanted reflections from the curved segments. This will provide more energy carried over the horizontal segment and therefore higher wave energy interacting with the rail. The use of a 3-D printer may be considered to build the transducers.
- Modify the setup configuration to include a second L-shape transducer as shown in Figure 9.1. In the setup with two transducers, we will monitor the solitary waves eventually transmitted through the rail web to the second transducer and vice-versa rather than monitoring the reflected waves only. The advantage of this second configuration is that it will be easier to maintain a contact between the rail and the transducers. Moreover,

as the results presented in this report seem to suggest that the energy carried by the solitary wave is not enough to induce large vibration on the rail, there is no need to allow induced vibration on the rail.

- Modify the setup configuration to include an accelerometer attached to the rail web few feet away from the interface rail-granular system. The accelerometer serves to monitor any effect of thermal stress on the low frequency waves induced by the solitary wave pulse.
- Evaluate the effect of the particles' temperature on the characteristics of the HNSWs.
- Test W-beam under compression at well controlled conditions.
- Use statistical analysis and advanced signal processing to evaluate laboratory and field test data.
- Estimate by using numerical modeling, the minimum mass (stiffness) of the granular material (non-linear medium) able to stimulate local vibration of the linear medium (beam, W-section, rail).
- Perform more field test at UCSD to use more transducers and confirm some of the outcomes of this year 1 project.

BIBLIOGRAPHY

Algan, B.B. Finite element characterization of the lateral, thermal buckling behavior of a railroad track structure. Master thesis, *Mechanical Engineering Department*, *Clemson University*, 1977.

Arbabi, F and Khalighi, M. Stability of Railroad Tracks under the Effects of Temperature Change and Earthquake, Journal of Seismology and Earthquake, 12(3), 2010.

Attard, M.M. Finite strain—isotropic hyperelasticity, International Journal of Solids and Structures 40:4353-4378, 2003a.

Attard, M.M. Finite strain-beam theory. International Journal of Solids and Structures 40: 4563-4584, 2003b.

Attard, M.M. Column buckling with shear deformations_A hyperelastic formulation, International Journal of Solids and Structures 45(14): 4322-4339, 2008.

Bartoli, I, Philips, R, Coccia, S, Srivastava, A. Scalea, F. L, Fateh. M and Carr. G. Stress Dependence of Ultrasonic Guided Waves in Rails. Journal of the Transportation Research Board. 91-97. 2010.

Bazant, Z.P. Correlation study of formulations of incremental deformations and stability of continuous bodies. Journal of Applied Mechanics Transactions, ASME 38: 919-928, 1971.

Bazant, Z.P. and Cedolin, L. Stability of Structures. Oxford University Press, Inc., New York. 1991.

Bazant, Z.P. Shear buckling of sandwich, fiber-composite and lattice columns, bearings and helical springs: paradox resolved. ASME Journal of Applied Mechanics 70: 75-83, 2003.

Bijl, F. Buckling force in gapless track calculated in a nonlinear manner. Delngenieur 119–23, 1964.

Boechler, N., Theocharis, G. and Daraio, C. Bifurcation-based acoustic switching and rectification. Nature Materials. 10, 665–668 , 2011.

Cai, L., Yang, J., Rizzo, P., Ni, X. and Daraio, C. Propagation of Highly Nonlinear Solitary Waves in a Curved Granular Chain, Granular Matter, 15, 357-366, 2013a.

Cai, L., Rizzo, P. and Al-Nazer, L. On the Coupling Mechanism between Nonlinear Solitary Waves and Slender Beams, in second round review, International Journal of Solids and Structures, 2013b.

Calkins, F.T., Flatau, A.B. and Dapino, M.J. Overview of magnetostrictive sensor technology. Journal of Intelligent Material Systems and Structures, 18, 1057–1066. 2007.

Carretero-González, R., Khatri, D., Porter, M.A., Kevrekidis, P.G. and Daraio, C. Dissipative solitary waves in granular crystals. Physical Review Letters., 102, 024102:1–024102:4. 2009.

Chatterjee, A. Asymptotic solution for solitary waves in a chain of elastic spheres. Physical Review. E. 59, 5912–5919.1999.

Chopra, A. Dynamics of structures: Theory and Applications to Earthquake Engineering. Third edition, Prentice Hall, 2007

Coste, C., Falcon, E. and Fauve, S. Solitary waves in a chain of beads under Hertz contact. Physical Review E 56, 6104–6117 , 1997.

Coste, C. and Gilles, B. On the validity of Hertz contact law for granular material acoustics. The European Physical Journal B, 7, 155–168, 1999.

Damljanovic, V and Weaver, R. Laser vibrometry technique for measurement of contained stress in railroad rail. Journal of Sound and Vibration. 282: 341-366, 2005.

Daraio, C., Nesterenko, V.F., Herbold, E.B. and Jin, S. Strongly nonlinear waves in a chain of Teflon beads. Physical Review E 72(1), 016603-1-016603-9, 2005.

Daraio, C., Nesterenko, V.F., Herbold, E.B. and Jin, S. Energy trapping and shock disintegration in a composite granular medium. Physical Review Letter 96(5), 058002-1-058002-4, 2006a.

Daraio, C., Nesterenko, V.F., Herbold, E.B. and Jin, S. Tunability of solitary wave properties in one-dimensional strongly nonlinear phononic crystals. Physical Review E, 73, 026610:1–026610:10, 2006b

Daraio, C., Ngo, D., Nesterenko, V.F. and Fraternali, F. Highly nonlinear pulse splitting and recombination in a two-dimensional granular network. Physical Review E, 82(3), 036603-1-036603-8, 2010.

El-Aini, Y.M. Effect of Imperfections on Vertical Track Buckling, Proceed. ASCE, Journal of the Engineering Mechanics Division. 104.1327-1340, 1978.

El-Ghazaly H.A., Sherbourne, A.N. and Arbabi F. Strength and stability of railway tracks–II. Deterministic, finite element stability analysis. Computers & Structures 39(1/2): 23–45, 1991.

Engesser, F. Die Knickfestigkeit gerader Stäbe. Zeitschrift des Architekten und. Ingenieur Vereins zu Hannover. 35, 455, 1889.

Engesser, F. Die Knickfestigkeit gerader Stäbe. Zeutralblatt des Bauverwaltung. 11, 483. 1891.

Esveld, C. and Hengstum, L.A. Tack stability in tight curves. Rail International, 12:15-20, 1988.

Federal Railway Administration, Website: http://safetydata.fra.dot.gov/OfficeofSafety/publicsite/Query/inccaus.aspx, accessed on 4/1/2013.

Fraternali, F., Porter, M.A. and Daraio, C. Optimal design of composite granular protectors. Mechanics of Advanced Materials and Structures. 17, 1-19, 2009.

Geng, J., Reydellet, G., Clément, E. and Behringer, R.P. Green's function measurements of force transmission in 2D granular materials. Physica. D Nonlinear Phenom. 182, 274–303, 2003.

Giurgiutiu, V. and Rogers, C.A. Modeling of the electro-mechanical (E/M) impedance response of a damaged composite beam, ASME Winter Annual Meeting, Adaptive Structures Materials Systems Symposium, Nashville, Tennessee, AD-59, MD-87, 39-46, 1999.

Gjelsvik, A. Stability of built-up columns. Journal of engineering Mechanics 117(6): 1331-1345, 1991.

Grissom, G.T. and Kerr, A.D. Analysis of lateral track buckling using new frame-type equations, International Journal of Mechanical Sciences,48:21-32, 2006.

Haringx, J.A. On the buckling and lateral rigidity of helical springs. Proceedings of the Koninklijke Nederlandse Akademie Van Wetenschappen 45: 533, 1942.

Haringx, J.A. On highly compressible helical springs and rubber rods, and their application for vibration-free mountings. Phillips research report. Eindhoven, 206–220, 1949.

Hibbeler, R. Mechanics of Materials. Prentice hall, 8th edition, 910 pages, 2011.

Hirao, M, Fukuoka, H and Hori, K. Acoustoelastic Effect of Rayleigh Surface Wave in Isotropic Material. Journal of applied mechanics. 48(1):119-125, 1981.

Hirao, M, Ogi, M and Fukuoka, H. Advanced Ultrasonic Method for Measuring Rail Axial Stresses with Electromagnetic Acoustic Transducer. Research in Nondestructive Evaluation. 5: 211-223, 1994.

Hong, J. and Xu, A. Nondestructive identification of impurities in granular medium. Applied physics letters. 81, 4868-4870, 2002.

Hong, J. Universal power-law decay of the impulse energy in granular protectors. Physical Review Letters. 94(10), 108001-1-108001-4, 2005.

Hurlebaus, S. Determination of Longitudinal stress in Rails. Safety IDEA Project 15. Transportation Research Board, National Research Council, 2011.

Job, S., Melo, F., Sokolow, A. and Sen, S. How Hertzian solitary waves interact with boundaries in a 1D granular medium. Physical Review Letters. 94(17), 178002-1-178002-4, 2005.

Job, S., Melo, F., Sokolow, A. and Sen, S. Solitary wave trains in granular chains: experiments, theory and simulations. Granuler Matter 10, 13-20, 2007.

Joule, J.P. On the effects of magnetism upon the dimensions of iron and steel bars. Philosophical Magazine, 30, 76–87, 1847.

Kerr, A. D. On the stability of the railroad track in the vertical plane. U.S. Department of Transportation Report No. FEA/ORD-74/5, 36, 1972.

Kerr, AD. An analysis of thermal track buckling in the lateral plane. FRA/ORD-76/285, Washington, DC, 1976.

Kerr, A.D. and El-Aini, Y.M. Determination of admissible temperature increases to prevent vertical track buckling. Journal of Applied Mechanics. 45.565-573, 1978.

Kerr, AD. An improved analysis for thermal track buckling. International journal of Nonlinear Mechanics, 15(2):99-114, 1980.

Kerr, A.D. and Zarembski, A.M. The response equations for a cross-tie track. Acta Mechanica, 40.253-276, 1981.

Kerr A.D. and Accorsi M.L. Generalization of the equations for frame-type structures, a variational approach. Acta Mechanic 56:55-73, 1985.

Kish, A., Samavedam, G. and Jeong, D. Analysis of thermal buckling tests on U.S. railroads. FRA/ORD-82/45, Washington, DC, 1982.

Kish, A. and Samavedam, G. Recent Investigations on the lateral stability of CWR track. U.S. Department of Transportation, Report No. DOT/FRA/ORD, 1983.

Kish, A. and Samavedam, G. Longitudinal Force Measurement in Continuous Welded Rail from Beam Column Deflection Response. American Railway Engineering Association Bulletin. 712:280-301, 1987.

Kjell, G and Johnson, E. Measuring Axial forces in Rail By Forced Vibration: Experiences From a Full-Scale Laboratory Expeirment. Proceedings of the Institution of Mechanical Engineers, Part F: Journal of Rail and Rapid Trasit. 223:241, 2009.

Kleinke, D.K. and Uras, M.H. A magnetostrictive force sensor. Review of Scientific Instruments.,65, 1699–1710, 1994.

Kleinke, D.K. and Uras, M.H. Modeling of magnetostrictive sensors. Review of Scientific Instruments. 67, 294–301, 1996.

Koob, M. J. The development of a vibration technique for estimation of neutral temperature in continuously welded railroad rail. University of Illinois at Urbana-Champaign, 2005.

Landau, L. and Lifshitz, E. Theory of Elasticity. 3rd Edition. Pergamon, 1986.

Lanza di Scalea, F., Rizzo, P. and Seible, F. Stress measurement and defect detection in steel strands by guided stress waves. Journal of Materrials in Civil Engineering. 15, 219–227, 2003.

Lanza di Scalea, F. Rail Neutral Temperature Measurement. FRA Research & Development Research Review, Washington DC, 2012.

Lazaridi, A. and Nesterenko, V. Observation of a new type of solitary waves in a one-dimensional granular medium. Journal of Applied Mechanics and Technical Physics, 26(3):405-408, 1985.

Lim, N. H., Park, N. H. and Kang, Y. J. Stability of continuous welded rail track, Computers and Structures 81: 2219-2236, 2003.

Lim, N.H. and Sung, I.H. Thermal buckling behavior of continuous welded rail track. Steel Structures 4: 111-119, 2004.

Lim, N. H., Han, S. Y., Han, T. H. and Kang, Y. J. Parametric study on Stability of Continuous Welded Rail-Ballast Resistance and Track Irregularity, Steel Structure, 8:171-181, 2008.

Lim, N.H and Soh, C.K. Effect of varying axial load under fixed boundary condition on admittance signatures of electromechanical impedance technique. Journal of Intelligent Material Systems and Structures, 23:815-826. 2012.

Nesterenko, V. Propagation of nonlinear compression pulses in granular media. Journal of Applied Mechanics and Technical Physics, 24(5):733-743, 1983.

Nesterenko, V.F., Lazaridi, A.N. and Sibiryakov, E.B. The decay of soliton at the contact of two “acoustic vacuums”. Journal of Applied Mechanics and Technical Physics. 36, 166-168, 1995.

Nesterenko, V. Dynamics of Heterogeneous Materials. Springer, 2001.

Nesterenko, V.F., Daraio, C., Herbold, E.B. and Jin, S. Anomalous wave reflection at the interface of two strongly nonlinear granular media. Physical Review Letters. 95, 158702-1-158702-4, 2005.

Ni, X., Rizzo, P. and Daraio, C. Actuators for the generation of highly nonlinear solitary waves. Review of Scientific Instruments. 82(3), 034902-1-034902-6, 2011a.

Ni, X., Rizzo, P. and Daraio, C. Laser-based excitation of nonlinear solitary waves in a chain of particles. Physical Review E, 84, 026601:1–026601:5, 2011b.

Ni, X. Nondestructive evaluation and structural health monitoring based on highly nonlinear solitary waves. Ph.D. Thesis, University of Pittsburgh, 2011c.

Ni, X., Rizzo, P., Yang, J., Katri, D. and Daraio, C. Monitoring the hydration of cement using highly nonlinear solitary waves. NDT & E International 52, 76-85, 2012a.

Ni, X. and Rizzo, P. Highly nonlinear solitary waves for the inspection of adhesive joints. Experimental Mechanics 52(9), 1493-1501, 2012b.

Ni, X. and Rizzo, P. Use of highly nonlinear solitary waves in NDT. Materials Evaluation 70, 561-569, 2012c.

Ni, X., Cai, L.Y. and Rizzo, P. A Comparative Study on Three Different Transducers for the Measurement of Nonlinear Solitary Waves. Sensors 13, 1231-1246, 2013.

Nucera, C., Phillips, R. and Lanza di Scalea, F. Ultrasonic Guided Wave Monitoring of Railroad Tracks. Advances in Science and Technology. 83, 198-207, 2012.

Phillips, R., Zhu, X. and Lanza di Scalea, F. The influence of stress on Electro-mechanical impedance measurements in rail steel. Material Evaluation, 70(10): 1213, 2012.

Ramesh MS. A nonlinear finite element approach to the analysis of lateral thermal and mechanical buckling of railroad tracks. Master Thesis, Clemson University, 1985.

Reissner, E. On one-dimensional finite-strain beam theory: the plane problem. Journal of Applied Mathematics and Physics 23: 795–804, 1972.

Reissner, E. Some remarks on the problem of column buckling. Ingenieur-Archive 52: 115-119, 1982.

Rizzo, P. and Lanza di Scalea, F. Effect of Frequency on the Acoustoelastic Response of Steel Bars. Experimental Techniques. 27(6), 40-43, 2003.

Rizzo, P. and Lanza di Scalea, F. Monitoring in cable stays via guided wave magnetostrictive ultrasonics. Materials. Evaluation., 62, 1057–1065, 2004.

Rizzo, P., Bartoli, I., Marzani, A. and Lanza di Scalea, F. Defect classification in pipes by neural networks using multiple guided ultrasonic wave features extracted after wavelet processing. J. Press. Vessel Tech., 127, 294–303, 2005a.

Rizzo, P. and Lanza di Scalea, F. Ultrasonic inspection of multi-wire steel strands with the aid of the wavelet transform. Smart Materials and Structures, 14, 685–695, 2005b.

Rizzo, P. and Lanza di Scalea, F. Feature extraction for defect detection in strands by guided ultrasonic waves. Struct. Health Monit., 5, 297–308, 2006.

Rizzo, P., Sorrivi, E., Lanza di Scalea, F. and Viola, E. Wavelet-based outlier analysis for guided wave structural monitoring: application to multi-wire strands. Journal of Sound Vibration 307, 52–68, 2007.

Robertson, C. Adelaide advertise, Website: http://www.telegraph.co.uk/news/picturegalleries/worldnews/4360255/Heatwave-in-Melbourne-plays-havoc-with-the-Australian-Open.html, accessed on 4/20/2012.

Samavedam, G. Buckling and post buckling analysis of CWR in the lateral plane. Technical Note TN-TS-34,British Railways Board, 1979.

Samavedam, G., Kish, A. and Jeong, D. Parametric studies on lateral stability of welded rail track, U.S. Dept. of transportation, Report No. DOT/FRA/ORD-83/07, 1983.

Schneider, E. Ultrasonic birefringence effect - its application for materials characterizations, Optics and Lasers in Engineering 22, 305-323, 1995.

Sen, S., Manciu, M. and Wright, J.D. Solitonlike pulses in perturbed and driven Hertzian chains and their possible applications in detecting buried impurities. Physical Review E 57(2), 2386-2397, 1998.

Sen, S., Manciu, M. and Manciu, F.S. Ejection of ferrofluid grains using nonlinear acoustic impulses—A particle dynamical study. Applied Physics Letter 75, 1479-1481, 1999.

Sen, S., Hong, J., Bang, J., Avalos, E. and Doney, R. Solitary waves in the granular chain. Physics Report 462(2), 21-66, 2008.

So, W. and Martin, G.C. A finite element model for track buckling. Conference on Advanced Techniques in Track/Train Dynamics, Chicago, Pergamon Press, 1977a.

So, W. and Martin, G.C. Finite element track buckling model. IEEE-ASME joint railroad conference, Washington, D.C., Mar.30-Apr, 1977b.

So, W. and Young, W. W. Mechanical model for lateral thermal buckling and displacement of the curved track. Transportation Research Board, Trans. Res. Record, No. 694, 24-29, 1978.

Szelazek, J. Monitoring of Thermal Stresses in Continuously Welded Rails with Ultrasonic Technique, NDTnet, 3(6): 1-8. 1998.

Tedesco, J, Mcdougal, W. and Ross, C. Structural Dynamics-Theory and applications, Addison Wesley, 1999.

Timoshenko, S.P. and Gere, J.M. Theory of Elasticity. McGraw-Hill International, London, 1963.

Tumanski, S. Induction coil sensors—A review. Measurement Science and Technology, 18, R31-R46, 2007.

Villari, E. Change of magnetization by tension and by electric current. Annual Review of Physical Chemistry, 126, 87–122, 1865.

Vortok International & AEA Technology. Verse® Technical Information Pack. AEA Technology, 2007a.

Vortok International & AEA Technology. User guide to Verse® United Kindom Version. AEA Technology, 2007b.

Wegner, A. Non-Destructive Determination of the Stress Free Temperature in CWR Tracks. Proceedings of the Longitudinal Force Workshop (Compact Disk). 173-216, 2005.

Wegner, A. Prevention of Track Buckling and Rail Fracture by Non-destructive Testing of the Neutral Temperature in cw-Rails. IHHA Spezialist Technical Session (STS), 2007.

Yang, J., Silvestro, C., Khatri, D., De Nardo, L. and Daraio, C. Interaction of highly nonlinear solitary waves with linear elastic media. Physical Review. E 83(4), 046606-1-046606-12, 2011.

Yang, J., Dunatunga, S. and Daraio, C. Amplitude-dependent attenuation of compressive waves in curved granular crystals constrained by elastic guides. Acta Mechanics. 223(3), 549-562, 2012a.

Yang, J., Sangiorgio, S. N., Borkowski, S.L., Silvestro, C., De Nardo, L., Daraio, C. and Ebramzadeh, E. Site-specific quantification of bone quality using highly nonlinear solitary waves. Journal of Biomechanical Engineering. 134, 101001-1-101001-8, 2012b.

Yang, J., Silvestro, C., Sangiorgio, S.N., Borkowski, S.L., Ebramzadeh, E., De Nardo, L. and Daraio, C. Nondestructive evaluation of orthopaedic implant stability in THA using highly nonlinear solitary waves. Smart Materials and Structures. 21, 012002-1-012002-10, 2012c.

Zhu, Y., Shukla, A. and Sadd, M.H. The effect of microstructural fabric on dynamic load transfer in two dimensional assemblies of elliptical particles. Journal of the Mechanics and Physics of Solids, 44, 1283–1303, 1996.

Zielger, H. Arguments for and against Engesser's buckling formulas. Ingenieur-Archive 52: 105-113, 1982.